UNIVERSITY OF THESSALY
POLYTECHNIC SCHOOL
DEPARTMENT OF MECHANICAL ENGINEERING

Experimental Investigation of Droplet Impingement on Solid Surfaces

By

Antonios-Panagiotis Kaltsas
Panagiotis Papadatos

Supervised by:

Professor Georgios Charalampous

Submitted in partial fulfillment of the requirements for the diploma of Mechanical Engineering
VOLOS 2019

Στην Οικογένειά μου,

Certified by the members of the Thesis Committee:

First examiner	Dr. Georgios Charalampous
{Supervisor}	Assistant Professor, Department of Mechanical Engineering,
	University of Thessaly
Second examiner	Dr. Vasilios Bontozoglou
	Professor, Department of Mechanical Engineering,
	University of Thessaly
Third examiner	Dr. Nicolaos Pelekasis
	Professor, Department of Mechanical Engineering,
	University of Thessaly

Abstract

The droplet impingement on different kinds of surfaces, is a phenomenon of great importance in industries. In the current thesis we examine the droplet collision in already wetted surfaces. Experiments were conducted using three surfaces with different roughness (Ra) of 0,09μm, 1,37μm and 6,99μm. The droplets fell from a syringe held in different heights above the surfaces and the collision was captured by a high speed camera. The three surfaces were examined in 10˚,20˚and 30˚ angles impact with respect to the horizontal axis, for six different droplet We numbers in each case (We=260, We=329, We=388, We=441, We=489, We=534). The images taken from the lab were analyzed and four parameters were measured on them, namely the crown height on both sides and the angle it formed with the surface again on both sides. The results of the measurements were depicted in diagrams related to the droplet We number and the roughness of the surfaces, in order to reveal the trend of each of the four parameters in each case.

Acknowledgements

The following thesis was composed in the scope of partial fulfilment of the requirements for the Diploma of the Mechanical Engineer at the University of Thessaly. However, this work would not have been possible without the aid of many people. The following section, is a personal effort for the expression of our deepest regards, for the help of all those people who contributed to the fulfilment of our work.

Firstly, and most importantly we want to thank our academic supervisor, for giving us the opportunity to complete our work on this interesting Thesis project and for the successful outcome of it. For all those reasons we would like to express our deepest regards to our Professor Georgios Charalampous. His crucial suggestions, helped us overcome every difficulty during the experimental procedure and his guidance on the adequate composition of the Thesis paper was truly important. His comments and guidance will be an important resource for our future academic steps in the sector of Mechanical Engineering and aerodynamics.

Last but not least, we will always be thankful to our family for their endless support and encouragement during all those years of our studies.

Table of Contents

List of Figures

List of Tables

Nomenclature

Bo	Bond number	-
Ca	Capillary number	-
D	Droplet Diameter	L
f	Impact frequency	T^{-1}
Fr	Froude number	-
g	Gravity acceleration	LT^{-2}
h^*	Dimensionless film thickness	-
h_o	Thickness of pre-existing Layer	L
K	Important composite group	-
La	Laplace number	-
n	Self-similar variable	L
Oh	Ohnesorge number	-
R_a	Arithmetic surface roughness	L
Re	Reynolds number	-
R_{nd}	Non-dimensional roughness	-
V	Droplet volume	L^3
V_o	Impact velocity	LT^{-1}
We	Weber number	-
μ	viscosity	MLT^{-1}
ρ	Liquid density	ML^{-3}
σ	Surface tension	MT^{-2}
v	Kinematic viscosity	L^2T^{-1}
ρ^*	Liquid-Gas density ratio	-
μ^*	Liquid-Gas viscosity ratio	-

1. Introduction

1.1 General analysis of the phenomenon

"You would never know if a drop fell in the water if you didn't see the ripples"

-James John

The shape of a droplet or even the sliding of it over a surface is a very common and vibrant image for any human brain. It has been observed by everyone at least once during his lifetime. Raindrops on a window is an everyday example when we speak about drop impact. Apart from the visual interest, drop movements, especially drop impacts on solid and liquid surfaces have a great influence on a large scale of technological applications located in everyday life. Ink-jet printing, rapid spray cooling of hot surfaces (such as turbine blades or rolling mills for steel production), annealing, quenching of aluminium alloys and steel, incinerators, spray painting and coating, plasma spraying and crop spraying are some characteristic examples. Electronics, like solder bumps on printed circuit boards, electric circuits and microelectronics produced by solder-drop dispensing are based on the behaviour of liquid formed soldering and drop segments orientation. Furthermore, drop impacts play a key role in the effectiveness and general function and at the production procedures of powder cleanings used daily. In addition to technical applications, drop impacts can be found in nature. A vast variety of natural phenomena are "dominated" by the existence of drops. Aeration of the surface layer of lakes, seas and oceans depend on air bubble entrainment due to raindrop impacts. Erosion of soil, dispersal of spores and micro-organisms or underwater noise during rains are some additional natural phenomena involving drop impact (Shoshan, Wygoda, & Umansky, 2005). Plus, special fields of study such as criminal forensics, transport of surface contaminants into bulk liquids and gas entrapment are based on theories strongly connected with droplet characteristics and behaviours.

The number of applications reveals with the most suitable way the importance of understanding the phenomenon of drop impacts and express the mechanism underlying. However, the physical problem is extremely difficult to solve because of the lack of information and the complexity of the mechanism. This is why the need for experimental process is crucial. The study of drop impact is considered as relatively young as it began to appear intensively in the last decades. Worthington (Worthington & Cole, 2006) was one of the first who decided to investigate the problem of droplet impacts with a systematic approach. The result of this investigation was published in a book filled with fascinating photographs of the phenomena created by drops of liquid and solid-balls impacts on deep liquid pools (Figure 1.1). That book sparked later efforts by physicists, engineers and mathematicians who took interest in the phenomena and tried to provide analytical forms validated by experimental data Nevertheless, the phenomenon of drop impacts has been partially understood and there is plenty of room for further more studies.

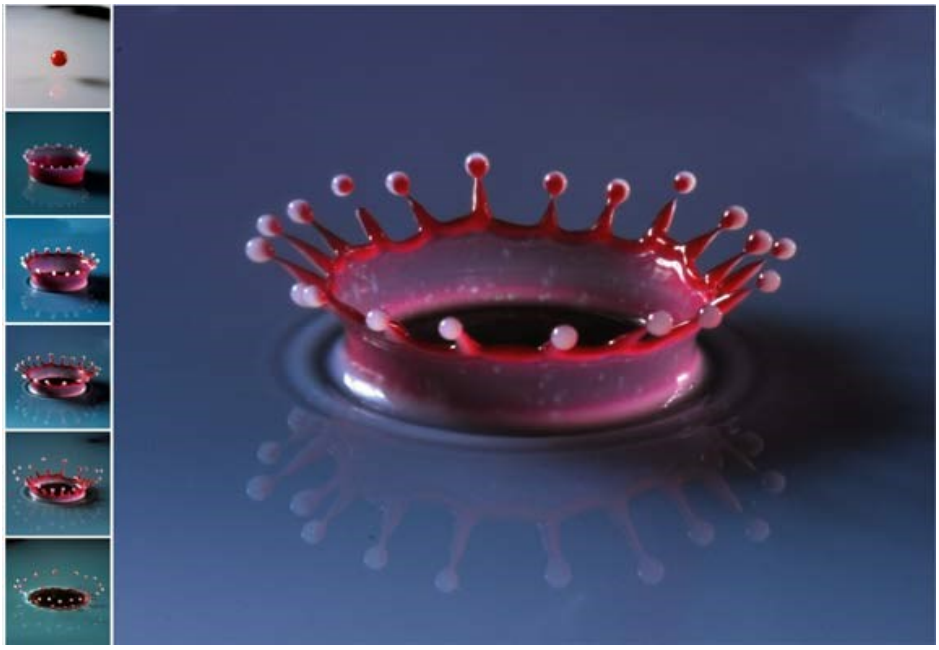

Figure 1.1: High speed photograph of red coloured droplet impact on liquid layer inspired by Worthington work, Wim Von Hoeve, University of Twente.

We will start by quoting the parameters that can affect and provoke the phenomenon of drop impact. These parameters will be used later for the categorization and planning of the experimental procedure. The drop size and shape is very important. The shape of a drop may be spherical or even elliptic at the moment of impact with the elliptic form created due to oscillations. The impact surface may be dry solid or consisted of a thin liquid layer, it can also be the liquid free surface in a deep pool. The orientation of the impact is a significant parameter. A schematic representation of the referred parameters has been made by Rein as shown in Figure 1.2. The impact may be normal with the drop orbit perpendicular to the impact surface or even oblique. The selected liquid may be Newtonian or non-Newtonian. The liquid of the drop and the liquid of the surface may be the same or not and also miscible or not.

If we refer to solid surface impact, the surface qualities must be taken into consideration. The surface may be rough or smooth, hard or soft, chemically homogenous or heterogeneous. The shape of the surface may be flat or curved with or without porous. It may also present a different temperature from that one of the drop or even the same. The outcome of the impact is also crucial. When we refer to solid dry surfaces, the impact may result in drop spreading, resending, bounding or levitating. The phenomenon of levitating is generated if evaporation of the drop occurs by a significantly hot surface which follows the criteria of the Leidenfrost effect. For a deep pool impact, the result may be a crater in the liquid free surface with the following forming of Worthington Jet in the area. Furthermore, for the case of impact on a thin liquid layer known as liquid film, the result may be a crown formation known as splashing. Propagation and breakup can be also observed in this type of impact.

The outcome of drop impact depends on the mentioned factors above. However, a relisting of them will be useful. The impact velocity, the properties of the used liquid such as its density, viscosity or viscoelasticity, the size of the impacting drop and the existence or not of Newtonian behavior with the surface or interfacial tension are very important. Furthermore, referring to the case of solid surface the characteristics are substantial for the phenomenon. The wettability and roughness of the solid

surface or the existence of non-isothermal phenomena are also a factor. The compressibility of the liquid can be also taken into consideration when the impact is very strong.

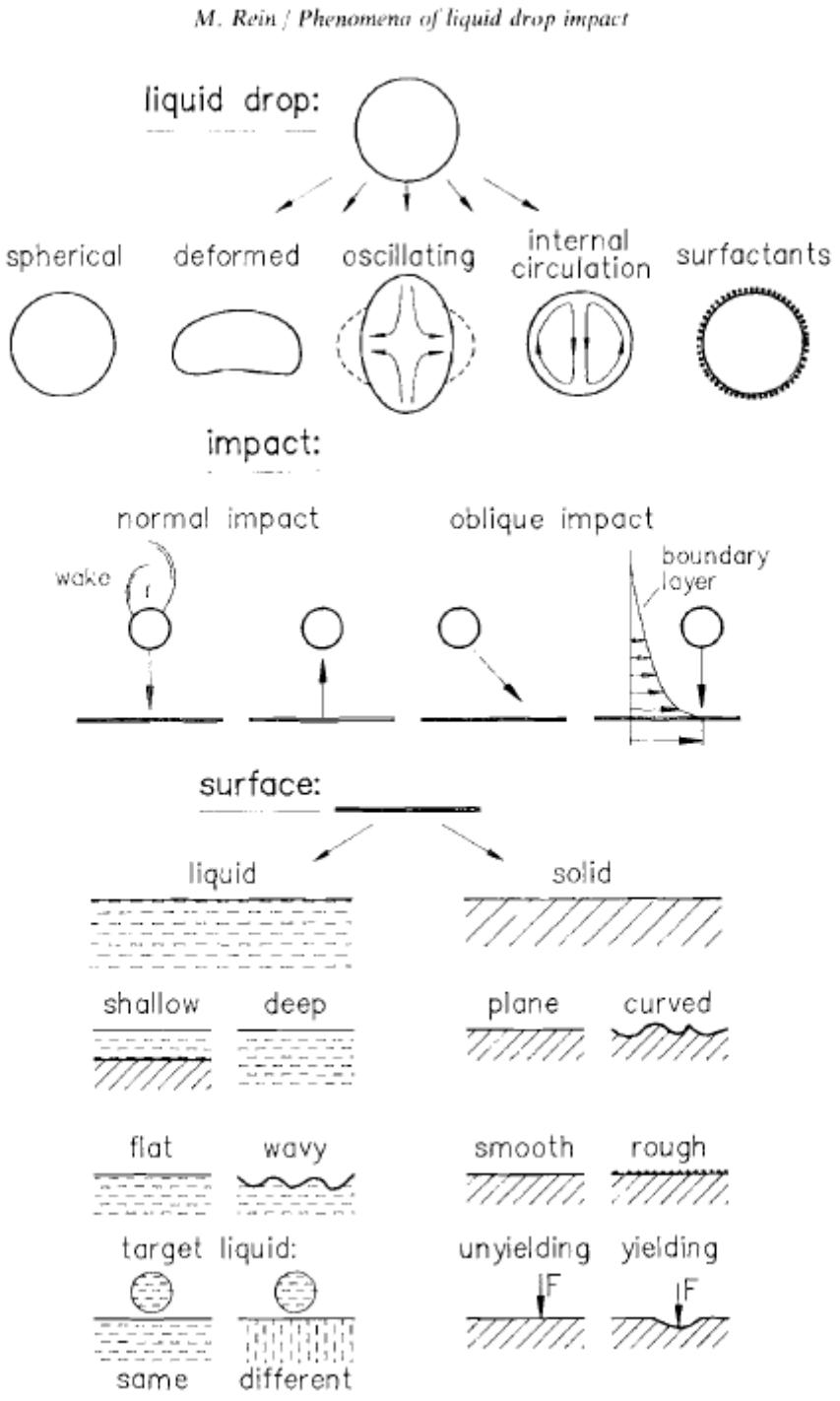

Figure 1.2: Survey of parameters governing the impact of a liquid Drop (Martin Rein, 1993).

In order to form mathematical equations describing drop impact, we need to name the basic parameters and physical properties which will be employed in the following thesis analysis. These parameters are known as dimensionless groups of the phenomenon and they are, the Weber number, the Reynolds number and the Ohnesorge number, as well as, the dimensionless film thickness h* and the parameter K which is used as a classification factor. Furthermore, effects related with gravity are described by the Bond number and by the Froude number. However, gravity related phenomena are not usually taken into consideration.

$$We = \frac{\rho DVo^2}{\sigma} \quad (1) \qquad Re = \frac{\rho DVo}{\mu} \quad (2) \qquad Oh = \frac{\mu}{(\rho\sigma D)^{\frac{1}{2}}} = \frac{We^{1/2}}{Re} \quad (3)$$

$$K = We \cdot Oh^{-\frac{2}{5}} \quad (4) \qquad h^* = \frac{ho}{D} \quad (5) \qquad Fr = \frac{Vo^2}{Dg} = \frac{We}{Bo} \quad (6)$$

Where μ the viscosity of the liquid and ρ, σ are the density and surface tension respectively. The use of g is for describing the acceleration of gravity for the system. The parameters D and ho are used to describe the diameter of the drop and the thickness of the liquid film correspondingly. Besides, when we talk about drop impact on solid surface, there are also factors and dimensionless numbers describing the surface condition. These numbers will be mentioned later. Nevertheless, an important classification number that needs to be added in this category is the capillary number.

$$Ca = \frac{\mu}{\sigma_{lv}} \cdot U_o \quad (7)$$

$$La = \frac{\rho\sigma_{lv}}{\mu^2} \cdot Do = \frac{Re^2}{We} = \frac{We}{Ca^2} = \frac{Re}{Ca} = Oh^{-2} \quad (8)$$

The dimensionless numbers referred above have been defined mathematically, but we need to quote their physical background. The Reynolds parameter is known as a dimensionless number that compares the effect of inertia forces versus the viscous forces on a referred liquid. Also, the dimensionless Weber number is very known in fluid mechanics and it can be thought as a measure of the relative importance of the fluid's inertia compared to its surface tension. The Ohnesorge number can occur from the combination of Weber and Reynolds number. The Ohensorge number as long as with the Capillary number they relate the viscous forces to surface tension forces. The Laplace number relates the surface tension forces to momentum transport also known as dissipation. Moreover, the Bond and Froude dimensionless numbers are connected with the phenomenon of gravity. The Froude number relates the inertial forces to gravitational forces and the Bond number the body forces which are dominated by gravitational forces to surface tension forces.

1.2 Drop impact on Thin Liquid Layer Surfaces

1.2.1 Definition of Liquid surface

The basic principle behind the drop collision on a wet surface is that the drop is left from a certain height and comes into contact with a fixed solid surface between which a liquid medium appears. However, before analyzing the mechanism underlying the drop impact on liquid layer the explanation of the liquid surface is crucial. The thickness of the layer is a matter of importance because it separates the physical phenomenon of drop impacts into thin liquid layers from drop impacts into liquid pools. In the first case, the thickness of the liquid medium is extremely lower in size even from the diameter of the impacting drop. Contrariwise, in the case of the liquid pool impact, the thickness of the liquid layer appears higher than the size of the droplet. The mentioned comparisons with the drop diameter for the liquid medium in every case can be quantified by the help of the factor ho/D known as the dimensionless thickness layer. With h_o we refer to the thickness size of the liquid layer and with D to the drop diameter. For the first case on thin layer impacts, the fraction appears low values and for deep pool impacts, the values are extremely higher. Tropea and Marengo (Tropea & Marengo, 2014) have studied the phenomenon and broadened the scenarios of liquid surface by distinguish four different types, the thin film, the liquid film, the shallow pool and the deep pool . The selection of this four types of liquid surfaces was based on the magnitude of film thickness h relative to arithmetical mean value of wall roughness R_a and also the length scale of the wall roughness L_a. The referred parameters are also non-denationalized by the drop diameter D, before the impact occurs (Liang & Mudawar, 2016). The classification equations emerged for the needed parameters are the following.

$$h^* = ho/D \quad (9a) \qquad R_{nd} = R_a/D \ (9b) \qquad L_{nd} = L_a/D \ (9c)$$

Table 1.1: Regimes of drop impact on a liquid surface (Tropea & Marengo, 2014)

Regime	Range	Impact characteristics
Thin film	$L_{nd} < h^* < 3R_{nd}^{0.16}$	Impact depends on wall features
Liquid film	$3R_{nd}^{0.16} < h^* < 1.5$	Impact is weakly dependent on wall features
Shallow pool	$1.5 < h^* < 4$	Impact depends on film thickness but is independent of wall features
Deep pool	$h^* \gg 4$	Impact is independent of film thickness

According to Table 1.1, we can clearly observe that both liquid and thin film reveal an upper bound of 1,5 (h < 1,5). However, Vander et al. proposed a different classification rule in which the thin film is generated on dimensionless thickness layers values close to 0,1 and for the case of liquid film the values of h^* are placed between 1 and 10 ($1 \le h^* \le 10$)(Vander Wal, Berger, & Mozes, 2006). Wang and Chen placed their personal perspective about the classification of the problem by adding the restriction for very thin film for h* values lower than 1 (h* < 1)(Wang & Chen, 2000).Besides, Cossali et al.(Cossali, Coghe, & Marengo, 1997) and Motzkus et al. (Motzkus, Gensdarmes, & Géhin, 2009) found that thin liquid films are associated with h* lower than 1 (h*< 1) opinion that has been widely

accepted among experimental investigators. Several specialists emphasized the importance of wall roughness underneath the liquid layer which should not be neglected for the case of thin films (Cossali et al., 1997; Stow & Stainer, 2017; Yarin & Weiss, 1995).

For the liquid film layer, a differentiation appears on its formation procedure. Specifically, the liquid film can preexist on the solid surface or it can be generated by multiple drop impacts. For this specific reason, the physical problem can be divided into two basic categories, the pre-existing liquid film and the film created by impacts of previous drops. A wide series of experimental procedures and theoretical work have been made by multiple scientists the past years, trying to describe and analyze the phenomenon evolution in each case. Yarin & Weiss were some of the first who studied the field of the drop generated liquid film. Normal impact of successive monodisperse ethanol drops (with D=70–340 μm and V0 up to 30 m/s) on a solid surface was studied experimentally by Yarin & Weiss (Yarin & Weiss, 1995). Following the first impact, the wall was permanently covered by a thin liquid film with thickness of the order of h ≈ (ν/f)1/2, f being the frequency of the impacts and f−1 the characteristic time of one impact. Besides, the case of pre-existing liquid layer has been studied by Cossali et al. Cossali et al. (Cossali et al., 1997), Wang & Chen (Wang & Chen, 2000), and Rioboo et al. (Rioboo, Bauthier, Conti, Voué, & De Coninck, 2003). Single-drop impacts on pre-existing films of the same liquid were studied and comparison has been made with the analytical forms generated by the previous work of Yarin & Weis (Yarin & Weiss, 1995).

1.2.2 Morphology and basic parameters Governing liquid impact dynamics phenomenon

Drop impingements on a liquid surface may be a very common physical phenomenon but involves a wide variety of mechanisms underlying and affecting every time the outcome of the collision. Furthermore, the element of time is strictly connected with the evolvement of it. Thence, it is necessary to lay a timeline with the impact characteristics. Figure 1.3 shows the variety of stages and characteristics of drop impact, along with basic parameters effecting the phenomenon. The dominant elements of the impact evolution based on time are, the drop prior to impact, the formation of the ejecta sheet, the transition from ejecta sheet to liquid crown, the formation of liquid crown following impact without the existence of splashing, and the formation of liquid crown following impact with splashing. The lack of splashing is also known as spreading. In case of spreading sufficiently low impact velocities spread the drops over the wall, taking the shape of lamellae with a visible outer rim (Figure 1.4(a)). In addition to, at still lower impact velocities practically no rim is visible, which Rioboo et al. (Rioboo et al., 2003) termed deposition. By contrast, at higher impact velocities the lamellae later took the shape of crowns (Figure 1.4(b)) consisting of a thin liquid sheet with an unstable free rim at the top, from which is combined with the scattering of numerous small secondary droplets from the crown's rim. The case of ejecta is a very quick phenomenon formed in the earliest seconds of impact and culminates in the formation of the liquid crown. The existence of ejecta is in order of milliseconds.

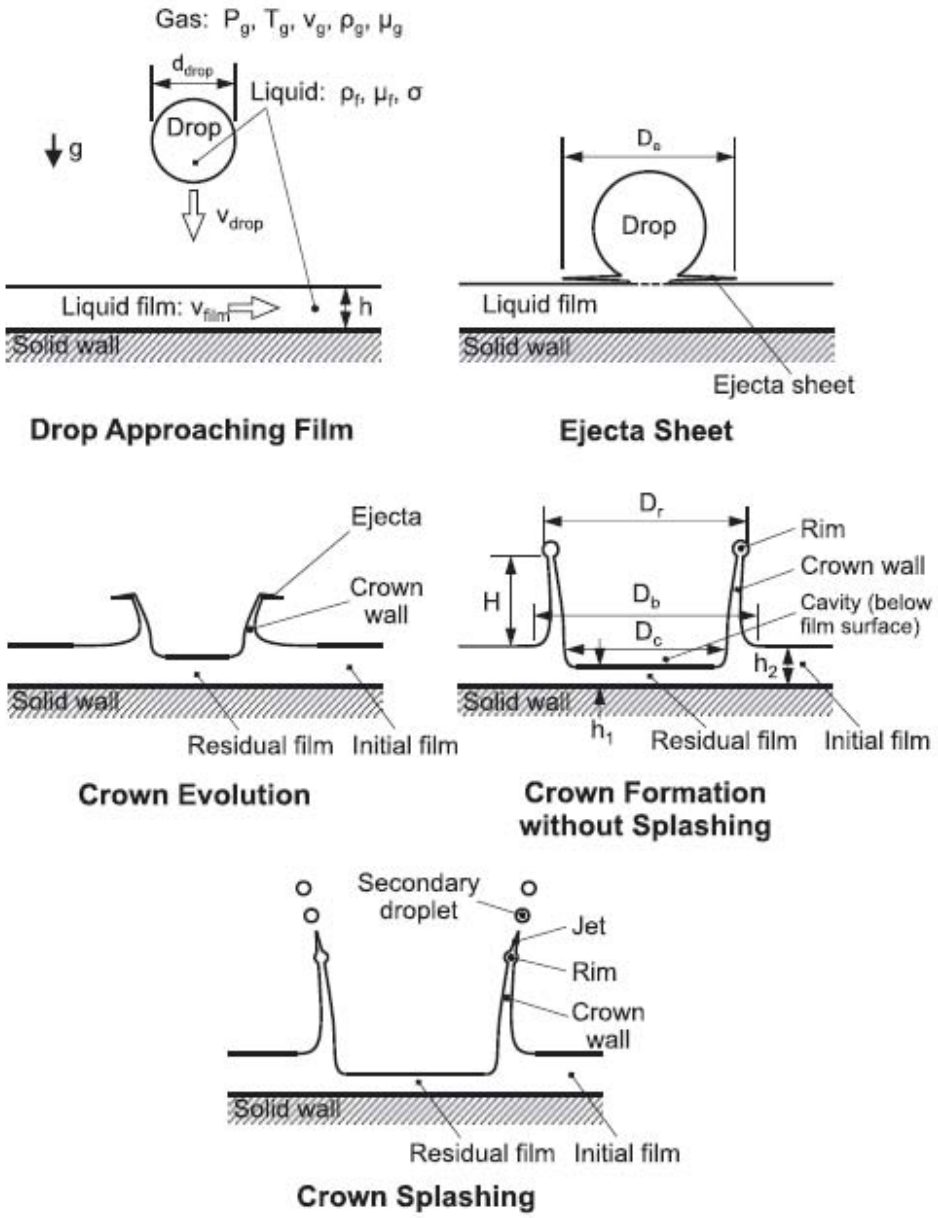

Figure 1.3: Schematics of drop impact on a liquid film and associated nomenclature (Liang & Mudawar, 2016).

The term of splashing is a result based on the criteria posed by the scientist each time depending on the problems nature and characteristics. For this reason, several other definitions of splashing can be found in literature. When we refer to deep pool impacts the ejection of liquid from the crater with or without formation of droplets at the top of the rim. Another example is the formation of Worthington jet ejected at the crater center. However, in case of liquid film impacts these outcomes do not occur cause of the film thickness restrictions (h*= ho/D, h*<1)(Rioboo et al., 2003; Wang & Chen, 2000). Liquid pool impacts are out of interest in the following thesis hence, these types of images are not considered here.

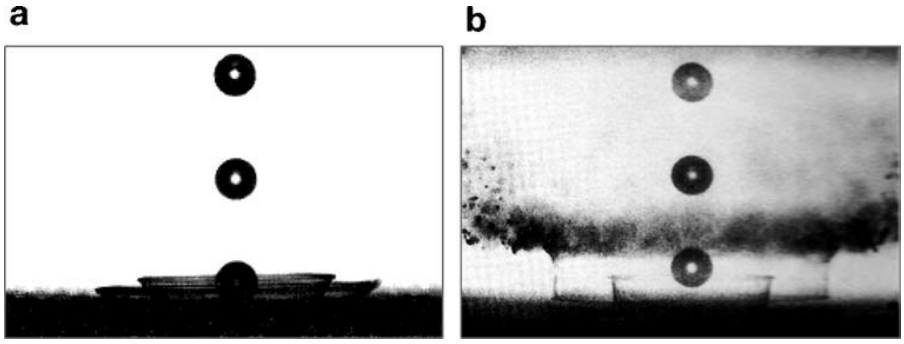

Figure 1.4: (a) Spreading ethanol drops stroboscopically illuminated. Spreading lamellae at two different stages can be recognized. Drop diameter D=279 μm, impact velocity V0 = 7.8 m/s, We =588, Re=1409, Oh=1.72 · 10−2. (b) Splashing ethanol drops illuminated by a single flash. Drop diameter D=276 μm, impact velocity V0 =12.7m/s, We=1542, Re=2270, Oh= 1.73 · 10−2. From Yarin &Weiss (1995). Courtesy of Cambridge University Press.

As referred before the main factors influencing the drop impact dynamics include the parameters of the liquid drop such as the diameter (D), the impact velocity (v_o), the temperature and the liquid properties (viscosity μ_f, density ρ_f, and surface tension σ), the liquid film parameters (thickness, ho, film velocity v_{film}, composition, temperature, and features of underlying surface), and the surrounding gas (velocity, pressure, temperature, flow regime and gas properties of viscosity μ_g, and density ρ_g). The mentioned parameters can be used for forming dimensionless equations describing liquid layer impact dynamics. The important dimensionless groups describing the problem are mentioned above:

$$We = \frac{\rho_f D v_o^2}{\sigma} \quad (10) \qquad Re = \frac{\rho_f D v_o}{\mu_f} \quad (11) \qquad Oh = \frac{\mu_f}{\sqrt{\rho_f \sigma D}} = \frac{We^{1/2}}{Re} \quad (12)$$

$$\tau = \frac{v_o t}{D} \quad (13) \qquad Bo = \frac{\rho g D^2}{\sigma} \quad (14) \qquad Fr = \frac{v_o^2}{Dg} = \frac{We}{Bo} \quad (15)$$

Where We, Re, Oh, Fr, and τ denote Weber number, Reynolds number, Ohnesorge number, Froude number, and non-dimensional time, respectively. In general, gravity effects can be neglected for $Fr<10^2$ (Deegan, Brunet, & Eggers, 2008; Yarin, 2006). Two other pertinent parameters are the ratios of liquid–gas density and viscosity (Liang, Guo, & Shen, 2014) , which are defined as:

$$\rho^* = \rho_f / \rho_g \quad (16a)$$

$$\mu^* = \mu_f / \mu_g \quad (16b)$$

For the purpose of this thesis the gravitational forces are neglected and also there is no emphasis given on the parameters of the surrounding gas.

1.3 Crown formation phenomenon

1.3.1 Crown formation mechanism

The crown formation and characteristics are very important for understanding the phenomenon. Figure 1.5 reveals the transmutation of the formed liquid crown in case of spreading. The difference in impact speed versus that one in case of splashing is reflected on the lack of secondary features such as secondary droplets and capillary breakups. The shape of the crown is influenced by time and also the crown is no longer observed in case of very thin films (h < 1)(Rioboo et al., 2003).

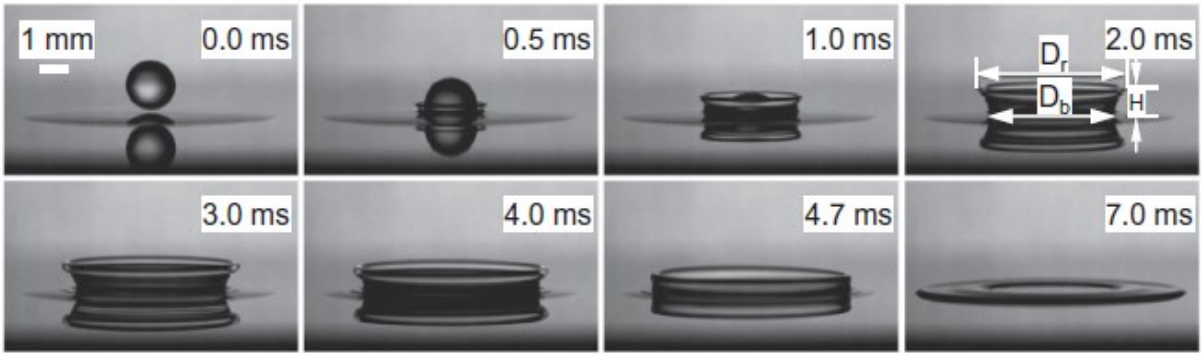

Figure 1.5: Temporal record of crown liquid sheet development of butanol for vdrop = 1.72 m/s and h≤0.05 (Liang & Mudawar, 2016).

When a liquid drop collides vertically with a liquid film, the fluid inside the drop is being redirected from vertical to radial axis. Yarin & Weiss (Yarin & Weiss, 1995), expressed that a kinematic discontinuity is formed as the fast redirected liquid meets the static liquid film, which contributes to the crown's formation and propagation. This theory has been widely accepted by many scientists and it has been a very important parameter for the numerical procedures and simulations trying to solve and represent the problem respectively (Coppola, Rocco, & de Luca, 2011). The theory has been also validated by experiments which have captured the discontinuity in liquid velocity. We should mention that the Yarin & Weiss theory does not account the effects of viscosity. Also, Levin & Hobbs enriched the crown formation theory by report that crown formation is greatly influenced by film thickness. Trujillo & Lee (Trujillo & Lee, 2001) used the discontinuity theory and also added the parameters of viscous forces on the evolution of the crown by making measurements for the liquid mass absorption by the crown with viscous and non-viscous constraints. However, following work by Roisman and Tropea (Roisman & Tropea, 2002) showed that the differences between the viscous theory of Trujillo & Lee and Yarin & Weiss were not significant and supposed that the main factor affecting the crown formation is the inertia of the liquid and not the viscous forces. Figure 1.6(b) shows crown formation resulting from kinematic discontinuity. In figure h1 and v1 represent film thickness and liquid velocity in the impact region, and h2 and v2 film thickness and liquid velocity in the static film region correspondingly. The thickness of the crown at the base and also the crown angle α were expressed by the following mathematical equations as:

$$h_b = h_1 + h_2 \qquad (17a)$$

$$\alpha = \arccos\left\{\frac{(h_1-h_2)(v_1-v_2)^2}{h_b(v_1-v_2)^2-(8\sigma)/\rho_f}\right\} \qquad (17b)$$

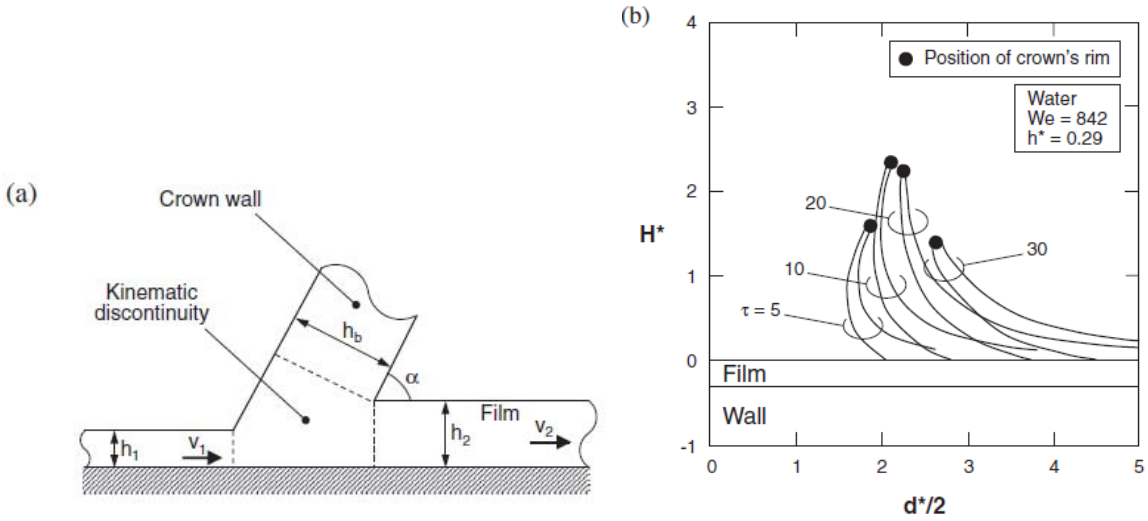

Figure 1.6: (a) Schematic of crown formation based on kinematic discontinuity. (b)Predicted shape of crown evaluation for water with We = 842 and h⁄ = 0.29 (96).

A list of complementary factors showed that they can affect the crown evolution as for example the density and viscosity of the surrounding gas (Guo & Wang, 2012; Liang, Guo, Yang, Guo, & Shen, 2013; Mukherjee & Abraham, 2007; Shetabivash, Ommi, & Heidarinejad, 2014) , the film velocity in case of flowing film (Alghoul, Eastwick, & Hann, 2011; Gao & Li, 2015; Raman, Jaiman, Lee, & Low, 2015), the shape of the drop before impact (Shetabivash et al., 2014) and also the shape of the solid surface sustaining the liquid film (Liang, Guo, Yang, Guo, et al., 2013; Liang, Guo, Yang, & Shen, 2014). Liang et al.(Liang, Guo, & Shen, 2014) predicted an incurve of the crown with decreasing density ratio, especially for density ratios of ρ*< 100, Figure 1.7(a), which they attributed to large gas velocity differences between crown's upper and lower levels They also showed that decreasing the liquid–gas viscosity ratio below μ*= 0.5 suppresses crown expansion, Figure 1.7(b), because of the combined effects of pressure difference and gas velocity in the drop-film neck region.

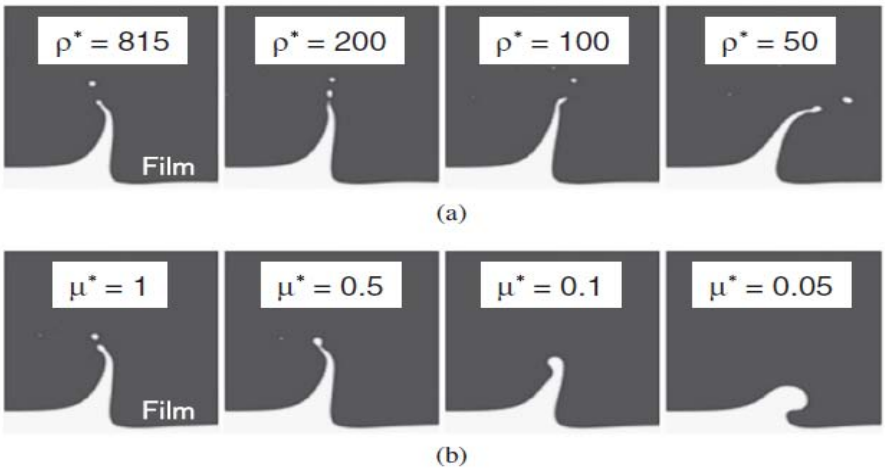

Figure 1.7: Effects of gas density (a) and viscosity (b) on crown shape for water with We = 693 and h≤ 0.3. Adapted from Liang et al (Liang, Guo, & Shen, 2014).

1.3.2 Crown Evolution, Diameter, Height, Angle

Following the evolution of the drop collision, the analysis of the crown film is crucial. The dominant analysis parameters based on geometrical criteria are the crown diameter D, height H, angle α, and thickness. In Figure 1.5 these basic geometrical characteristics of the crown are measured, they are symbolized as the base diameter of the crown Db and the rim diameter Dr. The average height of the liquid crown is also measured and mentioned as H. The height measurements are made from the base to the rim. Angle a, refers to the angle at the base. From an optical evaluation of impact images, we can clarify that the crown angle changes away from the base because of the crown wall's curvature. Yarin & Weiss (Yarin & Weiss, 1995) recommended a theoretical square-root dependence of non-dimensional crown diameter, D*, on non-dimensional time τ. the following equation describes the connection between those two parameters.

$$D^* = C(\tau - \tau_o)n\,, \qquad n = {}^1/_2 \tag{18}$$

Where τ_o corresponds to initial value on the moment of impact. The exponential number n is equal to 1/2 according to Yarin & Weiss (Yarin & Weiss, 1995). The use of Yarin & Weiss crown equation on experimental data was unsuccessful (Coghe, Brunello, Cossali, Marengo, & TeMPE-CNR, 1999), which shows that the equation is partially applicable to certain types of crown formation. most of the scientific correlations made by researchers during the last years are represented in the following table (Table 1.2). There is a variation in the values of exponent number n but, generally, in most cases, the number is slightly lower than the Yarin & Weiss number. Additionally, Cossali et al. (Cossali, Marengo, Coghe, & Zhdanov, 2004) found that, while the coefficient C is independent of the film thickness, it is not constant but slightly changeable based on the impact velocity.

The crown formation is a sustainable idea it can be also based on the dimensionless numbers of Reynolds and Weber. This dependence has been investigated by Liang et al. (Liang, Guo, Shen, & Yang, 2014) and specifically the dependence of crown size based on Reynolds and Weber numbers by varying impact velocity and also physical properties separately. They discovered that the crown

diameter is independent of We and Re. This conclusion has been also verified by the following works of Rieber and Frohn (Rieber & Frohn, 1999) and Josserad and Zaleski (Josserand & Zaleski, 2003). In addition, Fujimoto et al. (Fujimoto, Ogino, Takuda, & Hatta, 2001) based their research in numerical simulations in order to conclude that surface tensions reduce the crown's liquid sheet. The non-dimensional thickness of the liquid film h*, plays also a significant role in crown diameter. The increment of crown diameter causes a reduction of non-dimensional height is supported by a wide group of researchers. The idea is based on the decreased energy dissipation and liquid mass (Liang, Guo, Shen, et al., 2014; Trujillo & Lee, 2001). However theoretical studies had shown the opposite (Rieber & Frohn, 1999; Yarin & Weiss, 1995). Cossali et al. (Cossali et al., 2004) and Lee et al. (Lee, Hur, & Kang, 2011) suggested that crown diameter is slightly dependent on h*. Mukherjee and Abraham (Mukherjee & Abraham, 2007) concluded that crown diameter grows with increasing film thickness for thin films (h* < 0.25), but decreases for thick films (0.25 < h*< 2). The difference on the result is caused by more of the impact drop's energy being absorbed by the thick film (Mukherjee & Abraham, 2007).

Table 1.2: Correlations of crown Diameter (Liang & Mudawar, 2016).

Author(s)	Fluid(s)	Test conditions	Correlation(s)
Yarin and Weiss	Ethanol or mixtures of ethanol, glycerol, and water	d_{drop} = 70–340 μm, v_{drop} up to 30 m/s	$D_r^* = \frac{2v_f^{1/2}}{6^{1/4}\pi^{1/2}v_f^{1/8}d_{drop}^{1/4}f^{3/8}}(\tau-\tau_0)^{1/2}$ simplified to $D_r^* = 2\left(\frac{2}{3h^*}\right)^{1/4}(\tau-\tau_0)^{1/2}$
Cossali et al.	Distilled water	d_{drop} = 3.82 mm ± 4%, v_{drop} = 2.3–4.4 m/s, h = 1.1–4.3 mm, h^* = 0.29–1.13	$D^* = C(\tau-\tau_0)^{0.43\pm0.03}$, $\tau_0 = 0$–1.5
Rieber and Frohn	Water–air system, ρ^* = 1000, μ^* = 40	We = 250, Oh = 0.0014, h^* = 0.116	$D_r^* = 2.44\tau^{0.406}$, $D_b^* = 2.116\tau^{0.459}$
		We = 598, Oh = 0.0014, h^* = 0.116	$D_r^* = 2.30\tau^{0.441}$, $D_b^* = 2.130\tau^{0.444}$
Trujillo and Lee	Ethanol	d_{drop} = 3.4 mm, v_{drop} = 1.3 m/s, h^* = 0.25	$D_r^* = C\tau^{1/2}$
Davidson	Water	We = 20–400, h^* = 0.1–0.5	$D_b^* = C\tau^{1/2}$
Xie et al.	Glycerol–water solution	We = 2010, Oh = 0.0384, h^* = 0.5	$D^* = 0.01826(\tau+0.4)^{1/2}$ for crown's inner diameter
Guo et al.	Water	d_{drop} = 2 mm, v_{drop} = 2.75–4.32 m/s, h^* = 0.3–0.7	$D_r^* = C\tau^n$, n = 0.469, 0.447and 0.435 for h^* = 0.3, 0.5 and 0.7, respectively

According to the crown height the model made by Roisman & Tropea reveals that non-dimensional crown height H*= H/D increases by increasing h* correspondingly. However, this result has been questioned from later experiments made by Cossali et al. (Cossali et al., 2004) which revealed a strong dependence of crown height evolution on Weber number and a less important contribution of non-dimensional h*. Later experimental work made by Davidson (Davidson, 2002), the crown height achieved at a given instant increases with increasing h*. Furthermore, Mukherjee and Abraham (Mukherjee & Abraham, 2007) identified different crown height patterns for non-dimensional film heights lower than 0,25 (h* < 0,25), versus those for thicker films (h*> 0,25). Using an energy balance, Macklin and Metaxas (Macklin & Metaxas, 1976) derived a relation between maximum crown Height, H_{max} and maximum diameter of the cavity $D^*_{C\text{-}max}$, beneath the crown.

$$H^*_{max} = \frac{1+We^{-1}+2Fr^{-1}-3We^{-1}h^*D^*_{C-max}}{6We^{-1}D^*_{c-max}} \qquad (19)$$

Cossali et al. (Cossali et al., 2004) maintained that non-dimensional maximum Height H^*_{max} and corresponding non-dimensional time τ_{max} depend on impact velocity but are weakly effected by film thickness h*. They also formed correlations for H^*_{max} and τ_{max} of the form CWe^n with parameter n limiting between 0,65 and 0,75 (0,65<n<0,75) (Cossali et al., 2004). Contrarily, Asadi and Passadideh-Fard (Asadi & Passandideh-Fard, 2009) proposed their correlations for the variables of H^*_{max} and τ_{max} (We=296-1020). The mathematical equations that had been formed are:

$$H_{max} = 0{,}0025\ We \quad (20a) \qquad \tau_{max} = 0{,}0037We^{1,2} \quad (20b)$$

In addition to crown angle, the theoretical model by Roisman and Tropea (Roisman & Tropea, 2002) mentioned before, resulted in the crown angle relation by Equation (17b). Unfortunately, the term of liquid velocity in the liquid film found in equation is difficult to measure. Wang and Chen (Wang & Chen, 2000) noted that the crown wall, or the liquid crown sheet, is almost perpendicular to the horizontal liquid film (α=90˚)covering the solid surface, for h ≤ 0.5. Afterword, Fedorchenko and Wang (Fedorchenko & Wang, 2004) supported that film thickness determines the crown angle, independent of impact velocity or liquid properties. They concluded that, in the initial stages of crown emergence, α=90˚ for h*≥ 0,25 but for very thin films with h ≤ 0,25 the crown angle can be determined with the following mathematical form:

$$\cos(\alpha) = 1 - 4h^* \qquad (21)$$

When the drop collision velocity is significantly high the splashing phenomena are observed on the input outcome. From an optical scope, the basic characteristics of collision are the formation of secondary drops, known as droplets. The droplets emerge from the highest part of the liquid crown sheet, the crown rim. The phenomenon of splashing is very important in the fields of atomization, or even coating processes such as ink jet printing. Significant work on splashing was been made by Cossali et al. (25). Cossali categorized splashing into two types, known as prompt and delayed splashing. In case of prompt splashing droplet ejection from crown rim happens when the crown is still growing as shown for methanol drop impact in Figure 1.8. Additionally, delayed splashing occurs near or after the crown reaches maximum height, and it's associated with instability and breakup of crowns rim. Prompt splashes are shown in Figure 1.8 for butanol and propanol. Delayed splashing can be also observed in the final stages of prompt splashing as in the case of methanol in Figure 1.8.

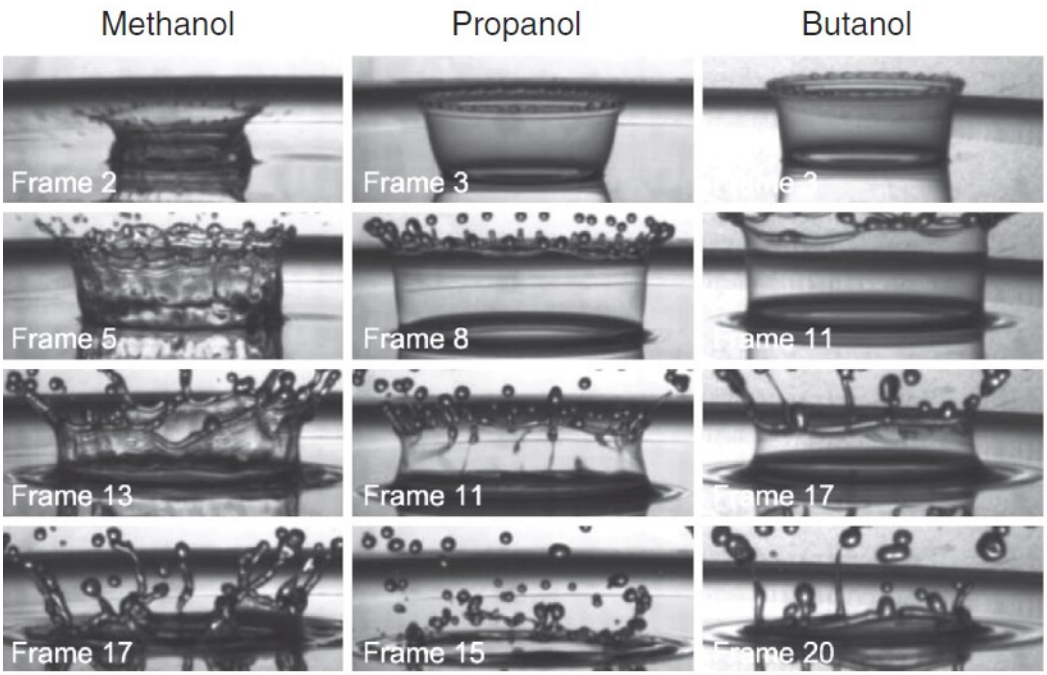

Figure 1.8: Prompt splashing in methanol drop impact, and delayed splashing in propanol and butanol drop impact for D_{drop} = 2 mm, $h/$ = 0.1 and V_{drop} = 3.15 m/s. Adapted from Vander Wal et al. [23].

1.4 Splashing mechanism

1.4.1 Splashing types

When the drop collision velocity is significantly high the splashing phenomena are observed on the input outcome. From an optical scope, the basic characteristics of collision are the formation of secondary drops, known as droplets. The droplets emerge from the highest part of the liquid crown sheet, the crown rim. The phenomenon of splashing is very important in the fields of atomization, or even coating processes such as ink jet printing. Significant work on splashing was been made by Cossali et al. (Cossali et al., 1997). Cossali categorized splashing into two types, known as prompt and delayed splashing. In case of prompt splashing droplet ejection from crown rim happens when the crown is still growing as shown for methanol drop impact in Figure 1.8. Additionally, delayed splashing occurs near or after the crown reaches maximum height, and it's associated with instability and breakup of crowns rim. Prompt splashes are shown in Figure 1.8 for butanol and propanol. Delayed splashing can be also observed in the final stages of prompt splashing as in the case of methanol in Figure 1.8.

Basic parameters influence the splashing are viscosity and surface tension. Experimental work has been carried out by Cossali et al. (Cossali et al., 1997), Motzkus et al. (Motzkus, Gensdarmes, & Géhin, 2011) and Liang et al. (Liang, Guo, Yang, Zhen, & Shen, 2013). They pointed out that prompt splashing takes place in low Ohnesorge number values (low viscosity) situations, while high Ohnesorge situations (high viscosity) result in delayed splashing. Relatively to droplet size, secondary droplets in prompt splashing are much smaller than those in delayed splashing (Motzkus et al., 2011). Vander Wal

et al. (Vander Wal et al., 2006) conducted extensive experiments with different liquids to assess the influence of liquid properties on splashing. They observed that high surface tension inhibits splashing regardless of whether the target is dry or covered with a thin liquid film. Later work from Liang et al. (Liang, Guo, Yang, Zhen, et al., 2013) confirmed the results of Vander Wal et al. Contrarily, viscosity reveals different effects for a dry versus wet surface, promoting splashing on the dry surface but resisting splashing for droplet impact on a thin film (Vander Wal et al., 2006).

1.4.2 Mechanisms of splashing

When we refer to splashing mechanisms splashing threshold is a crucial parameter. The threshold parameter above certain values corresponds with the formation of secondary droplets. The effect of surface tension is crucial and is therefore expressed in terms of either non-dimentional Weber number alone or with the collaboration of other parameters. Studies reveal that the threshold We is influenced by both viscosity and film thickness. Based on Figure 1.9 we can conclude that the influence of viscosity is reflected in the threshold We which increases with equivalent increasing of Ohnesorge number (Asadi & Passandideh-Fard, 2009; Cossali et al., 1997; Pan & Hung, 2010; Wang & Chen, 2000). The matter of film thickness influence reveals differentiations among scientists. Cossali et al. (Cossali et al., 1997) pointed out that threshold We reveal incensements among with the augmentation of the h*. these results had been confirmed later by Rioboo et al. in the case of thin films (Rioboo et al., 2003). However, other investigators suggested the threshold We seem independent of h* for thin films with h* < 0.1 (Asadi & Passandideh-Fard, 2009; Liu, Vu, Yoon, Jepsen, & Aguilar, 2010; Wang & Chen, 2000)

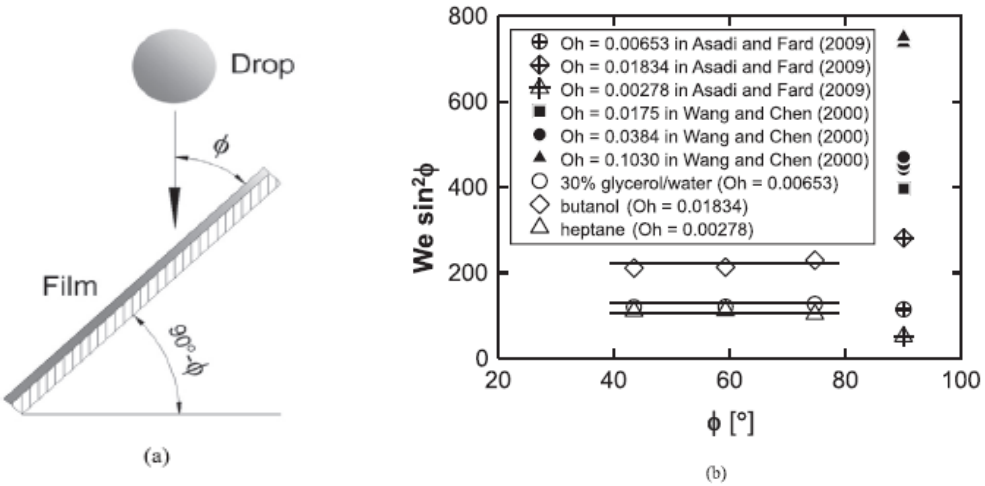

Figure 1.9: (a) Schematic of drop impact on inclined wetted wall, and (b) variation of modified Weber number for splashing threshold with impact angle for different values of Oh. Adapted from Liang et al. [117].

However, knowing that surface tension and viscosity have a strong influence on splashing thresholds, even for low viscosity liquids the use of threshold We seem insufficient. A preferable method is to use K-type correlations combining both the inertial force of the impacting drop with the viscous and surface tension forces represented by Ohnesorge or Reynolds and Weber numbers correspondingly. The film thickness described by the h* term is also used in the K-type correlations. Some important correlations found by researchers over the last decades are presented in table 3. Notice that, while the majority of correlations are based solely on We and Oh, a few (Cossali et al., 2004; Motzkus et al., 2011) also account for h*. Motzkus et al. (Motzkus et al., 2011) used their experimental data to assess the predictive accuracy of some of the correlations in Table 1.3. Their comparisons of data to correlations are shown in Figure 1.10(a)~(d) in the form of threshold We versus h* for Oh = 2.4×10^{-3}, 6.8×10^{-3}, 9.5×10^{-3} and 1.5×10^{-2}, respectively. The data are segregated according to delayed slashing (D), prompt splashing (P), and coalescence (C).

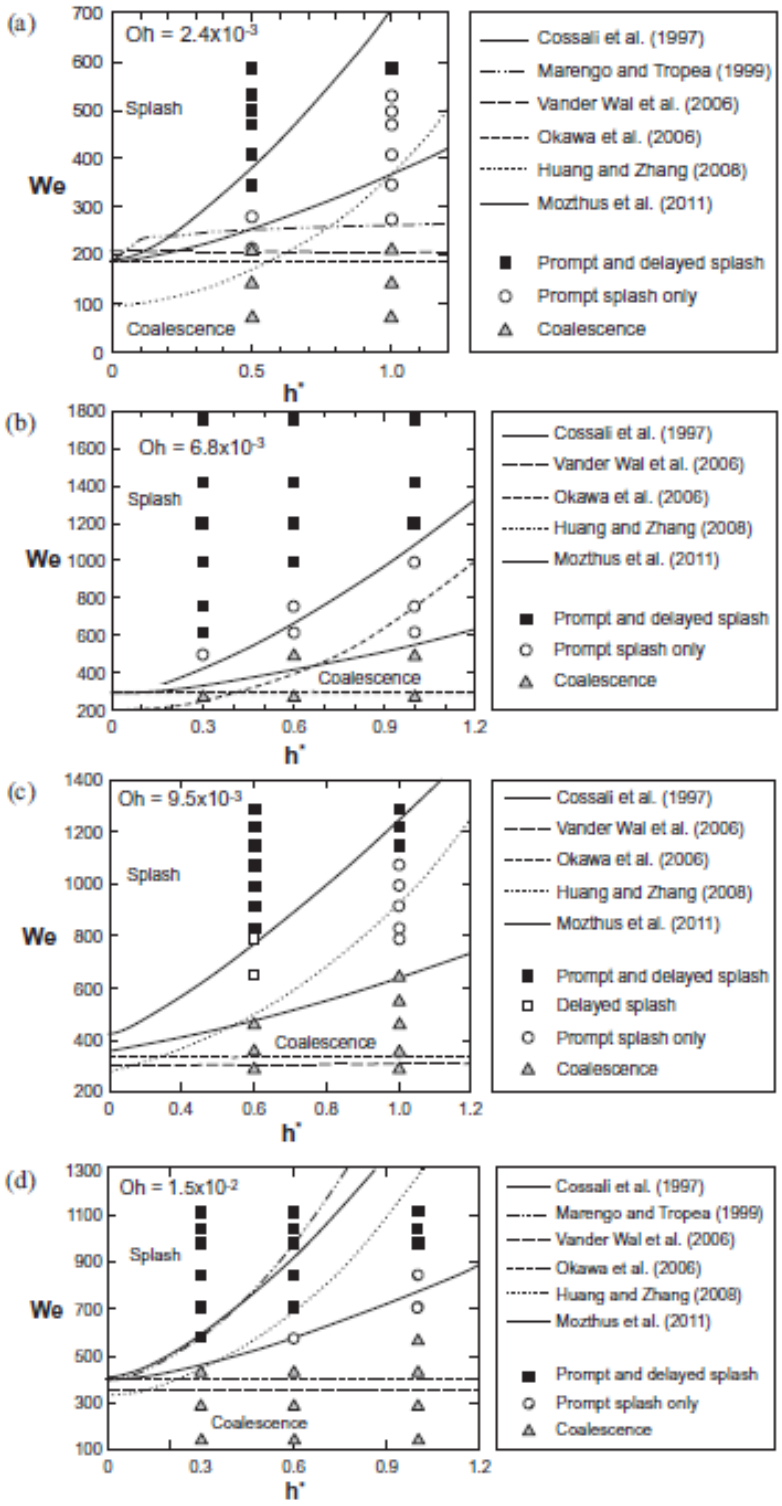

Figure 1.10: Comparison of different splashing thresholds for (a) Oh = 2.4 x 10^{-3}, (b) Oh = 6.8 x 10^{-3}, (c) Oh = 9.5 x 10^{-3} and (d) Oh = 1.5 x 10^{-2}. Adapted from Motzkus et al. (Motzkus et al., 2011).

Table 1.3: Correlations for critical K required to initiate splashing into small droplets.

Author(s)	Fluids	Test conditions	Correlation(s)
Walzel	Glycerol–water mixtures	$h^* = 0.1$	$K = We\,Oh^{-0.4} = 2500$
Yarin and Weiss	Ethanol, ethanol–glycerol–water mixtures	d_{drop} = 70–340 μm, v_{drop} up to 30 m/s	$v_{drop} = \left(\frac{\sigma}{\rho_f}\right)^{1/4} \nu_f^{1/8} f^{3/8}$ simplified to $K = We\,Oh^{-0.4} = 2400$
Cossali et al.	Water, glycerol–water mixtures	d_{drop} = 3.07 ± 0.07–3.51 ± 0.06 mm, $We = 2 \times 10^2$–1.6×10^3, $h^* = 0.1$–1, $Oh > 7 \times 10^{-3}$	$K = We\,Oh^{-0.4} = 2100 + 5880h^{*1.44}$
Marengo and Tropea	Water	–	$K = We\,Oh^{-0.4} = 2074 + 870h^{*0.23}$
	μ_f = 50 mPa s	$Oh > 0.01$	$K = We\,Oh^{-0.4} = 2164 + 7560h^{*1.78}$
Rioboo et al.	Glycerol–water mixtures, hexadecane, $PDMS_5$, $PDMS_{10}$	We = 28–890, $h^* > 0.06$, $Oh = 1.14 \times 10^{-2}$–5.48×10^{-2}	$K = We\,Oh^{-0.4} = 2100$
Okawa et al.	Water	We = 2.5–980, h^* = 0.4–68, $Oh = 1.5 \times 10^{-3}$–7×10^{-3}	$K = We\,Oh^{-0.4} = 2100$
Vander Wal et al.	Heptane, nonane, decane, dodecane, tetradecane, hexadecane, deionized water, 30% glycerol/water, methanol, ethanol, n-propanol and butanol	$Re = 5 \times 10^2$–5×10^3, $Oh = 10^{-3}$–2.2×10^{-3}	$K = Oh\,Re^{1.17} = 63$
Huang and Zhang	Water, oil	h^* = 0.1–1, ρ_f = 854–998 kg/m^3, μ_f = 1–22.5 mPa s, σ = 0.029–0.072 N/m	$K = (We\,Re)^{0.25} = 25 + 7h^{*1.44}$
Motzkus et al.	Water, glycerol–water mixtures	We = 62–1754, h^* = 0.3–1, $Oh = 2 \times 10^{-3}$–1.5×10^{-2}	$K = We\,Oh^{-0.4} = 2100 + 2000h^{*1.44}$
Gao and Li	Water, glycerin–water mixtures	$h^*\nu^*_{film}$ = 0.05–0.18, μ_f = 1–46.47 mPa s, σ = 0.0657–0.0714 N/m	$K = We\,Re^{0.5} = 3378(1 + h^*\nu^{*2}_{film})^{-1}(1 + h^*\nu^*_{film})^{-0.5}$

1.4.3 Additional kindred phenomena, Jets formation and secondary droplets

Trying to list the instability phenomena governing the droplet impingements, secondary droplets reveal an important role. Deegan et al. (Deegan et al., 2008) found three sources of secondary droplets with very case revealing a different type of instability. The three instability cases can be listed as prompt instability of the ejecta, rim instability of the ejecta sheet that forms very small droplets and last rim instability of the crown sheet that produces jets followed by large droplets. The third type of instability is presented in Figure 1.12. Several conclusions have been made by researchers over the last decades. Specifically, the number of jets generated along the corona rim, reveals abatement characteristic time values of $0 < \tau < 8$. However, a stabilization occurs in jet number to about 10, independent of film thickness and impact velocity (Yarin & Weiss, 1995)(Cossali et al., 2004; Yarin & Weiss, 1995). According to Engel (Engel, 1967) the total volume of secondary droplets is equal to 2-4 times the volume of the impinging drop they also assumed that only 5% of the impinging drop's kinetic energy is absorbed by secondary droplets. Okawa et al. (Okawa, Shiraishi, & Mori, 2008) reported that impingement angle effects the number of secondary droplets. Angle numbers higher than 40˚, leads to a substantial increase in the total mass of secondary drops. Cossali et al. by carrying out experiments they realized that, for high viscosity liquids, secondary droplets detach from the crown rim only after its full development. For low viscosity liquids, the secondary droplets formed on the top of the initial jets. Surface tension also effects the mechanism of secondary droplets. By increasing surface tension, the number of secondary droplets is reduced (Davidson, 2002). The same results have been produced by increasing the liquid velocity. Gregory et al. (GREGORY, GUTHRIE, & BUNCE, 2009) showed that the number of secondary droplets increases with decreasing film thickness. Allen also found that he

ejecting angle of secondary droplets depends on h*. Some of the correlations for the number of secondary droplets made by scientists are presented in the following Table 1.4. Trying to evolve the generating mechanism of secondary droplets, the model of Rayleigh-Plateau capillary instability formed. According to Rayleigh-Plateau mechanism the cylindrical jets formed on the crown rim break into droplets, because of surface tension. The mechanism has been also supported with later works made by Bremond and Villermaux (Bremond & Villermaux, 2006) and also Lagubeau et al. (Lagubeau et al., 2010). Deegan et al. (Zhang, Brunet, Eggers, & Deegan, 2010) verified the Rayleigh-Plateau mechanism by measuring the spectrum of small-amplitude perturbations growing on the rim. Finally, a schematic representation of the phenomenon is shown in Figure 1.11.

Table 1.4: Correlations for number of secondary droplets (Liang & Mudawar, 2016).

Authors	Fluids	Test conditions	Correlation
Yarin and Weiss	Ethanol, mixtures of ethanol, glycerol and water	d_{drop} = 70–340 μm, v_{drop} up to 30 m/s	$N = \frac{15\pi D^*}{4.5}$
Cossali et al.	Water	d_{drop} = 3.82 ± 4% mm, v_{drop} = 2.3–4.4 m/s, h = 1.1–4.3 mm, h^* = 0.29–1.13	$N = C\tau^n$, n increases with increasing We
Okawa et al.	Water	We = 2.5–980, $Oh = 1.5 \times 10^{-3}$–8.4×10^{-3}, h^* = 0.43–68	$N = 7.84 \times 10^{-6} K^{1.8} h^{*-0.3}$, where $K = We\ Oh^{-0.4}$

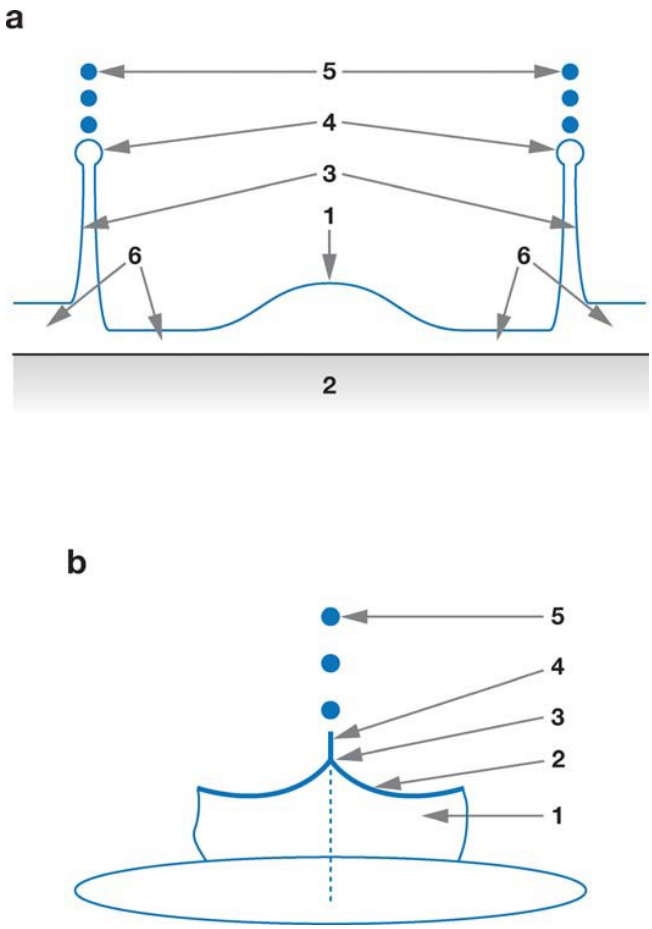

Figure 1.11: Sketch of splashing mechanism: (1) residual top of impacting drop (2) wall (3) section of crown-like sheet propagating outward (4) cross-section of free rim (5) secondary droplets formed from cusps of free rim (6) liquid

layer on wall. (b) Free rim and secondary droplets magnified (1) crown-like sheet (2) free rim at its top edge (3) cusp (4) thin jet emerging at cusp (5) secondary droplets formed on breakup of jet. From Yarin &Weiss (1995). Courtesy of Cambridge University Press.

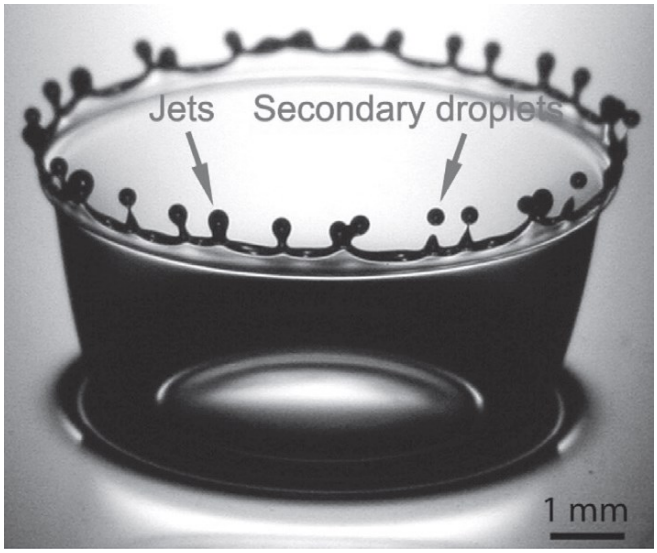

Figure 1.12: Jets and secondary droplets in splashing of silicone oil drop with Re = 966, We = 874 and h⁄ = 0.2. Adapted from Zhang et al. (Zhang et al., 2010).

1.5 Thesis aim

The present thesis focuses on the possible outcomes of a collision between a droplet and an already wetted (or partly wetted) flat solid surface. It is an attempt to explain the splashing phenomenon on this specific regime as well as another effort to supplement the already growing field of studies on the general droplet-particle subject and to arise some questions for upcoming studies as well. We conducted experiments using water droplets impinging aluminum plates with different impact angles (10˚ 20˚ and 30˚). The role of surface roughness Ra is also examined in the following thesis by using aluminum plates with different scales of roughness (Ra). By changing the geometrical parameters, and subsequently the aforementioned dimensionless numbers, we were able to qualitatively determine how they affect the collision outcome in each case. We focused on the transition from deposition to splashing of the droplet and tried to explain the created liquid shapes accordingly. The image results were further analyzed with the assistance of Matlab for impact tracking. Image measurements have been made using ImageJ in order to pinpoint the basic impact characteristics such as the crown diameter. We reached many conclusions that are listed in detail as well as some questions for further analysis.

The structure of the thesis is as follows, in section 2, the experimental arrangement is presented. In section 3, we present and analyze the results of the measurements. The thesis closes with a summary of the main findings and suggestions for future work.

2. Methods

In order to study the droplet collision with the different surfaces an experiment had to be carried out. The experiment consisted of some solid tiles, each of different roughness, a syringe that formed the falling droplets, a powerful light source to illuminate the experiment and a high speed camera to capture the phenomenon. We would change the angle of the solid surface in relation to the horizontal axis and the height of the syringe in order to see the how the effect of the angle and the distance between the syringe and the surface would change the outcome.

The surfaces we decided to use were aluminium alloy tiles that were placed in three different angles in relation to the horizontal axis. The angles we studied were 10, 20 and 30 degrees with respect to the horizontal x-axis. We decided to use water as the liquid. The falling droplets were released from a syringe held in different heights. The heights we studied, measured from the centre of the tiles, were 19cm, 29cm, 39cm, 49cm, 59cm and 69cm. By conducting the same experiment in three different angles and 6 different distances, the images revealed the similarities and the differences between each case. The experimental set up can be seen in Figure 2.1.

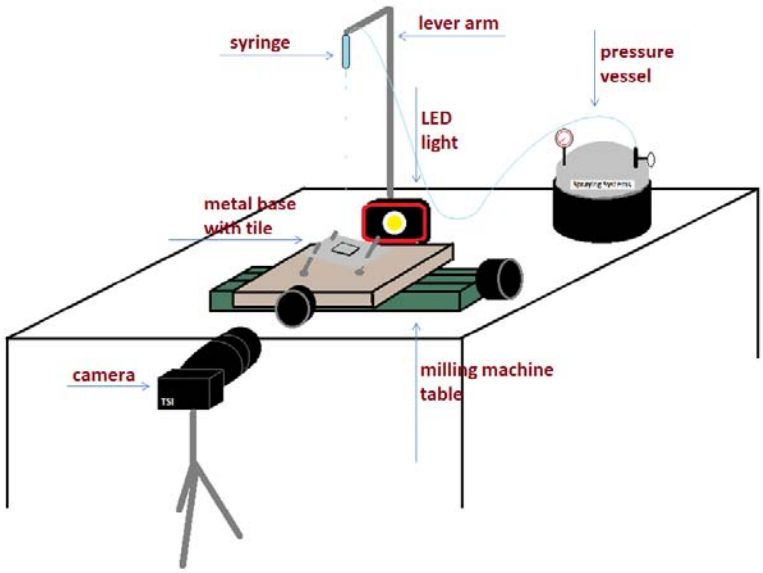

Figure 2.1: Experimental set up

2.1 Experimental Set up

2.1.1 Surfaces

The used surfaces were three square aluminum alloy 2024 tiles with dimensions 4cmx4cm and 2mm thickness. Each one of them had the necessary process with a certain abrasive wheel in order to acquire a requested roughness. The roughness has been measured with Mitutoyo Surftest 211. The tiles were then placed on a small metal base with three threaded legs. By adjusting each leg's position (screwing or unscrewing them) the base could change its angle with respect to the x axis, as can be seen in Figure 2.2. The base was placed on top of a milling machine table. The table was originally installed on top of a moving saddle that had the potential of moving both in x and y axis by using the corresponding handwheels (Figure 2.3). This way it was ensured that we could change the position of the particle with great accuracy.

Figure 2.2: Metal base

Figure 2.3: milling machine table with the moving saddle

2.1.2 Droplets

In order to form droplets, we chose a typical syringe of 10mL 21G X 1 1/2" with a 0.8mm needle outer diameter. By currying out many tests, it was obvious that the needle was constantly changing the way the droplets departed from it and therefore the place it landed, so we decided to use the syringe without the needle. The syringe was held in place via a stable arm with a grapple which was placed behind the milling machine table. The arm had screws that allowed us to move the grapple vertically in order to adjust the distance between the syringe and the tiles. Since the droplet would perform a free fall under gravity with zero initial velocity, the distance to the target would affect the impact velocity and therefore the post impingement behavior. To find out the height from which the droplet would reach its terminal velocity, some calculations had to be carried out.

When an object falls vertically there are two forces acting upon it. The gravity which is represented by the weight force (Fw) and the drag force (Fd) which is the resistance of the air. Considering a water droplet as a sphere (Figure 2.4), and given the fact that the droplet has no horizontal velocity, those two forces are opposing. The definition of the forces is described below.

$$F_w = mg,$$

Where m is the droplet mass, and g the standard acceleration due to gravity which is equal to 9.8 m/s^2 on earth.

$$F_d = \frac{1}{2}\rho v_d^2 A C_d,$$

Where ρ is the air density, v_d is the droplet velocity, A is the projected area of the droplet on a surface perpendicular to the motion and C_d is the drag coefficient.

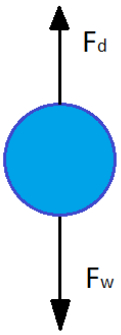

Figure 2.4: Free falling droplet

At the beginning the gravitational force is greater than the drag force and therefore the droplet accelerates but, during the free fall, the drag force is constantly increasing due to the increasing velocity. At some point the two forces will equalize and at that point the droplet has reached its terminal velocity. Therefore, to find the terminal velocity:

$$F_w = F_d \leftrightarrow mg = \frac{1}{2}\rho v_{d,t}^2 A C_d \leftrightarrow v_{d,t} = \sqrt{\frac{2mg}{\rho A C_d}} (1)$$

For the droplets of our experiment, the diameter was calculated from the experiment images. During the fall the droplets had a small oscillatory motion in the direction of the fall and thereby they were not perfect spheres in every image. Nevertheless, considering them as perfect spheres, an average diameter of 4.9mm was measured. In order to find the water mass, the exact volume of a sphere was calculated.

$$V = \pi \frac{d_d^3}{6} = 61.6\, mm^3$$

$$m = \rho V = 61.6 \cdot 10^{-6}\, kg$$

The projected area of a sphere on a surface regardless of its direction is a circle area.

$$A = \pi \frac{d_d^2}{4} = 18.86\, mm^2$$

The air density in standard conditions (about 25°C in the lab) is 1.2 kg/m^3. Considering a drag coefficient for a round sphere with a value of 0.5 the terminal velocity is found:

$$(1) \rightarrow v_{d,t} = 10.33\, \frac{m}{s}$$

We know the droplet will perform a free fall with zero initial gravity, since it departs from the syringe a few moments after its creation. The laws for the free fall are the following:

$$v_d = gt\ (2)$$

$$x = \frac{1}{2} g t^2\ (3)$$

$$(2), (3) \rightarrow x_{max} = \frac{v_{d,t}^2}{2g} \rightarrow \boldsymbol{x_{max} = 5.5\, m}$$

So we can ensure that within the lab limits (the syringe could not reach more than 1 m from the target) the droplet would never reach its terminal velocity and therefore the always changing distance between the syringe and the particle did change the collision outcome.

In order to feed the syringe with a constant water supply, we used a pressure vessel, specifically the Spraying Systems 22140 which we connected to the syringe via a typical rubber hose. This specific vessel was manufactured from stainless steel and could take 3 lt of liquid. A pressure regulator valve could fluctuate the pressure inside from 0.3 to 8.5 bar and a ball valve controlled the liquid supply. By constantly adjusting the supply and regulating the pressure we had the ability to feed more or less water to the syringe which meant more or less droplets in a certain time interval would depart from the syringe. The vessel can be seen in Figure 2.5.

Figure 2.5: pressure supply system

2.1.3 Camera

The phenomenon of the collision takes place within a few milliseconds. In order to capture the droplet at exactly the time of the collision, we needed a camera able to take pictures with the lowest possible exposure. The first attempt was with a Mako U-503 which is an ultra compact, monochrome USB3 Vision camera that has an ON Semiconductor (Aptina) MT9P031 CMOS sensor with rolling shutter. The camera was placed on a Velbon tripod which provided the ability to move vertically as well as to turn horizontally and tilt on both these two directions. We used the Vimba Viewer program in order to plug the camera into the computer which gave as live image footage of the experiment and allowed us to take different sequences of pictures. The lowest possible shutter speed of the camera was 30μs. With that fixed, the pictures were very dark and therefore we needed a strong light source in order to illuminate the experiment and have bright enough pictures for further processing. The illumination is described thoroughly in the next section.

In order to study the morphology of the phenomenon while it evolved, we needed images during the three faces of the phenomenon, which means the camera had to take pictures in the beginning of the collision, during the formation of the crown and during the final stages of its collapsing. The problem we faced was that there was no available way to synchronize the camera with the falling droplet in order to take certain pictures in specific times. Therefore, for each experiment, we had to take a sequence of images at random moments and choose the images that contained any of the aforementioned phases, afterwards.

After we carried out many experiments and collected a sufficient number of images, we kept only those that depicted either the formation of the crown, or the evolution of the splashing. By observing them carefully we found out that most of the images were slightly deformed in a way that the depicted crowns had a strange inexplicable shape on the two sides (Figure 2.6). That was attributed to a camera recording method which is called rolling shutter. This is the function were a picture is not captured by a single snapshot of the entire scene at a single moment but by scanning across the screen rapidly. In a phenomenon that takes place in a matter of milliseconds, the vertical scanning of our camera was

slow enough to cause the deformation. We conducted the same test placing the camera at 90° and the results, shown in Figure 2.6, confirmed our hypothesis. This meant that none of the images was reliable for further processing and therefore we had to change the equipment and start over again.

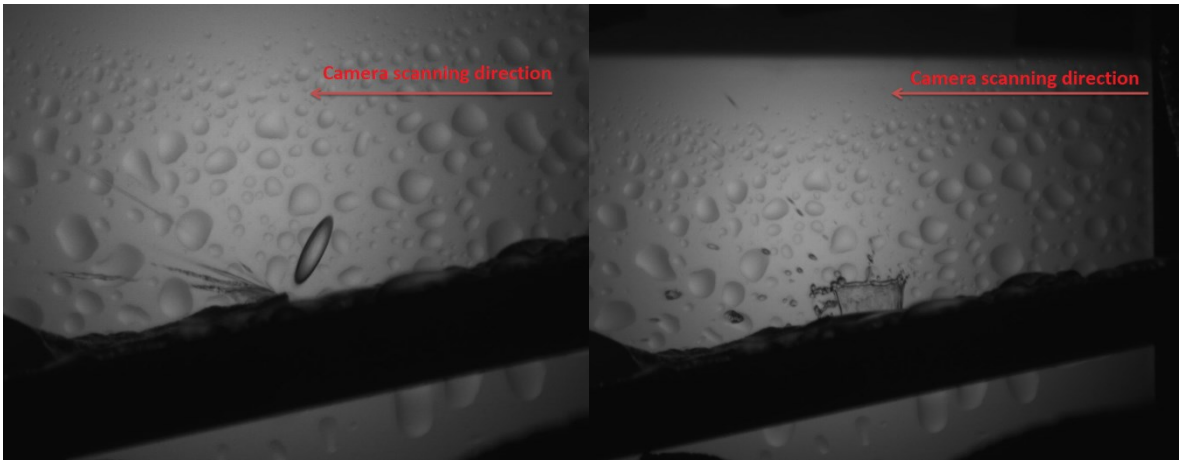

Figure 2.6: Deformed images

The other available camera in the lab was the TSI powerview plus HS-200. This is a high frame rate camera with 2048x2048 pixels resolution and 12-bit intensity dynamic range. We adapted a SIGMA 70-200mm F.2.8 APO, fixed zoom lens on it for the best possible results. The camera was placed on a tripod which provided the ability to move in every direction.

We used the insight 3D program to plug the camera in the computer, which allowed us to have live image from the experimental set up. We chose a shutter speed of 200μs in order to capture the phenomenon as clear as possible. The camera can be seen in Figure 2.7.

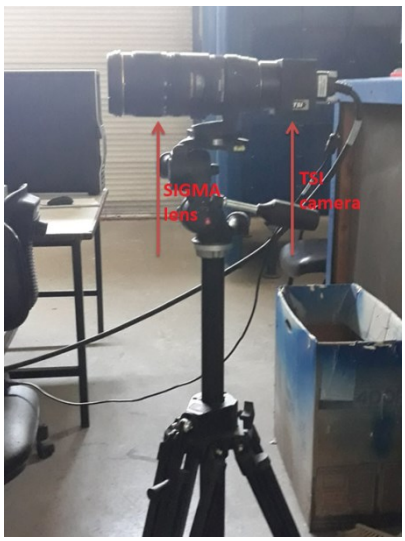

Figure 2.7: Camera

2.1.4 Illumination

Finding a strong light for the experiment was difficult. At the beginning we tried to use typical LED lights that needed alternating current from the sockets in the lab. The problem was that the constantly, sinusoidal changing current caused the light to turn on and of instantly with a certain frequency. The result in the image was what is called flickering, namely some dark lines on the screen that move upwards or downwards depending on the relative frequency between the light source and the camera's frame rate (Figure 2.8). Even by changing the camera's acquisition frame rate to suit the frequency of the currents, the dark lines did not disappear rather than remained stationary on the screen.

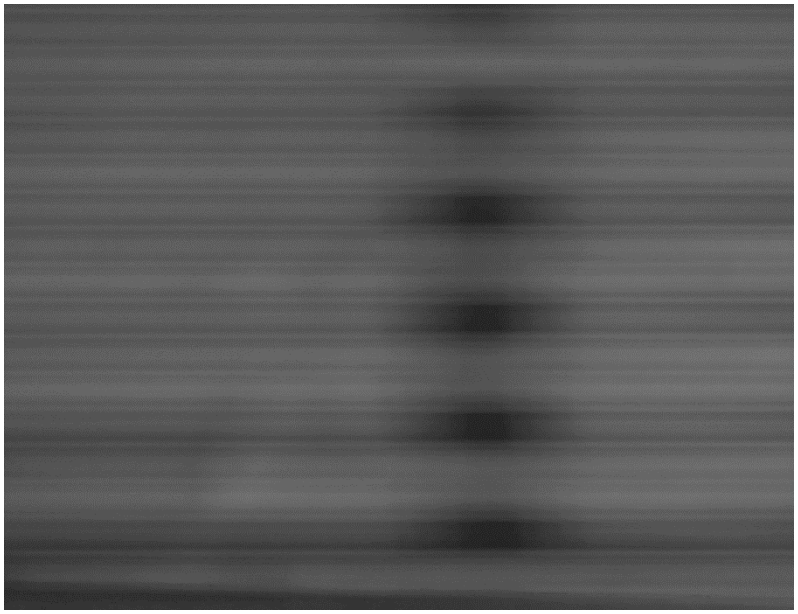

Figure 2.8: Flickering effect

The problem was solved by using an LED headlight with batteries, in order to have direct current and consequently steady light. The one we used was the daylight worklight XW 750 by Dekton which provided 450 lumens and a beam distance of 100 m. We assembled a split arm which we bolted on the milling table in order to hold the light in place behind the base with the tiles, aligned with the camera. Because of the extreme brightness that was a potential danger for the lens, a diffuser was used in order to reduce the intensity of the light by scattering it. Many glasses were tried but we ended up with the solution of a square piece of frosted plexiglass 9x9.

2.2 Properties

The alloy tiles that were used in the experiment were processed in order to form three surfaces with different roughness. The roughness of each one of them was measured after the process in different positions on the surface. For the experiments we considered an average roughness in each tile. The results can be seen in Table 2.1.

Table 2.1: Roughness table Ra (μm).

	Tile 1	Tile 2	Tile 3
Roughness 1(μm)	0,09	0,99	8,83
Roughness 2(μm)	0,07	1,25	6,58
Roughness 3(μm)	0,09	2,08	7,57
Roughness 4(μm)		1,50	6,68
Roughness 5 (μm)		1,03	5,23
Roughness Av(μm)	0,09	1,37	6,99

The three tiles were kept stable while the droplets fell on them from 6 different heights. In order to relate the different heights with the droplet's features, each one of the six heights was matched to a certain droplet We number. For this to happen, the velocity of the droplets in each case had to be measured first. Although we already had a velocity value for each height (see 2.1.2.), the theoretical analysis of the free fall had two major problems. First it did not take the drag resistance from the air into consideration, and secondly, it regards the droplet as a point object, with no actual dimensions. In reality the droplet is obviously not a point object, it has dimensions and furthermore, because it is not solid, it doesn't perform a free fall, but does an oscillatory motion while in the air.

In order to measure the droplet velocity, we decided to use our camera, capture some blurred images of the droplet and use the blurriness as a guide. The idea was that the blurriness of the droplet corresponded to a certain distance the droplet had covered during a specific time interval. So the shutter speed of the camera was increased to 1 milisecond, and we started taking images of the falling droplets (Figure 2.9). The syringe height varied from 19cm, from the metal base, to 69cm, namely six tests were conducted. A sequence of blurred images was captured for each test. The pictures then were grouped together with respect to the height and analyzed in order to measure the necessary parameters in each one.

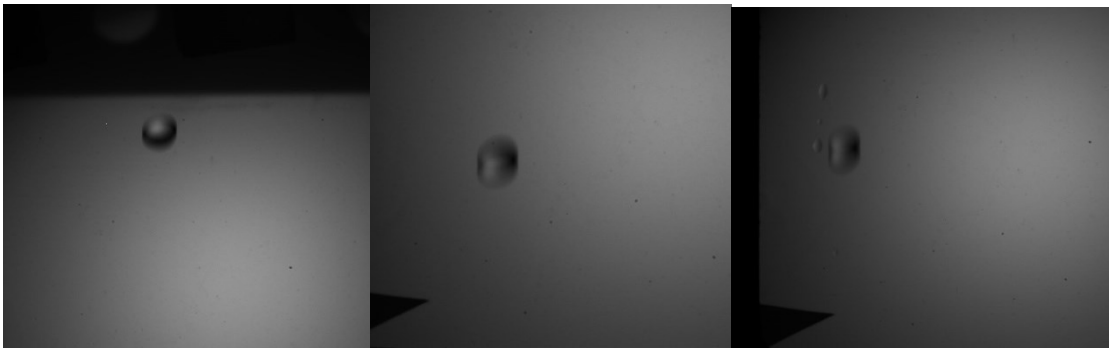

Figure 2.9: Streaked images

In each image the blurred droplet appeared in a form of a vertical ellipse. We measured the distance from the bottom of the blurred droplet to the base and removed it from the total distance between the syringe and the base in order to have the real distance the droplet had gone through by the moment the picture was captured ($h-h_0=h_{real}$). Then we measured the horizontal dimension (semi minor axis) (Dw) and found an average taking as data the measurements from all six tests. This average was used to calculate a theoretical volume if the droplet was sphere. In each image we also measured

the distance of the blurriness (d_{peak}). Considering that the volume of the droplet doesn't change during the fall, the horizontal dimension and the average were used in order to theoretically calculate the other dimension of the ellipse (semi major axis) (D_h) for each image. From the two ellipse dimensions another volume was calculated for each image and was compared each time with the theoretical droplet volume in order to confirm that the volume agreed with the one of the hypothetical sphere (Vratio=1). The distance of the blurriness minus the semi major axis distance of the ellipse was the distance the droplet had covered during the 1 milisecond of the camera's take (D_d). With such a small time interval, it was safe to assume the droplet performs a uniform motion and therefore the droplet velocity was calculated by a simple division between the distance and the time. Some of the described results can be seen indicatively in Table 2.2 below.

Table 2.2: Real Velocity calculation

res	h	h0	hreal	Dw	dpeak	Dh	Vratio	dt	Dw	dD	U	U theory	err
mm/px	m	m	m	px	px	px		sec	mm	mm	m/sec	m/sec	
0,05866	0,200	775	0,154538	92	109	79,93771	1	0,001	5,396738	1,7048	1,7048	1,741276	98%
0,05866	0,200	644	0,162223	92	113	79,93771	1	0,001	5,396738	1,939441	1,939441	1,784044	109%
0,05866	0,200	548	0,167854	89	117	85,41759	1	0,001	5,220758	1,85263	1,85263	1,814745	102%
0,05866	0,200	112	0,19343	84	132	95,88899	1	0,001	4,927457	2,118279	2,118279	1,948101	109%
0,05866	0,200	63	0,196304	85	133	93,64605	1	0,001	4,986117	2,30851	2,30851	1,962522	118%
0,05866	0,300	607	0,264393	88	130	87,36993	1	0,001	5,162097	2,500688	2,500688	2,277586	110%
0,05866	0,300	656	0,261519	88	128	87,36993	1	0,001	5,162097	2,383368	2,383368	2,265171	105%
0,05866	0,300	715	0,258058	86	133	91,4809	1	0,001	5,044777	2,435519	2,435519	2,250133	108%
0,05866	0,400	239	0,38598	91	123	81,70423	1	0,001	5,338078	2,422418	2,422418	2,751896	88%
0,05866	0,400	368	0,378413	90	122	83,52997	1	0,001	5,279418	2,25666	2,25666	2,724787	83%
0,05866	0,500	451	0,473544	88	131	87,36993	1	0,001	5,162097	2,559349	2,559349	3,048104	84%
0,05866	0,500	52	0,49695	84	138	95,88899	1	0,001	4,927457	2,47024	2,47024	3,122523	79%
0,05866	0,600	410	0,575949	86	140	91,4809	1	0,001	5,044777	2,84614	2,84614	3,361566	85%
0,05866	0,600	446	0,573838	88	141	87,36993	1	0,001	5,162097	3,14595	3,14595	3,355398	94%
0,05866	0,700	374	0,678061	87	139	89,38998	1	0,001	5,103437	2,910134	2,910134	3,647404	80%
0,05866	0,700	104	0,693899	87	144	89,38998	1	0,001	5,103437	3,203435	3,203435	3,689757	87%
0,05866	0,700	677	0,660287	85	139	93,64605	1	0,001	4,986117	2,660471	2,660471	3,599282	74%

The whole process was repeated one more time because some measurements had sufficient deviation from the theoretical velocities. The two tests were combined in an excel file and a diagram was designed which can be seen in Figure 2.10. The blue line sums up the results of the first test and the red one sums up the results of the second test. The two tests combined gave the black line in the middle which we considered the most valid in order to extract a function to describe the velocity in relation to the distance.

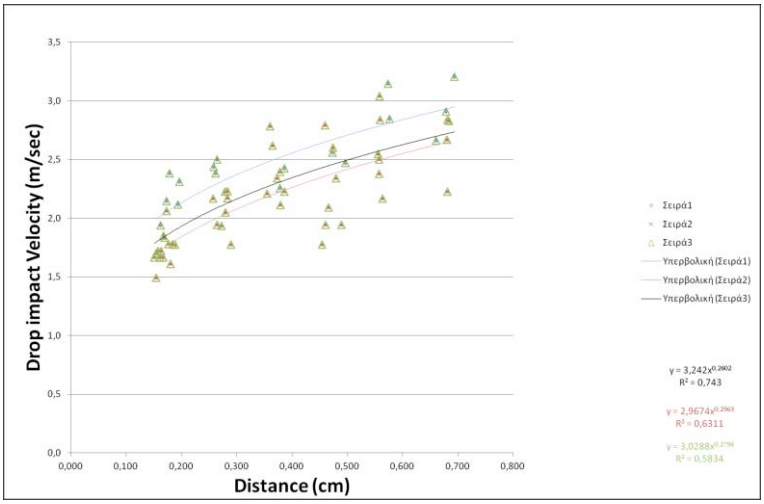

Figure 2.10: Velocity chart in relation to the vertical distance between the syringe and the base

A similar process was followed to calculate the droplet We numbers. With the velocities now known for any given distance, the We numbers were easy to calculate. Considering a value of the water surface tension shown in the following table, We numbers were calculated using the already described formula and the values were designed in a diagram shown in Figure 2.11.

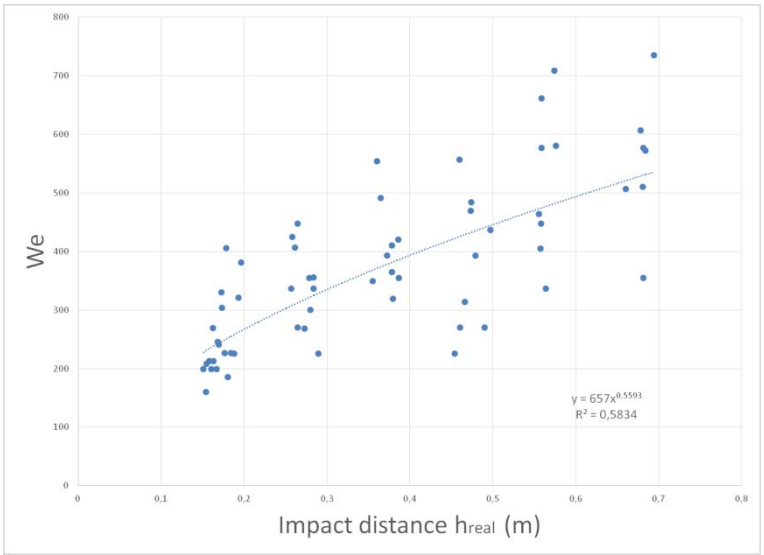

Figure 2.11: We chart in relation to the vertical distance between the syringe and the base

From the fitting which can be seen in Figure 2.11 we used the given function in order to calculate the six We numbers of the droplets that corresponded to each of the experiments that were carried out. The results can be seen in Table 2.3.

Table 2.3: Droplet velocities and We numbers for the 6 distances

h(m)	V_d(m/s)	We	σ(Nm)	ρ(Kg/m³)

0,190	2,10	260	0,072	1000
0,290	2,35	329		
0,390	2,54	388		
0,490	2,69	441		
0,590	2,83	489		
0,690	2,94	534		

2.3 Image Process

As already described above, we conducted one experiment for each of the three piles in three different angles and six different distances between the syringe and the target. In the end, there were 54 experiments with many pictures in each one. For the image processing we used the imageJ program. For each image batch there was a photograph of the screen's background with a ruler placed along the metal base in order to give us the scale of the measurements. In Figure 2.12 for example it can be seen that 20mm of the ruler correspond to a certain amount of pixels.

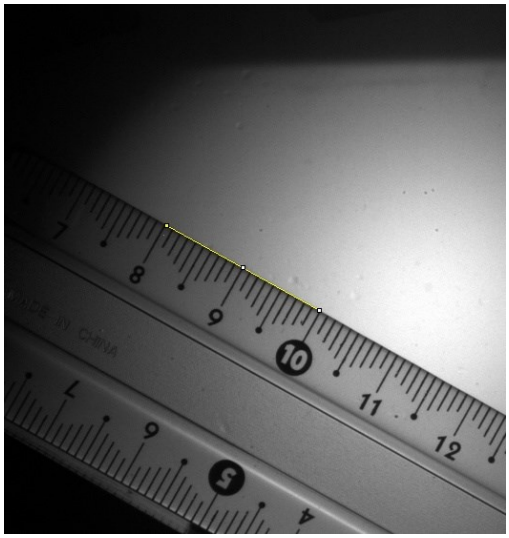

Figure 2.12: Image scale

With the scale now known, for all the batches, we could measure the parameters of the crown where there was splashing. The parameters we chose to measure were the crown height on both sides of the crown, as well as the angle between the crown and the surface again on both sides (Figure 2.13). Because there was no way we knew the precise time in the evolution of the crown we decided to base our results on the crown diameter D_1. That means, the larger the D_1, the more the phenomenon has progressed.

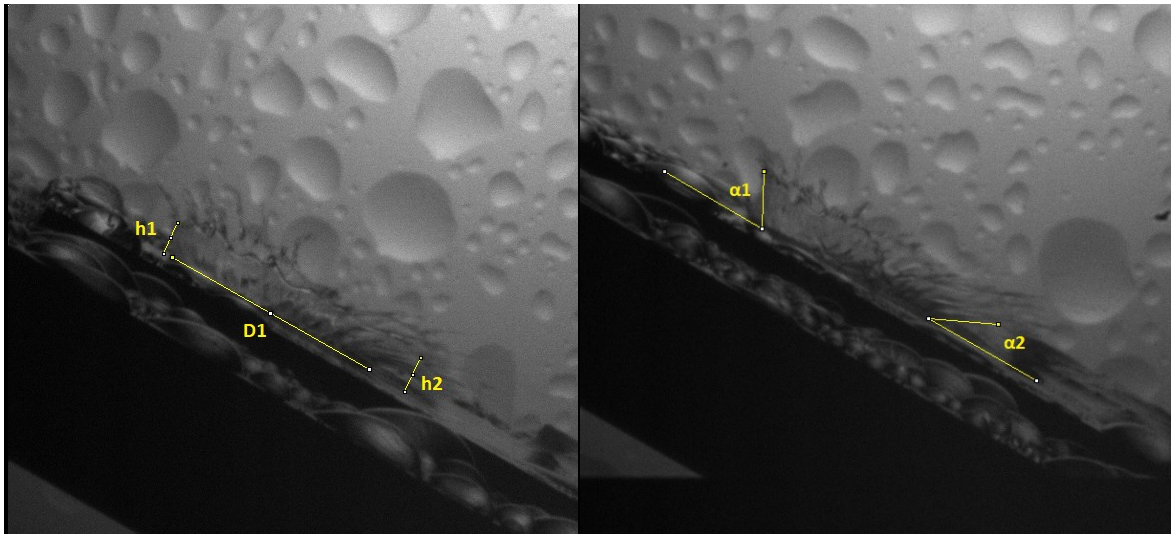

Figure 2.13: Measurements in ImageJ.

With all the measurements completed and concentrated in excel files, we formed diagrams in order to visualize the results. The crown diameter D_1 was non-dimensionalised using the droplet diameter D_0 and was used as the x axis in order to see how the four parameters change during the evolution of the phenomenon. Two types of diagrams were designed. The first type included diagrams of the four parameters for the 6 different We numbers, while the second type were diagrams of the four parameters for the 3 different roughness.

The experimental data gathered in this thesis, is not numerically accurate, it merely shows the tendency of each parameter while the phenomenon evolves. This happened because of the conditions of the experiment. The frequency of the falling droplets did change from experiment to experiment due to the lack of accuracy of the valve that fed water to the syringe. Different frequencies meant that there was a different amount of water stagnating on the tile each time. When the droplets fell with lower frequency, there was enough time for the water to flow until the next impingement and therefore the collision took place in a thin liquid film. When the droplets fell with higher frequency, the water accumulated, increasing the film thickness where the next droplet landed. Furthermore, sometimes a droplet collision would form a bulk of water either upslope or downlsope. If the next collision formed a crown, some of its parameters were affected from the position of the water bulk and took values that don't match with the majority of the tests. Unfortunately, there was not enough time to conduct more tests in order to determine a relation between the frequency of the falling droplets and the changes in the crown parameters.

What we mean with all the above, is that the final data should not be considered as an accurate numerical analysis of the crown parameters, but an indicative investigation of the phenomenon's evolution. The diagrams can be seen in the next sections.

3. Results and Discussion

3.1 Morphologic investigation

In order to see the phenomenon of the collision and understand what happens in the phases of its progress, first we need to observe the images taken from the lab. In this section we present indicatively some pictures from each test, in order to comprehend the formation and evolution of the splashing. The images are shown in the same sequence the tests were conducted which means that they are grouped based on the three angles of the base with respect to the horizontal axis. Each row depicts the evolution of the phenomenon for a given distance between droplet and target and therefore a given droplet We number. We chose to use two of the distances (29cm and 59cm) along with the 19cm distance were the phenomenon was not clear splashing in all the angles.

The progress of the phenomenon can be seen for the three We numbers for the tile with the lowest roughness (Ra=0.06μm), placed at θ=10°. It is evident that in the first case (We=260, Figure 3.1) the collision leads to half a crown with short fingers on the rim that survive throughout the final stages where the crown height is diminished. As the We number increases (We=329, Figure 3.2 and We=534, Figure 3.3), the splashing becomes clearer, the crown height becomes larger as do the fingers which they finally break to satellite droplets during the last stages. The stages are in order: droplet collision, crown formation, development of crown height and fingers and finally collapsing of the crown and formation of satellite droplets from the fingers.

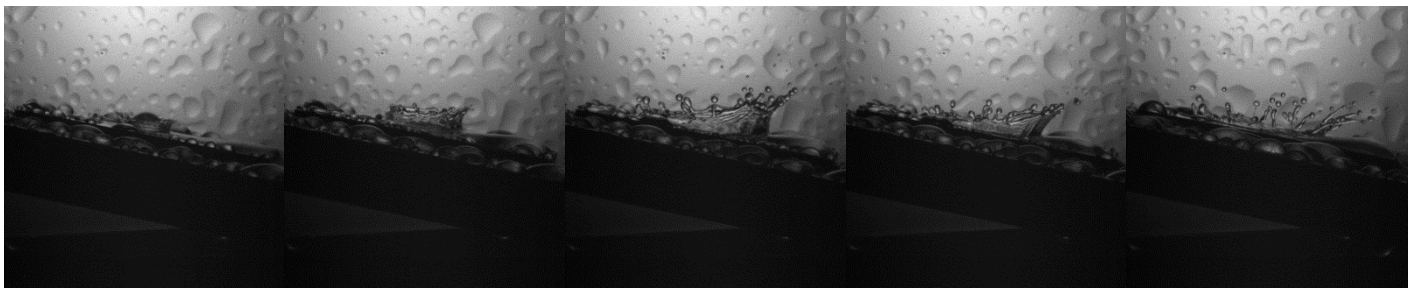

Figure 3.1: Evolution of droplet impingement for θ=10°, We=260, Ra=0.06μm

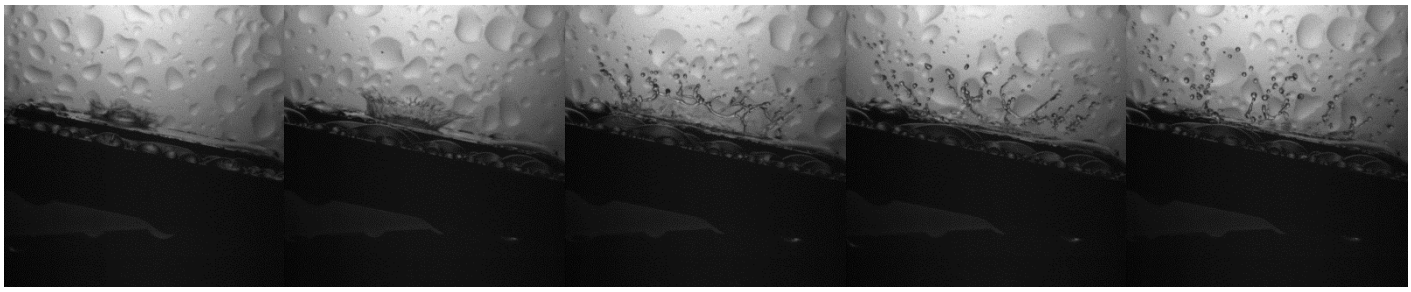

Figure 3.2: Evolution of droplet impingement for θ=10°, We=329, Ra=0.06μm

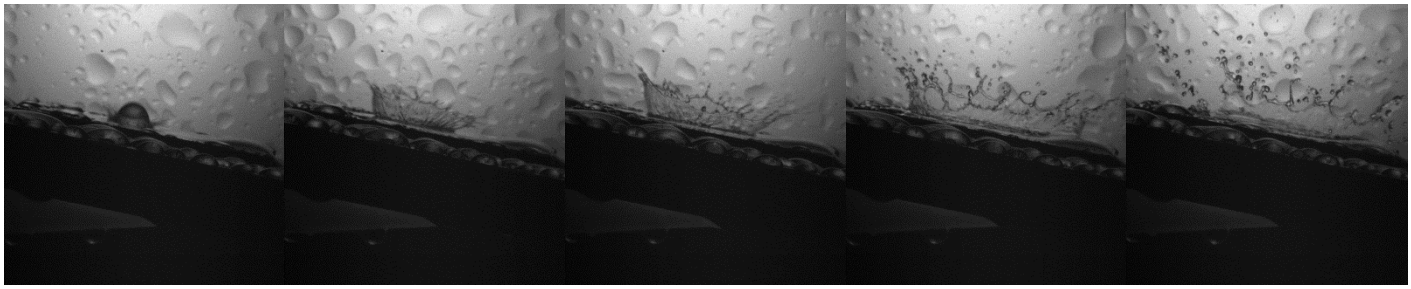

Figure 3.3: Evolution of droplet impingement for θ=10°, We=534, Ra=0.06μm

When the surface roughness increases to Ra=1.37μm it is evident that in the first case (We=260, Figure 3.4), the crown is not formed uniformly. The fingers created are short and few but quite large in diameter. As the droplet We increases (We=329, Figure 3.5 and We=534, Figure 3.6), the crown becomes more uniform, the height increases as does the number of fingers. As the crown collapses, the fingers break to form satellite droplets. The same phases of the phenomenon can be seen in these rows of images, this time the crown being higher during its fully developed stages.

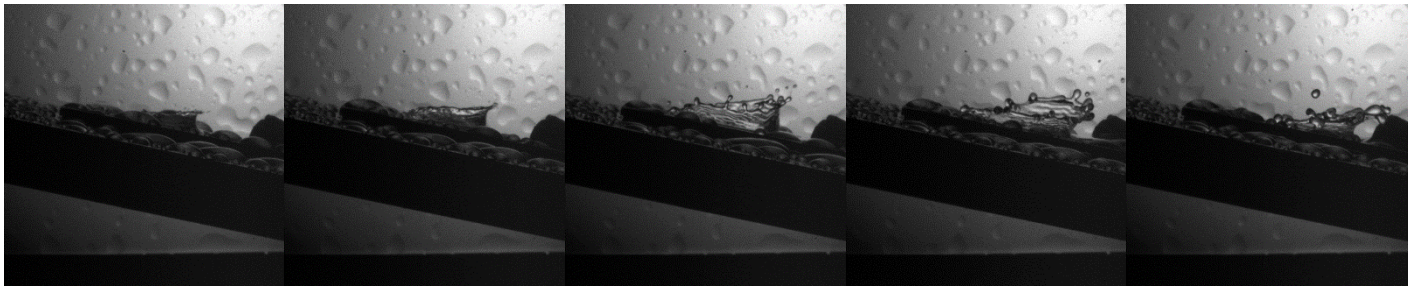

Figure 3.4: Evolution of droplet impingement for θ=10°, We=260, Ra=1.37μm

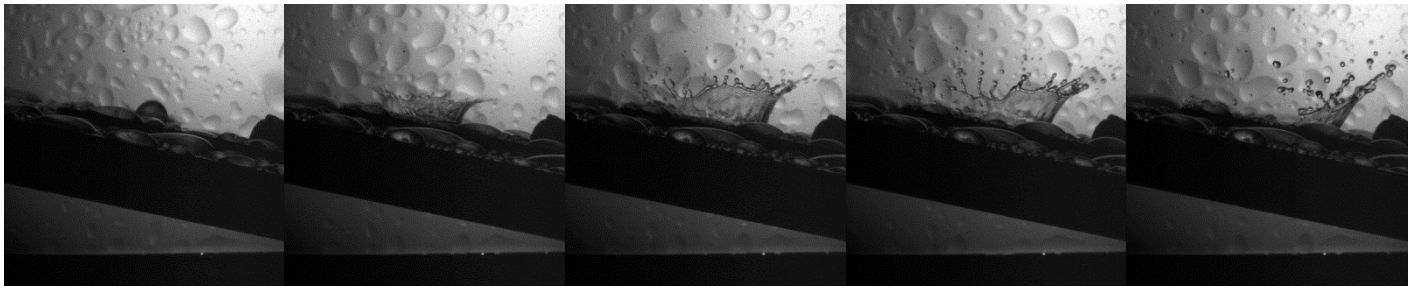

Figure 3.5: Evolution of droplet impingement for θ=10°, We=329, Ra=1.37μm

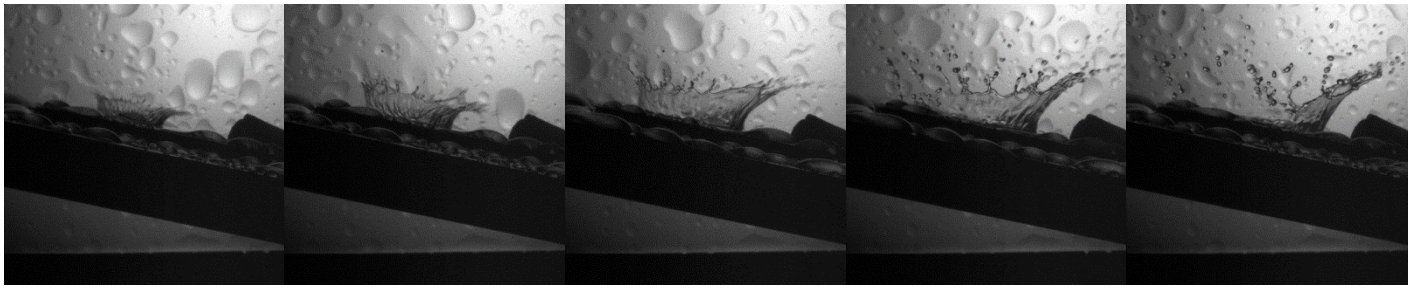

Figure 3.6: Evolution of droplet impingement for θ=10°, We=534, Ra=1.37μm

Comparing the three different surfaces, in all the cases, there is a slight increase in the crown height with the increase in roughness, but all three surfaces seem to respond in a similar morphological way for each of the three distances. The stages of the evolution for the tile with the highest roughness remain the same as before.

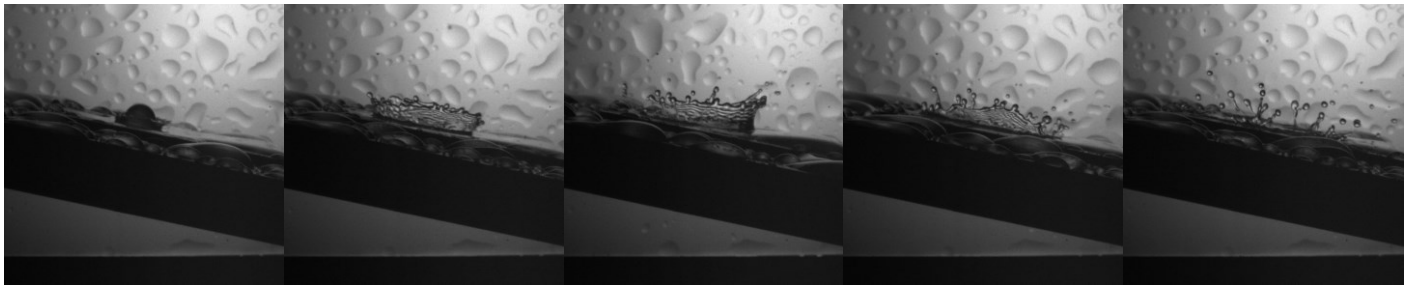

Figure 3.7: Evolution of droplet impingement for θ=10°, We=260, Ra=6.99μm

Figure 3.8: Evolution of droplet impingement for θ=10°, We=329, Ra=6.99μm

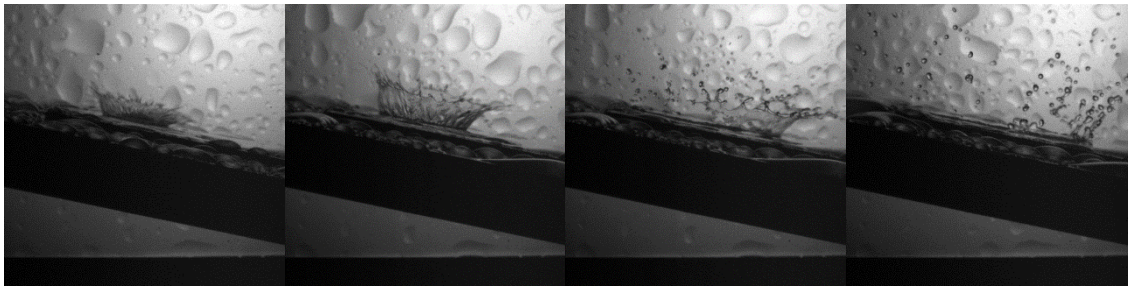

Figure 3.9: Evolution of droplet impingement for θ=10°, We=534, Ra=6.99μm

When the surface is placed at θ=20° in relation to the horizontal axis, the splashing phenomenon is much less intense in the case for We=260 (Figure 3.10) compared to the case of θ=10°. The crown is approximately half and its height is very low compared to the higher We numbers. Some fingers may be formed on the downslope side which will form some satellite droplets when the crown collapses. Again, the difference in the crown height between the two next cases is clear (We=329, Figure 3.11

and We=534, Figure 3.12), as is the height of the fingers, measured from the rim. Se, the higher the droplet We, the higher the formed crown, and the fingers and the more satellite droplets at the end.

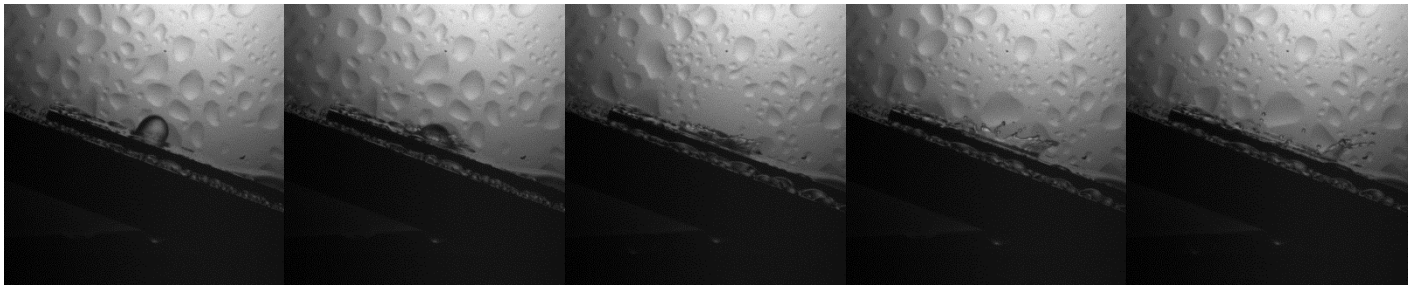

Figure 3.10: Evolution of droplet impingement for θ=20°, We=260, Ra=0.06μm

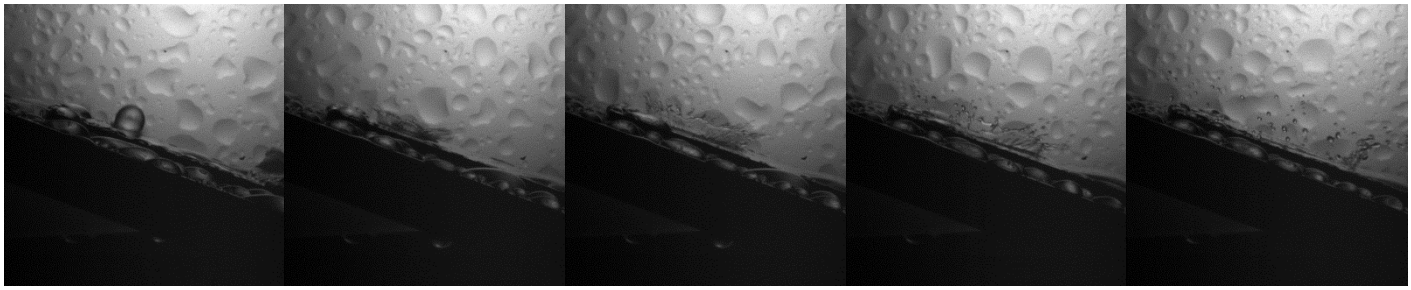

Figure 3.11: Evolution of droplet impingement for θ=20°, We=329, Ra=0.06μm

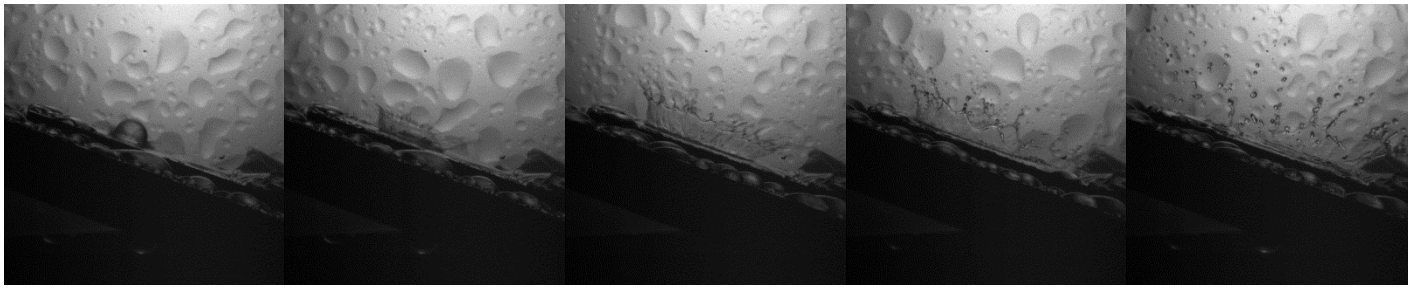

Figure 3.12: Evolution of droplet impingement for θ=20°, We=534, Ra=0.06μm

For the second tile (Ra=1.37μm), in the case of We=260 (Figure 3.13) we can observe a more integrated crown compared to the first one (Ra=0.06μm), although it is not a full circle. The crown is also higher than the one at θ=10**°**, possibly due to the increased roughness. The biggest crowns in diameter occur for the higher We while their height doesn't seem to be affected (Figure 3.14 and Figure 3.15).

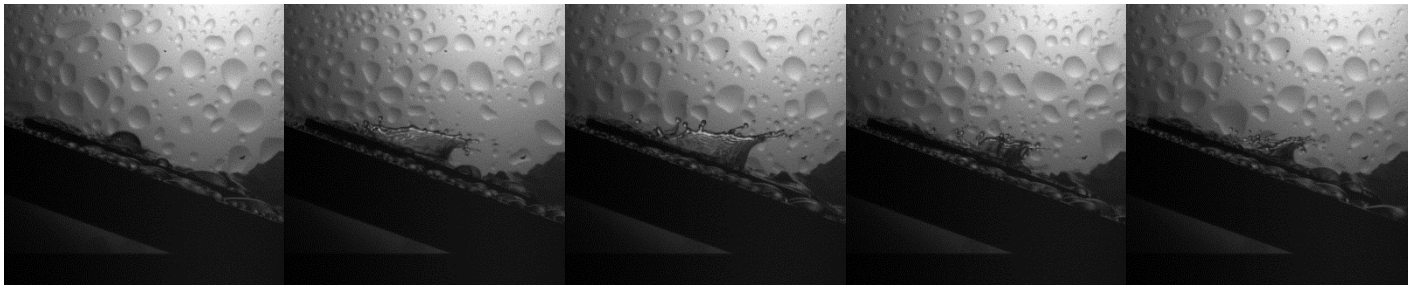

Figure 3.13: Evolution of droplet impingement for θ=20°, We=260, Ra=1.37μm

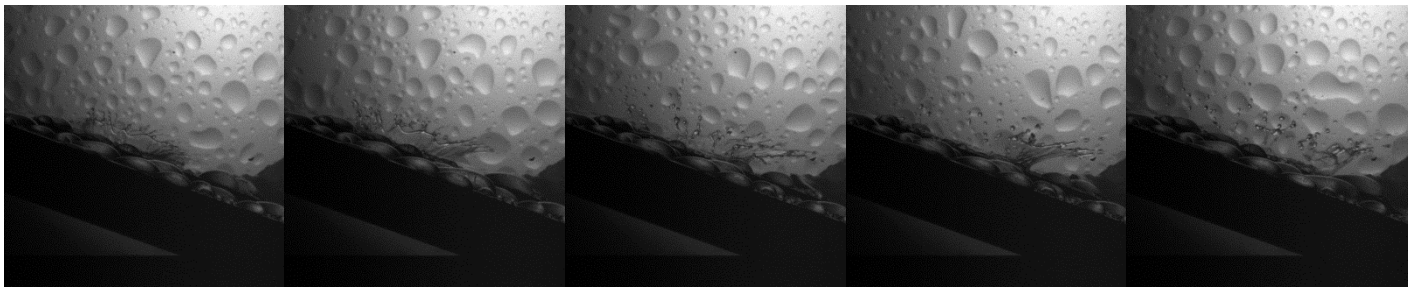

Figure 3.14: Evolution of droplet impingement for θ=20°, We=329, Ra=1.37μm

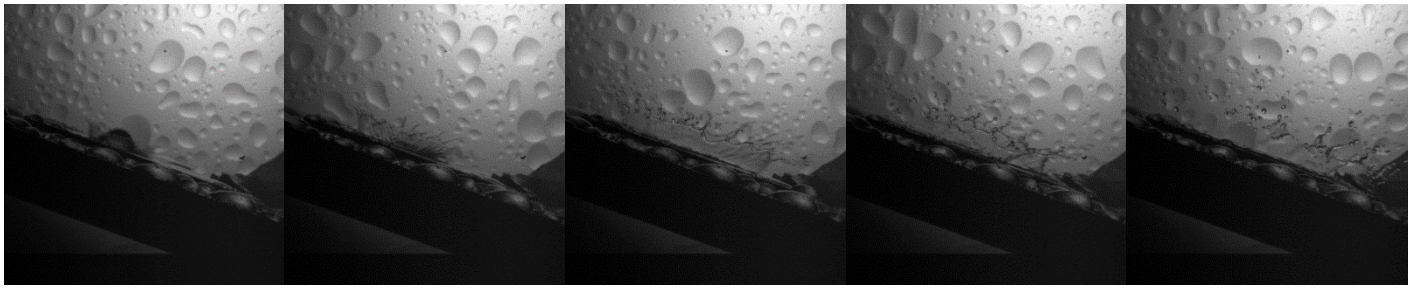

Figure 3.15: Evolution of droplet impingement for θ=20°, We=534, Ra=1.37μm

Here we see the tile with the highest roughness (Ra= 6.99μm) in each test. The crowns that are formed in the case of We=260 (Figure 3.16) are here uniform which can be attributed to the higher value of roughness that causes more water to stagnate on the surface. The fingers are small and few and there are not many satellite droplets at the end. The next two figures (We=329, Figure 3.17 and We=534, Figure 3.18) show that the crown height increases with the We number as well as the number of fingers which form the satellite droplets when the crown collapses.

In all the cases shown above the same evolution phases can be distinguished: formation of the crown, development of the height and fingers and collapsing of the crown with the formation of satellite droplets from the fingers.

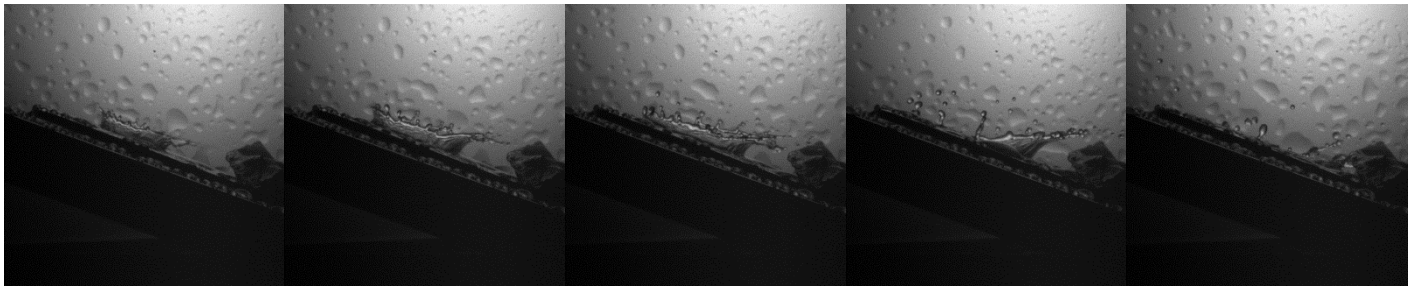

Figure 3.16: Evolution of droplet impingement for θ=20°, We=260, Ra=6.99μm

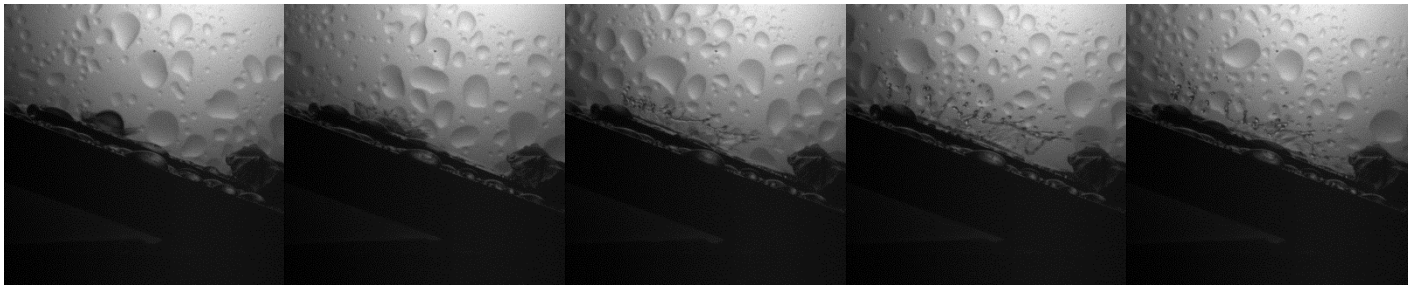

Figure 3.17: Evolution of droplet impingement for θ=20°, We=329, Ra=6.99μm

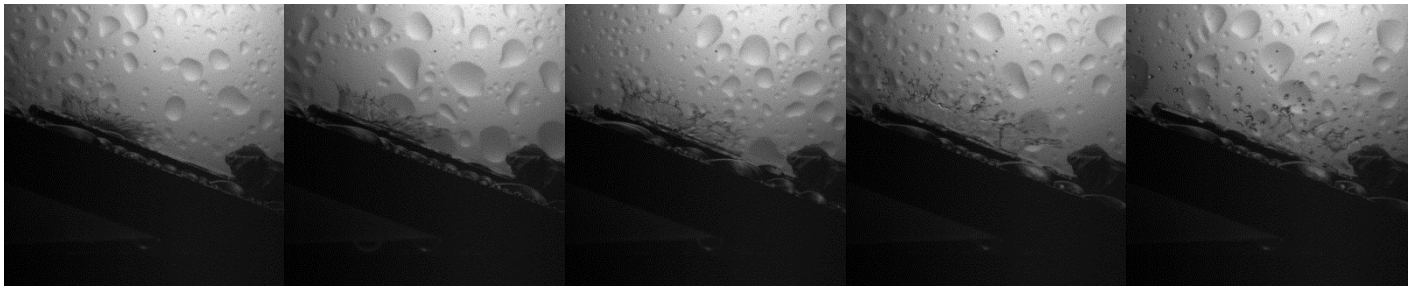

Figure 3.18: Evolution of droplet impingement for θ=20°, We=534, Ra=6.99μm

As we can see in Figure 3.19 for We=260, the effect of the big angle (θ=30°) on the splashing is quite important. The collision does not form a crown, it merely pushes the water film downhill creating a mass of water that resembles to half a crown. It can be said that this is not a case of splashing, but a transitional phenomenon between deposition and splashing. The next two figures (We=329, Figure 3.20 and We=534, Figure 3.21) showcase the development of the splashing for a low We number, were even though the crown is formed its height is almost negligible, as well as for a higher We where the formation and development of the crown is more clear and its behavior throughout the evolution resembles the previous occasions of θ=20°.

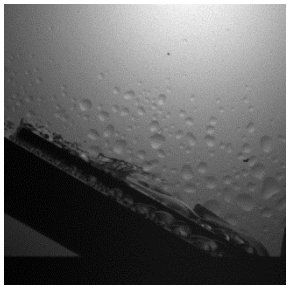

Figure 3.19: Evolution of droplet impingement for θ=30°, We=260, Ra=0.06μm

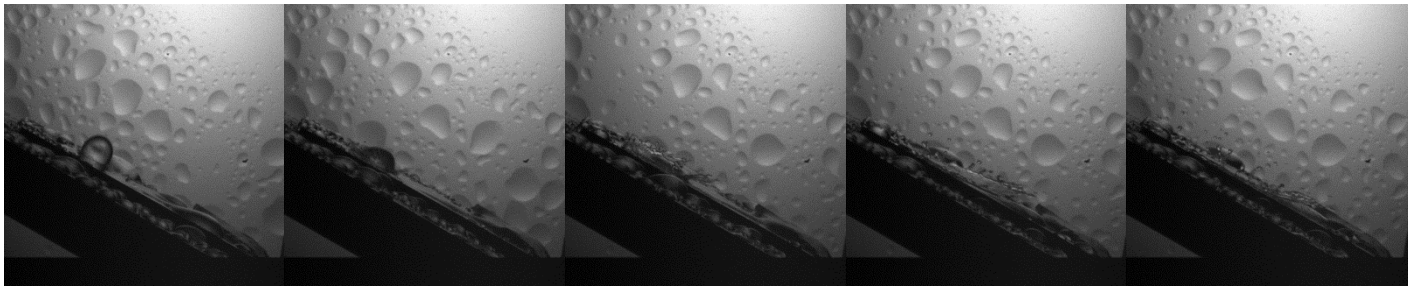

Figure 3.20: Evolution of droplet impingement for θ=30°, We=329, Ra=0.06μm

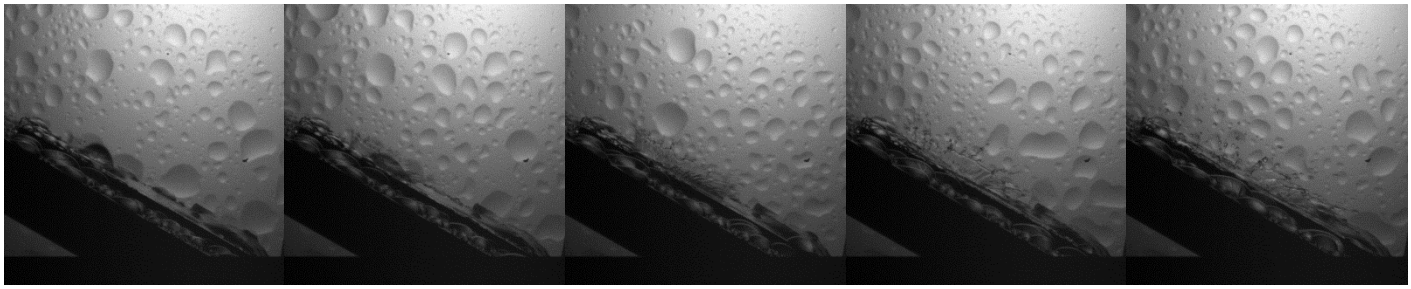

Figure 3.21: Evolution of droplet impingement for θ=30°, We=534, Ra=0.06μm

For this tile (Ra=1.37μm), again it can be seen that in the case with the lowest We number (Figure 3.22), the occurring phenomenon is a transitional one, between deposition and splashing. The falling droplet pushes the water film creating what may be considered a form of a crown. Again, for the low We number the crown height is very small, but it does evolve following the aforementioned phases. For the higher We (Figure 3.23 and Figure 3.24) the splashing phenomenon occurs normally, a crown with a measurable height is formed, with many fingers that gradually grow and finally form the satellite droplets while the crown collapses.

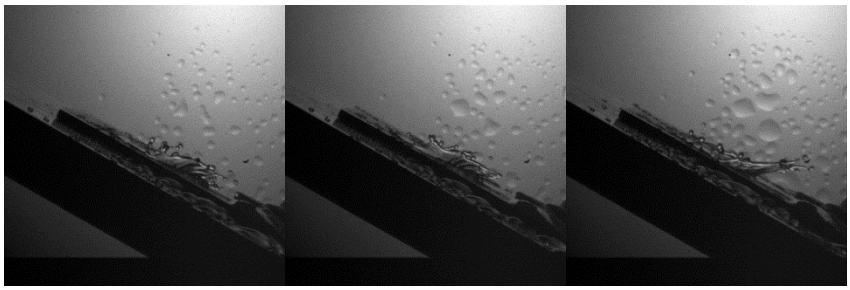

Figure 3.22: Evolution of droplet impingement for θ=30°, We=260, Ra=1.37μm

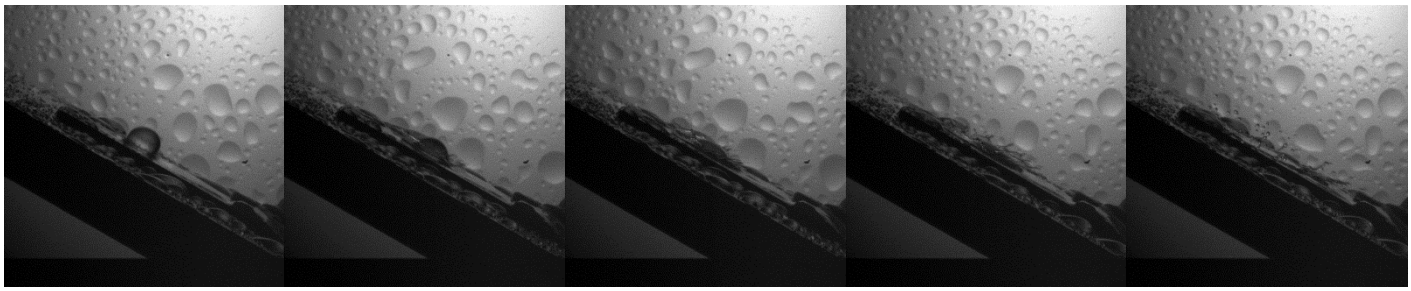

Figure 3.23: Evolution of droplet impingement for θ=30°, We=329, Ra=1.37μm

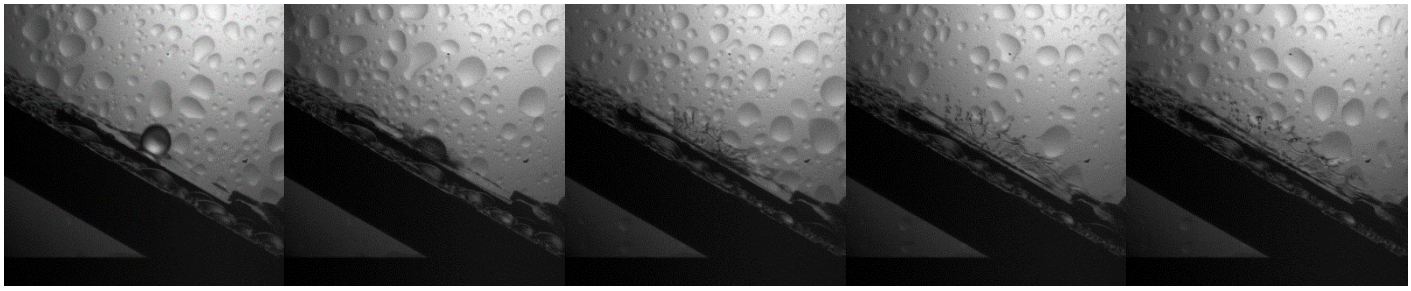

Figure 3.24: Evolution of droplet impingement for θ=30°, We=534, Ra=1.37μm

In the final three rows (We=260, Figure 3.25, We=329, Figure 3.26 and We=534, Figure 3.27) the effect of the angle is confirmed. No clear splashing phenomenon can be observed for the lowest We, rather

the same transitional phenomenon that occurred for the previous two surfaces. The higher the We number, the higher the formed crowns. The evolution of the fingers resembles the previous cases.

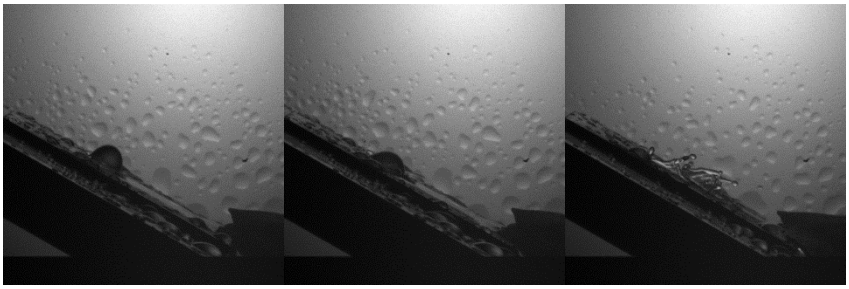

Figure 3.25: Evolution of droplet impingement for θ=30°, We=260, Ra=6.99μm

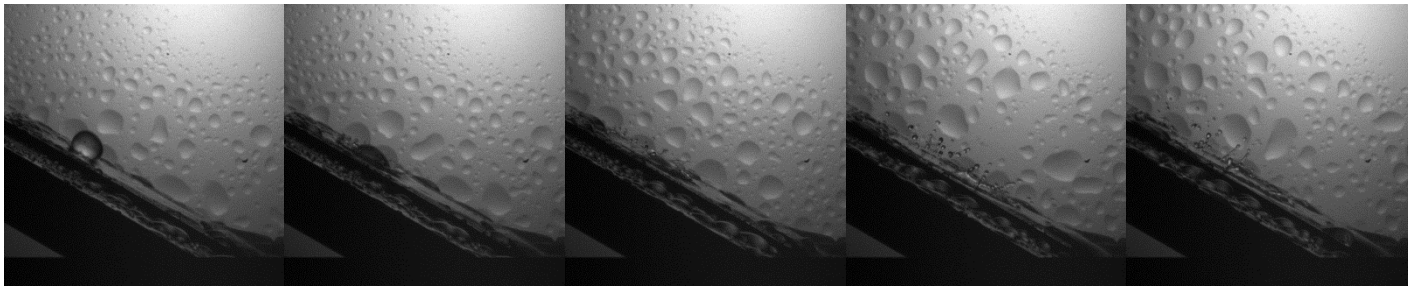

Figure 3.26: Evolution of droplet impingement for θ=30°, We=329, Ra=6.99μm

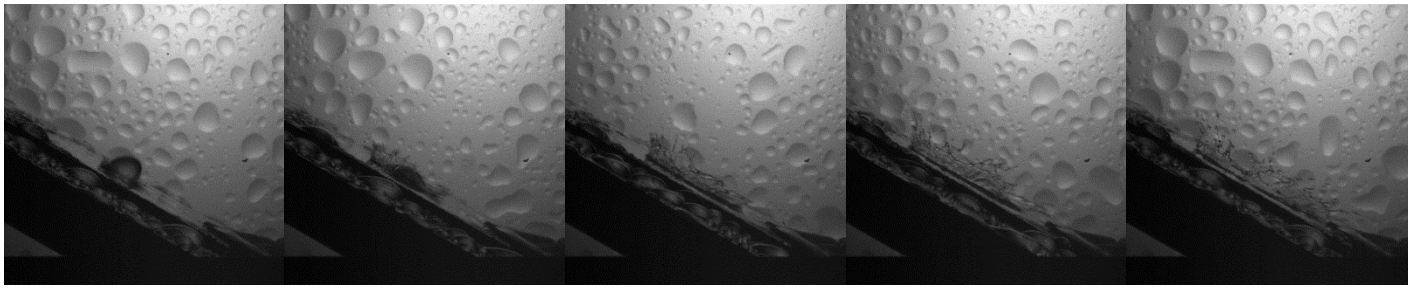

Figure 3.27: Evolution of droplet impingement for θ=30°, We=534, Ra=6.99μm

3.2 Weber Number effect on droplet impingement

In this section the presented diagrams are grouped with respect to each tile in the same angle. The four parameters we studied can be seen for each tile for θ=10°, then for θ=20° and finally for θ=30°.

Figure 3.28 shows that the crown height on both sides ranges between 0,5 and $1.5D_0$ and that the general trend for h_1 and h_2 is to increase while the phenomenon progresses. In both diagrams the lowest values are observed for the lowest We numbers while the highest values for the highest We numbers. The crown angle on the upslope side seems to be larger than the angle on the downslope side and has the trend to decrease or remain the same during the progress, while the angle on the downslope side tends to do the opposite (Figure 3.29). No escalation can be seen in relation to the increasing We numbers.

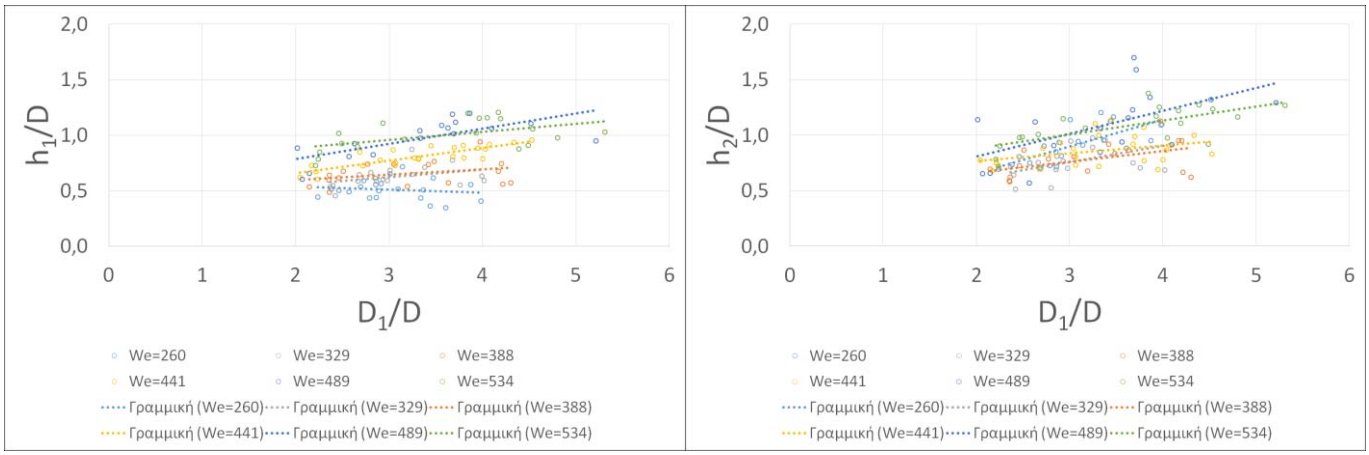

Figure 3.28: Crown height on the upslope (left) and downslope (right) side for θ=10°, Ra=0.09μm

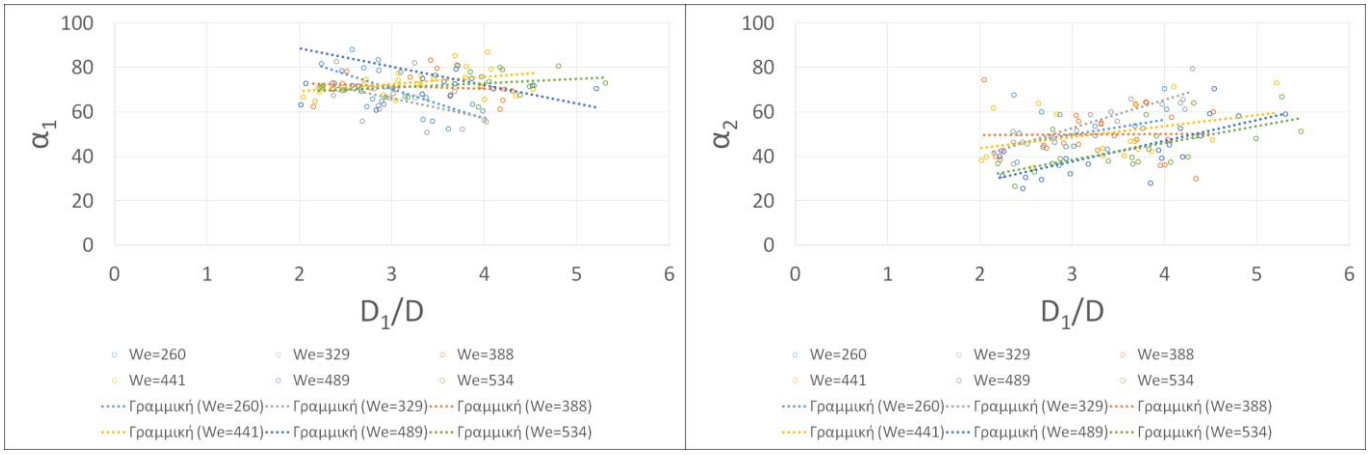

Figure 3.29: Crown angle on the upslope (left) and downslope (right) side for θ=10°, Ra=0.09μm

Figure 3.30 shows that the crown heights on both sides of the crown have values between 0.5 and $1D_0$ and have the trend neither to increase or decrease with the phenomenon progress. The angles of the crowns (Figure 3.31) in this case don't present any clear trend during the evolution of the phenomenon, but again the angle on the upslope side (α_1) is constantly larger than the angle on the downslope side (α_2). The α_2 angle has the higher values for the lowest droplet We numbers while the lowest values appear for the higher We numbers. The increase of the α_2 can be attributed to the final stages, before the collapse of the crown.

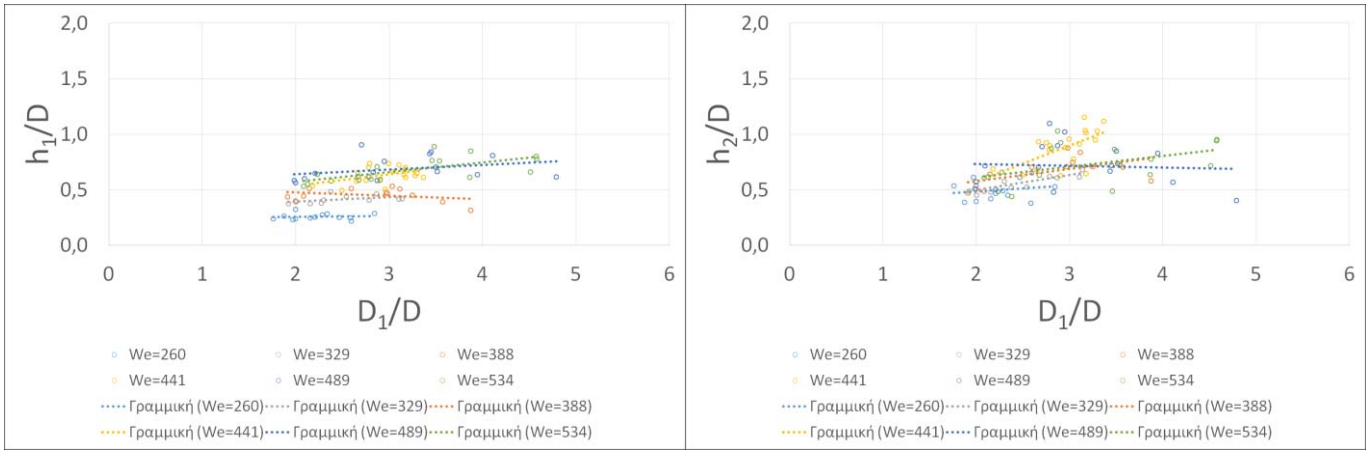

Figure 3.30: Crown height on the upslope (left) and downslope (right) side for θ=20°, Ra=0.09μm

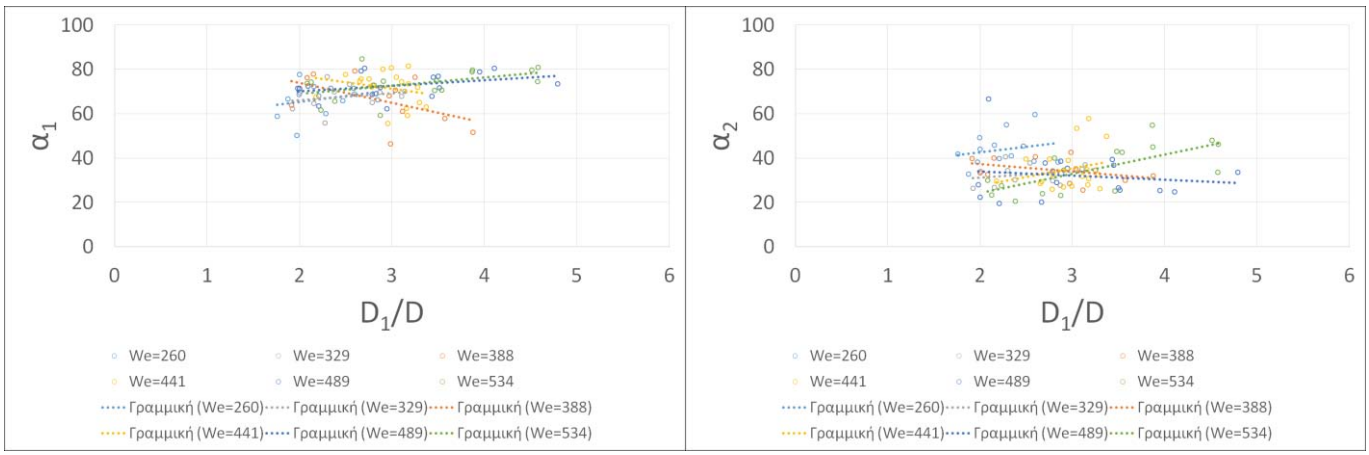

Figure 3.31: Crown angle on the upslope (left) and downslope (right) side for θ=20°, Ra=0.09μm

Figure 3.32 and Figure 3.33 show the same parameters of the first tile but this time placed at θ=30°. H_1 and h_2 seem to have the trend to increase during the phenomenon, and the crown height on the upslope side (h_1) takes noticeably lower values than h_2 which is due to the larger angle. The highest values on both parameters can be seen for the highest We number. The angle on the upslope side is larger than the one on the downslope side, and there is no clear trend for any of them. The measurements were fewer in this case, because as seen in the morphologic investigation, when the tile was under 30° in relation to the x-axis, no clear crown was shaped because the collision outcome was a transitional state between splashing and deposition.

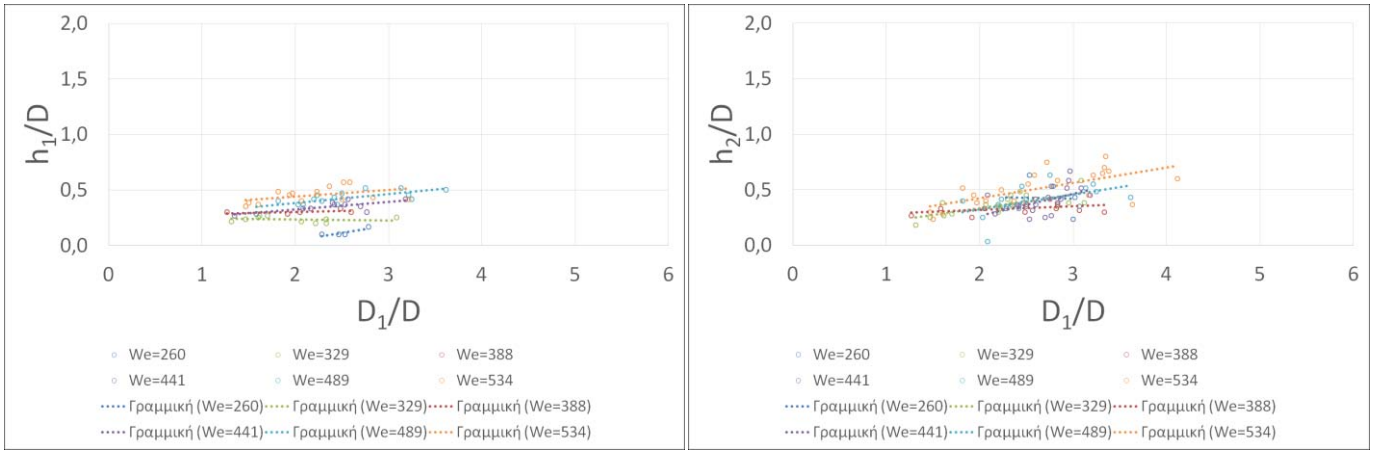

Figure 3.32: Crown height on the upslope (left) and downslope (right) side for θ=30°, Ra=0.09μm

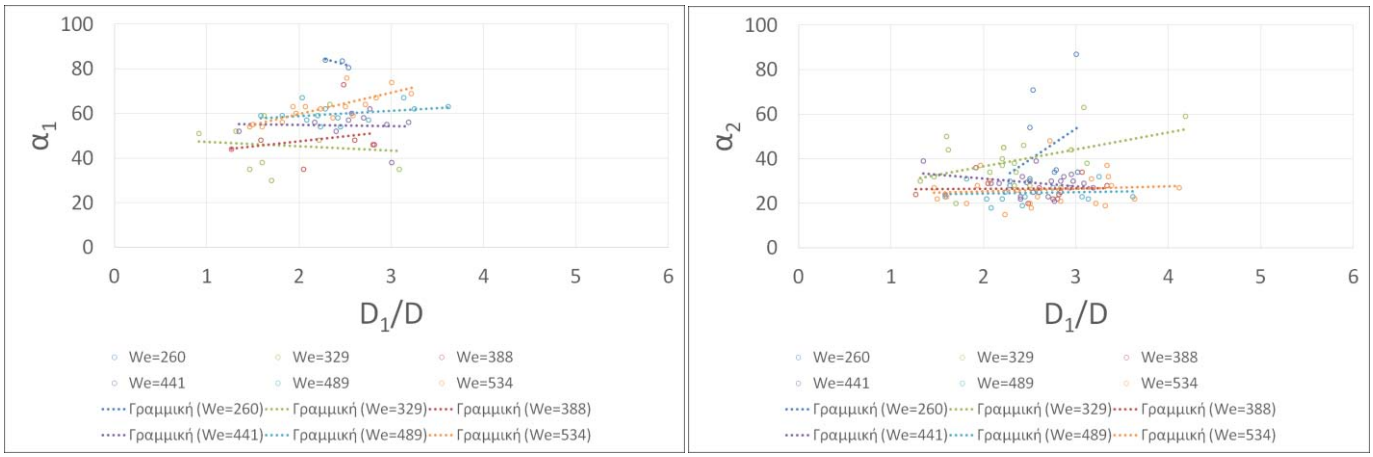

Figure 3.33: Crown angle on the upslope (left) and downslope (right) side for θ=30°, Ra=0.09μm

As expected the highest crowns were formed in the first case of θ=10° provided that both h_1 and h_2 parameters progressively decrease as the angle of the tile increases, independently of the We number. The same can be said for the α_2, but it is not as clear for the α_1 parameter. Although it is not definitive, the highest values for both crown heights are encountered for the highest We.

Figure 3.34 shows the crown's heights on the next tile for θ=10°. The h_1 parameter is significantly lower than the h_2 (values between 0.2 and $1.2D_0$ for the first against values between 0.5 and $1.8D_0$ for the second one). While the h_1 remains roughly the same throughout the phenomenon's exelixis, the h_2 has the trend to increase rapidly during the development of the crown. The angle on the upslope side (α_1) in this case seems to range from 40° to 80° and it is not significantly larger than the angle on the downslope side (α_2) (Figure 3.35). The latter has a greater dispersion and has no clear trend which may be due to bulks of water that remained from the previous colision, but it can be said with certainty that the lowest values correspond to the highest We numbers.

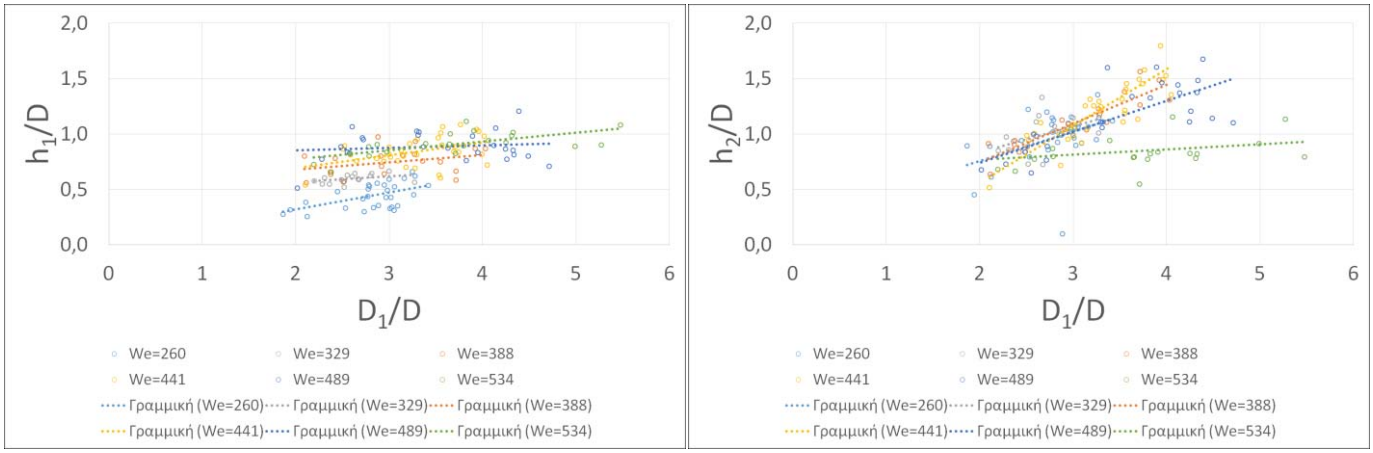

Figure 3.34: Crown height on the upslope (left) and downslope (right) side for θ=10°, Ra=1.37μm

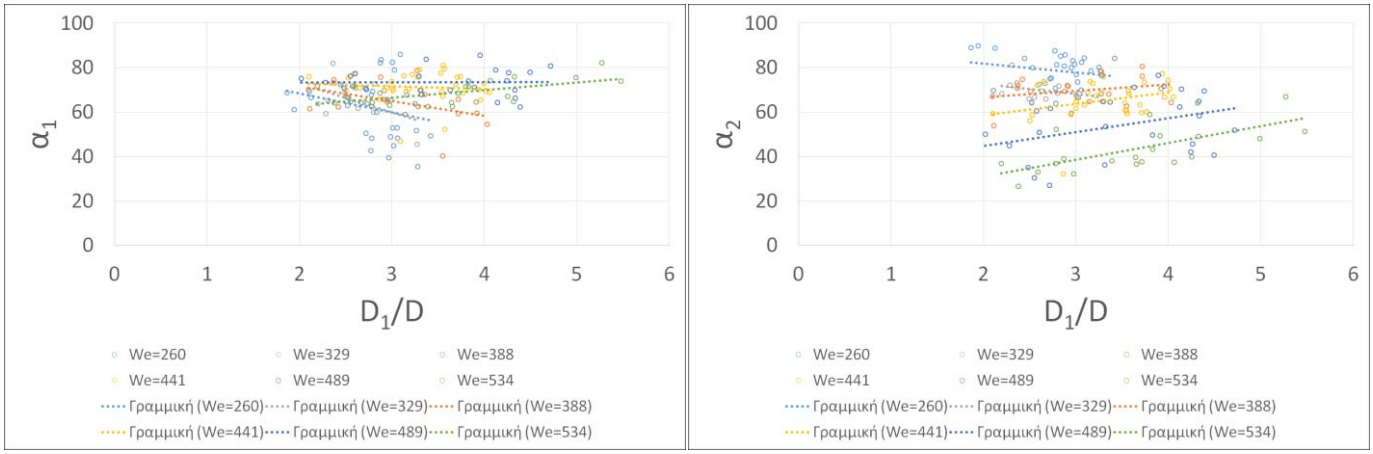

Figure 3.35: Crown angle on the upslope (left) and downslope (right) side for θ=10°, Ra=1.37μm

In the case of θ=20° it can be deduced that the h_1 parameters takes lower values than the h_2 (Figure 3.36). The first parameter remains within the same range of values throughout the phenomenon while the second clearly increases. No specific relation with the We number of the droplet can be extracted. The angle on the upslope side α_1 takes significantly higher values than the angle on the downslope side α_2, and has the trend to remain the same or slightly decrease during the evolution of the phenomenon,

while the angle on the downlsople side tends to increase during the same time. The higher values of the α_1 match the higher We numbers while the opposite seems to happen with the α_2 (Figure 3.37).

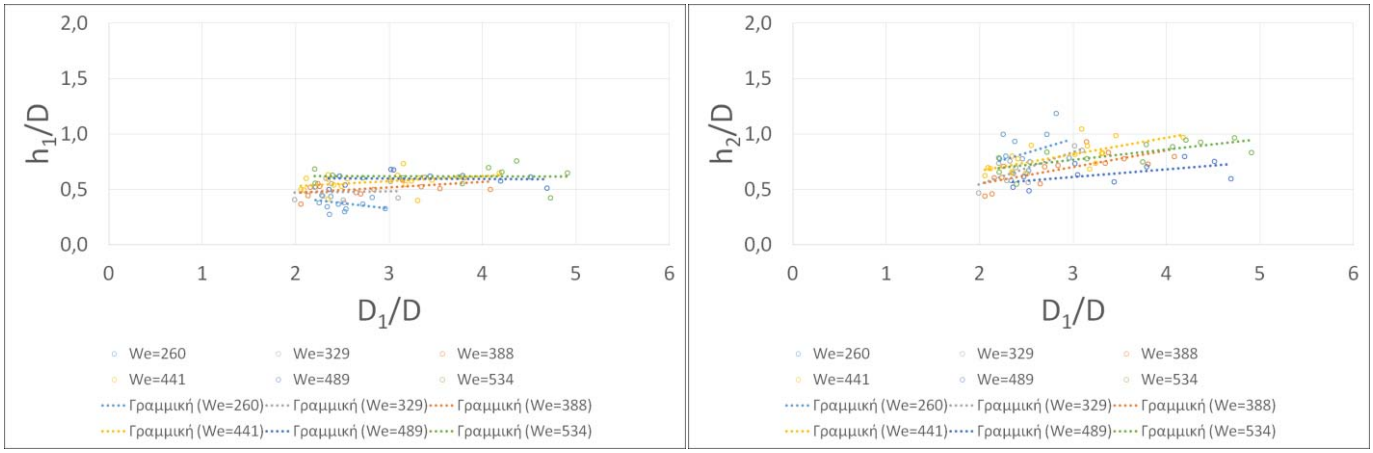

Figure 3.36: Crown height on the upslope (left) and downslope (right) side for θ=20°, Ra=1.37μm

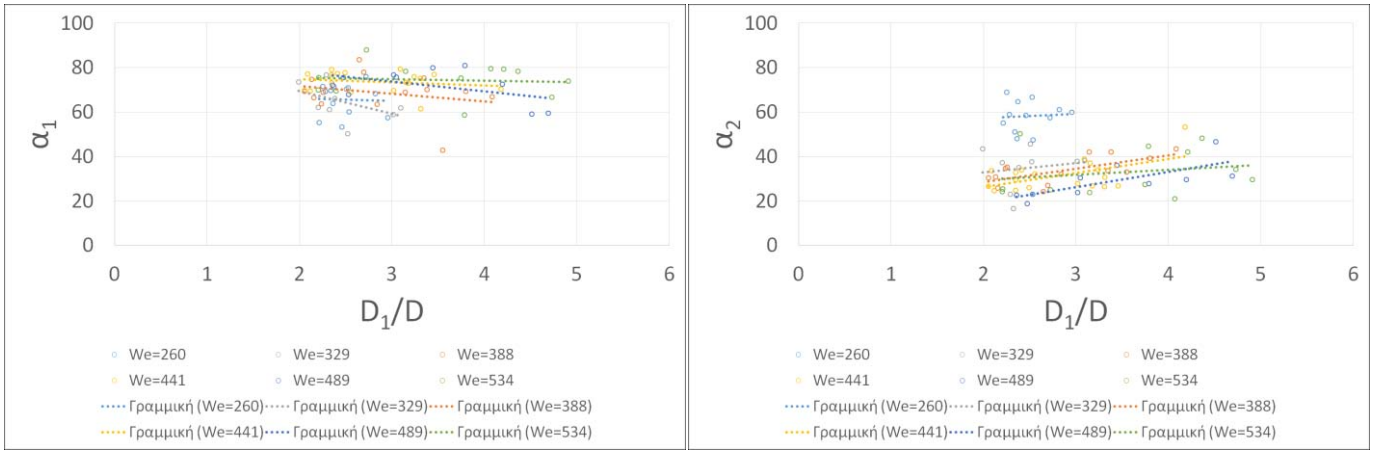

Figure 3.37: Crown angle on the upslope (left) and downslope (right) side for θ=20°, Ra=1.37μm

For the 30° angle, the crown heights on both sides take the same low values, independently of the We number, and they both have a slight trend to increase throughout the phenomenon (Figure 3.38). The α_1 angle has higher values than the α_2, but they both have the trend to increase during the evolution (Figure 3.39).

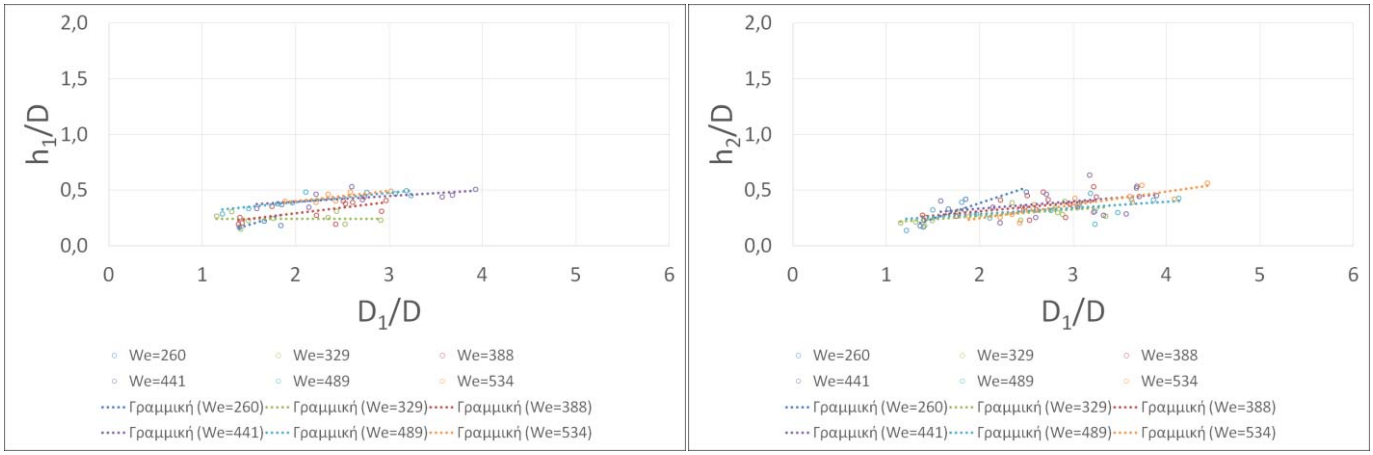

Figure 3.38: Crown height on the upslope (left) and downslope (right) side for θ=30°, Ra=1.37μm

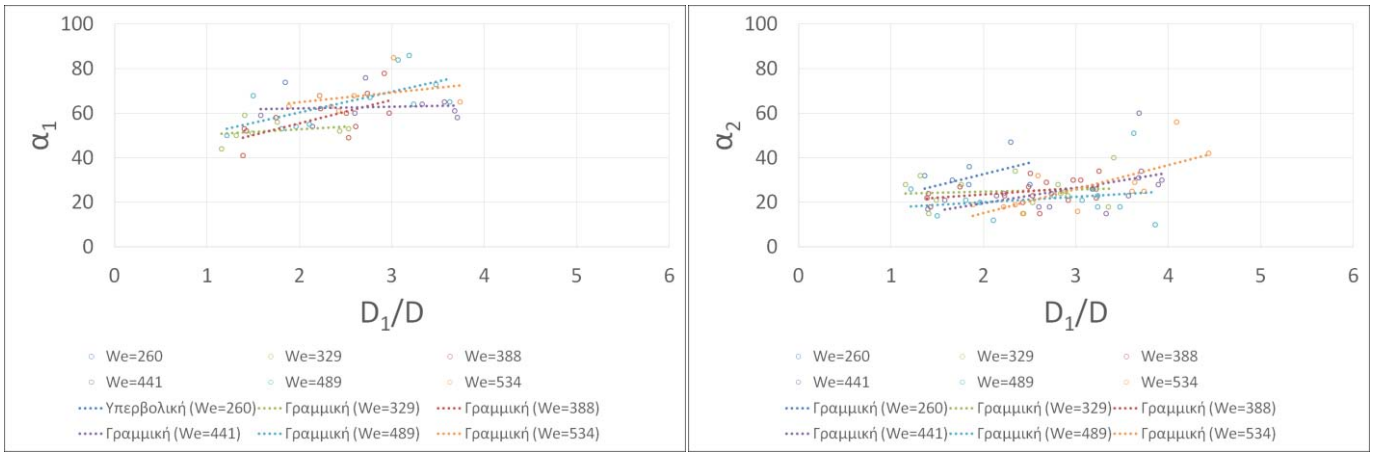

Figure 3.39: Crown angle on the upslope (left) and downslope (right) side for θ=30°, Ra=1.37μm

Comparing the cases for the three angles, we can safely deduce that the crown height on the upslope side h_1 and the crown height on the downslope side h_2 have about the same range of values with small deviation. Furthermore, they both have the trend to take lower values while the angle progressively increases, with the change in the case of the h_2 being more obvious. There cannot be deduced such a relation between the α_1 and α_2 angles, but we can safely claim that, the values of the α_1 angle will be about the same or higher than those of the α_2 in most cases for θ=20° and θ=30° when there is not such evidence for θ=10°.

Figure 3.40 shows the crown heights for the last tile. The h_1 seems to have slightly smaller values than the h_2 and it does remain relatively constant throughout the phenomenon, while the h_2 parameter has the trend to increase. The lower values of the h_2 correspond to the lowest We numbers and the higher values to the higher We accordingly. Figure 3.41 depicts the angles on both sides of the crown, the values of the α_1 being more concentrated around higher numbers than those of the α_2. No clear trend can be seen for any of the parameters in this figure.

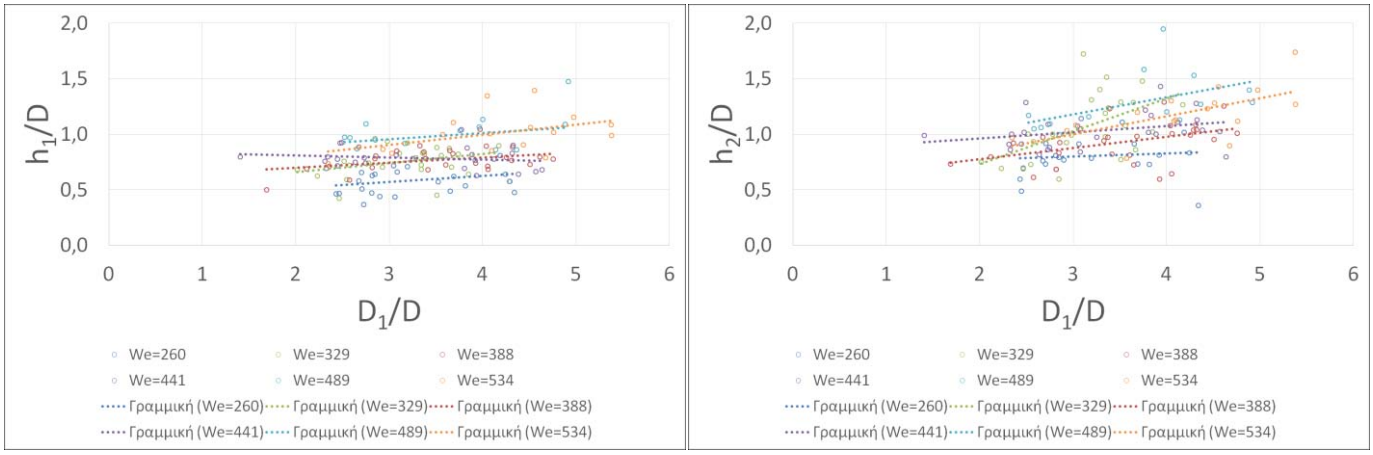

Figure 3.40: Crown height on the upslope (left) and downslope (right) side for θ=10°, Ra=6.99μm

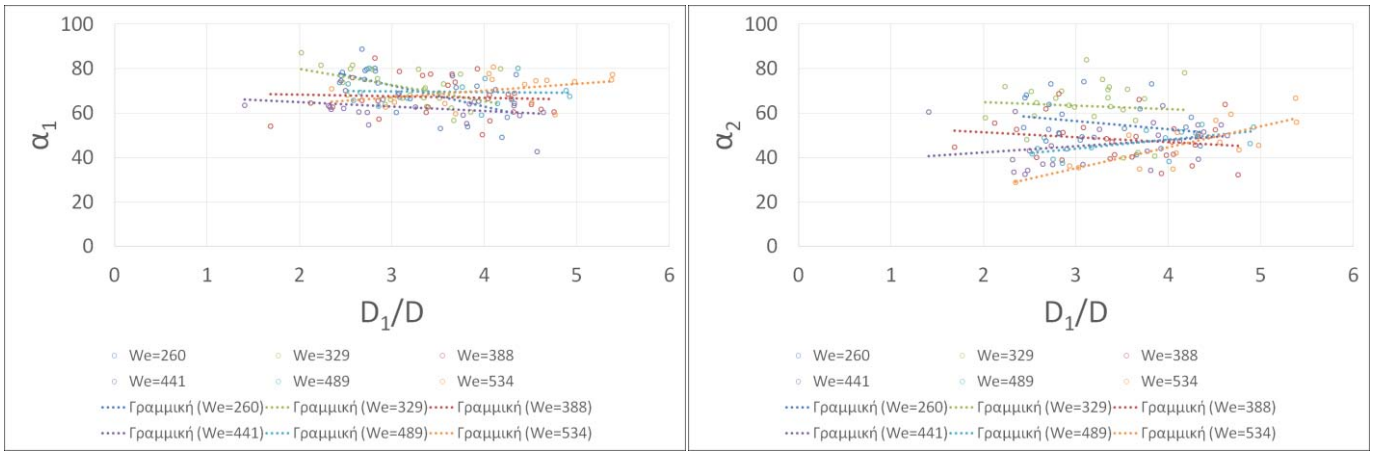

Figure 3.41: Crown angle on the upslope (left) and downslope (right) side for θ=10°, Ra=6.99μm

Figure 3.42 shows that the h_1 height has lower values than the h_2 ranging from 0.3 to 0.8, and it tends to remain to the same range during the evolution of the splashing, while the h_2 tends to increase. The next figure (Figure 3.43) pinpoints the difference between the angles on the two sides of the crown. The α_1 has greater values than the α_2 and it has the trend to decrease with the progress, when the α_2 tends to increase rapidly. In both cases the highest values correspond to the lowest We number but there is not a clear connection between We and α_2 for the lower values.

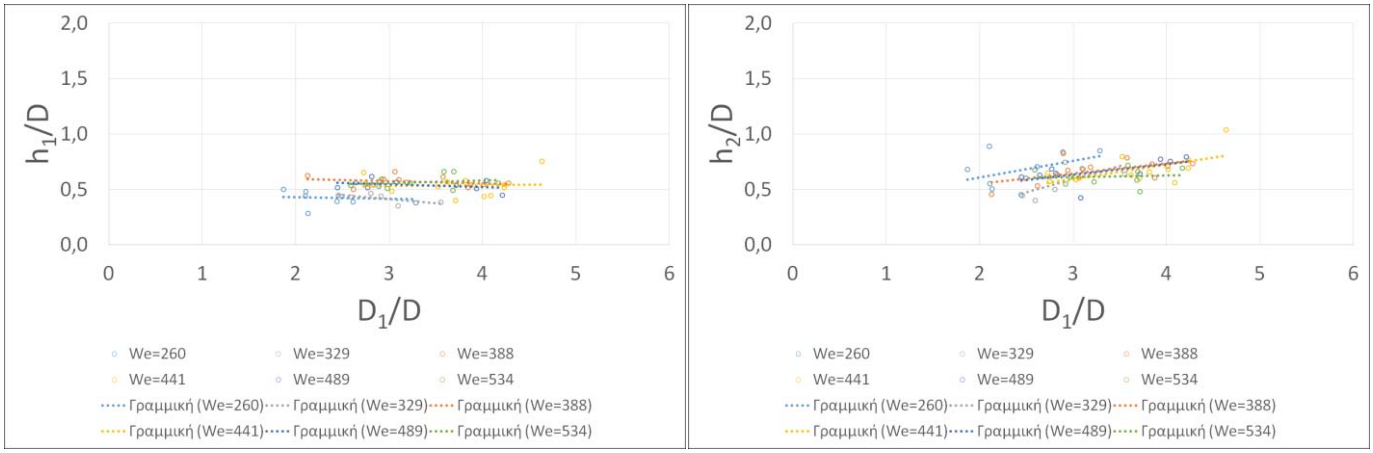

Figure 3.42: Crown height on the upslope (left) and downslope (right) side for θ=20°, Ra=6.99μm

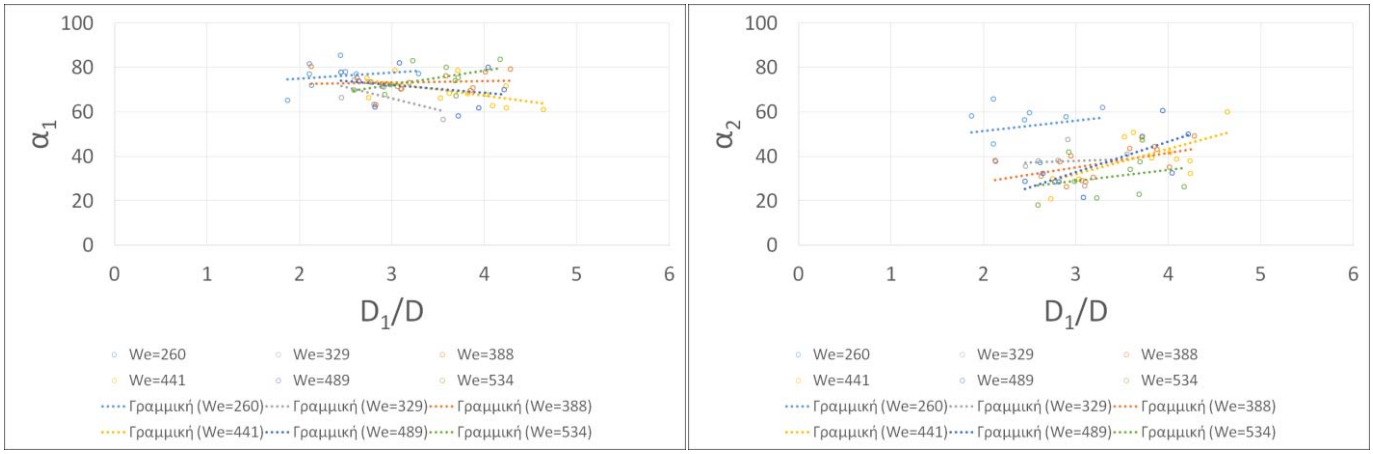

Figure 3.43: Crown angle on the upslope (left) and downslope (right) side for θ=20°, Ra=6.99μm

Figure 3.44 shows that the heights on both sides of the crown have values in the same range. They both have the trend to increase with the exelixis of the phenomenon, and it can be said that the highest values of the h_1 correspond to the highest We numbers while the same cannot be said with certainty for the h_2. In the next figure (Figure 3.45) we can see the trend of both crown angles to increase during the splashing. The α_1 have greater values than the α_2 angle. There is a peculiar angle α_2 that decreases rapidly during the phenomenon, but since it corresponds to the lowest We, we know that the transitional phenomenon did not give clear results.

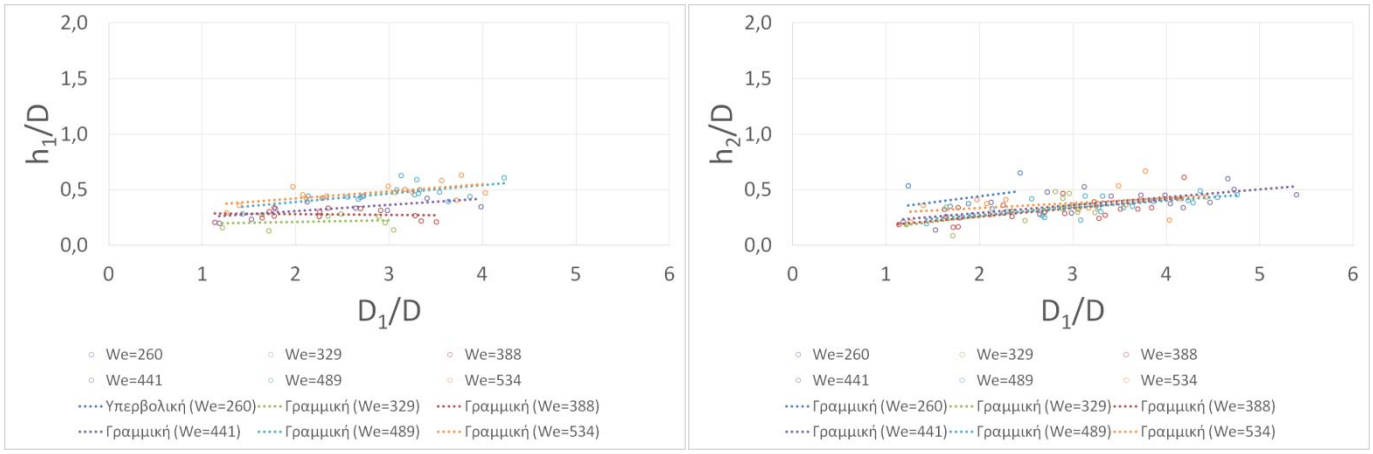

Figure 3.44: Crown height on the upslope (left) and downslope (right) side for θ=30°, Ra=6.99μm

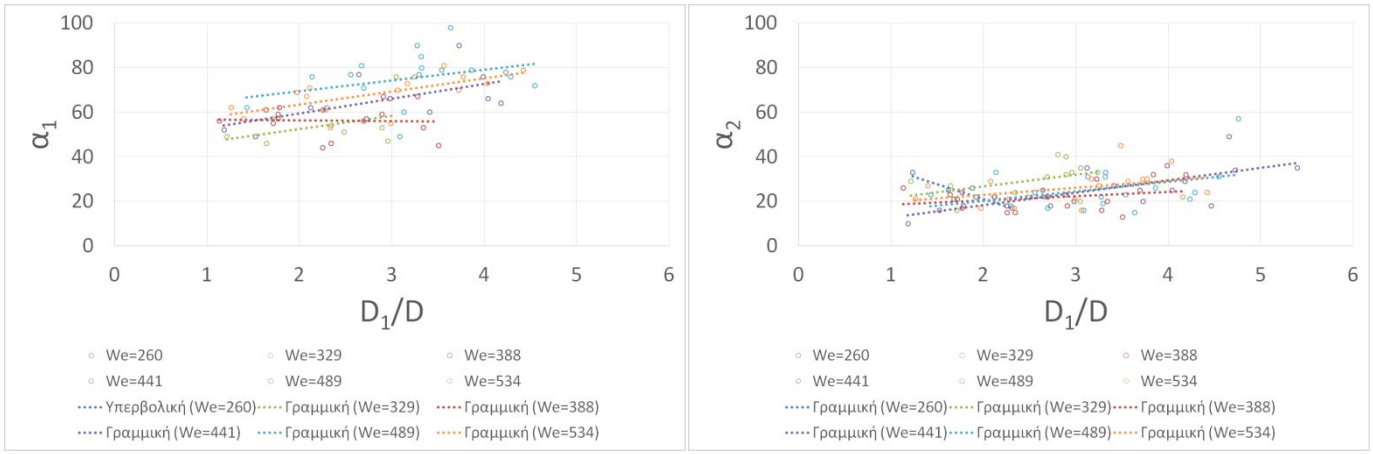

Figure 3.45: Crown angle on the upslope (left) and downslope (right) side for θ=30°, Ra=6.99μm

The comparison between the three tiles reveals the trend of both the crown heights to decrease with the increase of the angle from θ=10° to θ=30°. Even though the results are not conclusive, we can claim that both the heights increase during the phases of the phenomenon on all the angles. The α_1 and α_2 angles present some similarities as to their values in each of the three cases, but no further conclusions can safely be made about their trends or their relation with the droplet We numbers.

3.3 Roughness effect on droplet impingement

In Figure 3.46 we can see the similarities and differences between the three different tiles for the 6 droplet We numbers in the case of 10° angle. A general view reveals that the crown height on the upslope side h_1 increases during the evolution of the phenomenon. At low We numbers the tile with the highest roughness has the largest values of h_1, but as the We number progressively increases, the difference between this and the other two tiles becomes less evident until all three tiles seem to create the same crown height h_1 in the last diagram.

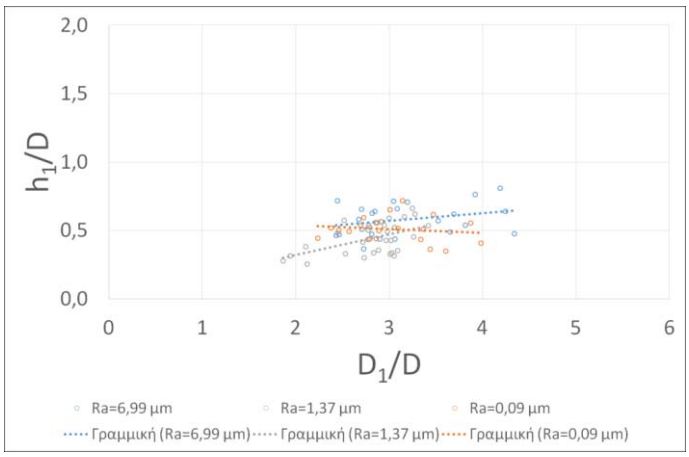

We=260

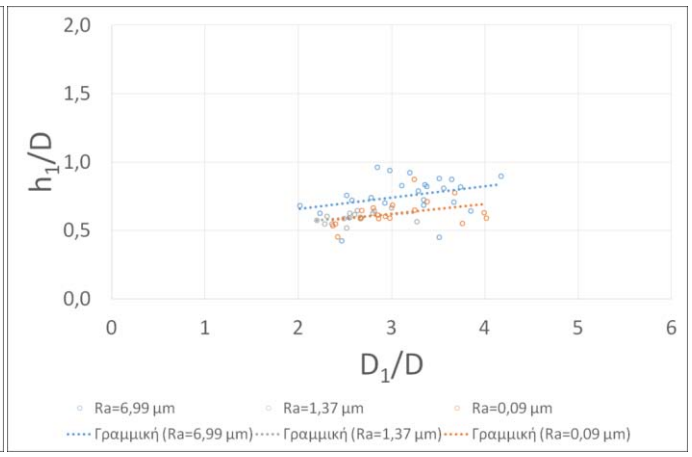

We=329

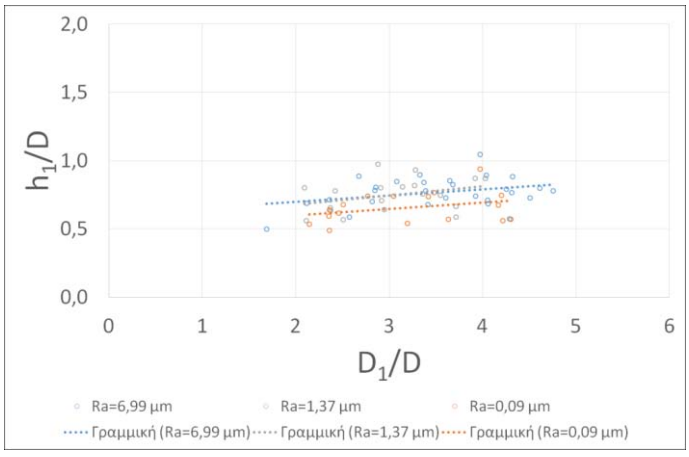

We=388

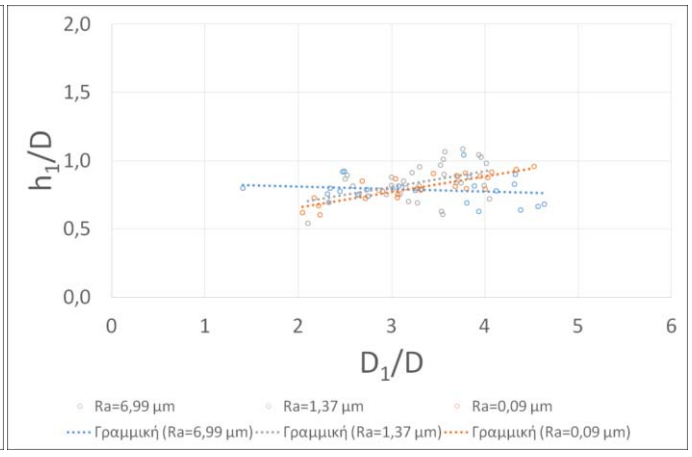

We=441

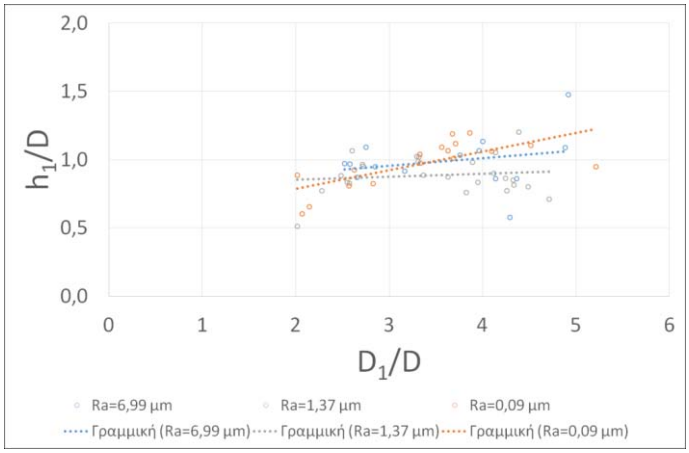

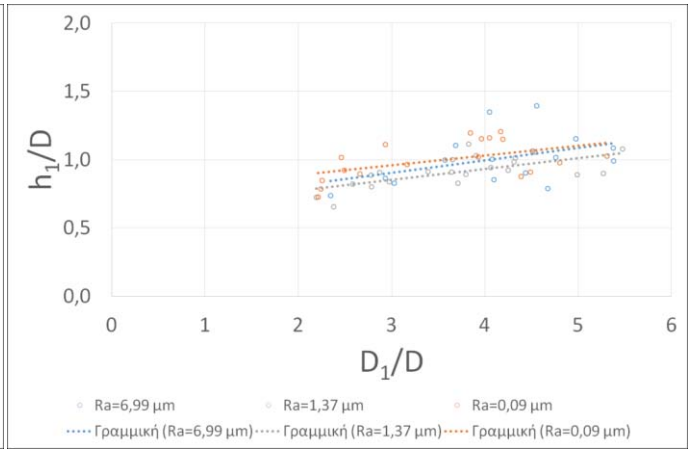

We=489 We=534

Figure 3.46: Crown height on the upslope side for θ=10°, for all six We numbers in sequence

In Figure 3.47 we observe that in the case of θ=20° there is no clear trend of the h_1 increasing or decreasing for the different We numbers. Again the tile with the highest roughness seems to create the higher h_1 at low We, but as the distance between the syringe and the tile surface increases the opposite happens. On the contrary the tile with the lowest roughness creates the lowest h_1 at low We and as the We numbers increase it ends up creating the highest h_1. In this case the values of the specific parameter seem less scattered than they are in the case of θ=10°.

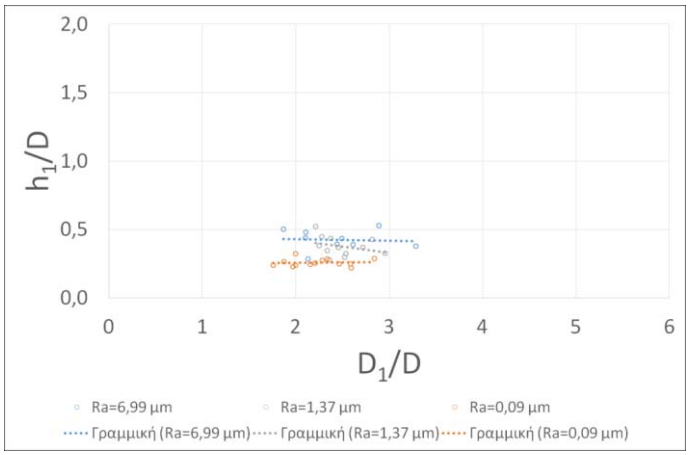

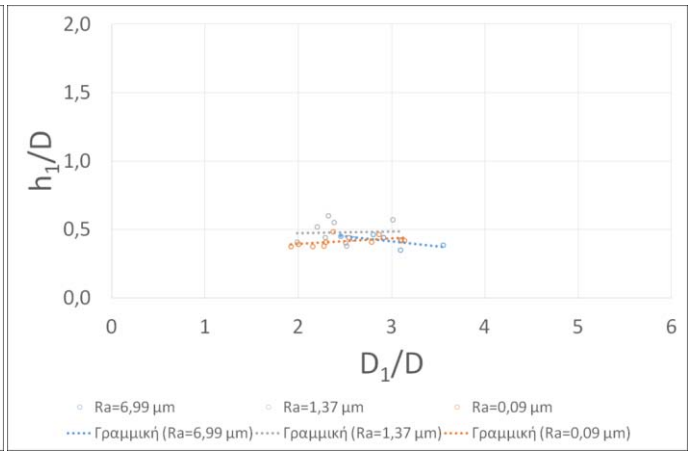

We=260 We=329

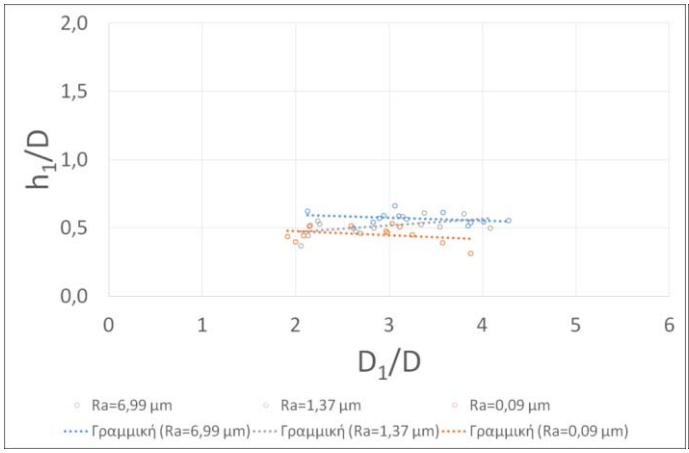

We=388

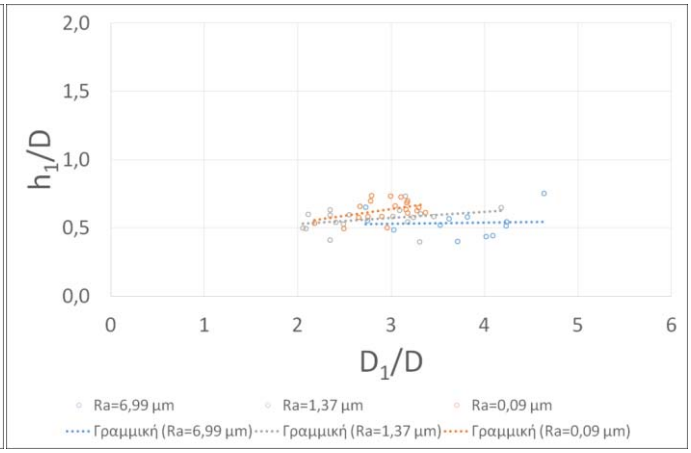

We=441

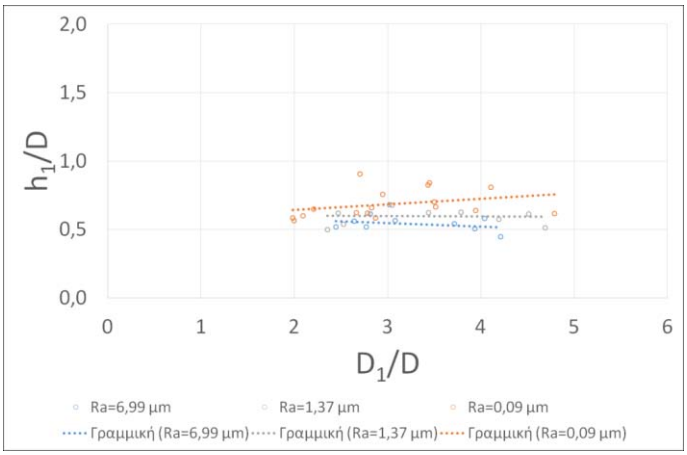

We=489

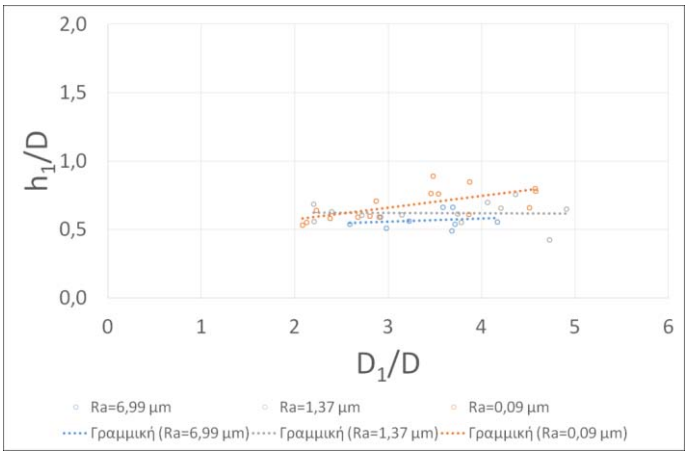

We=534

Figure 3.47: Crown height on the upslope side for θ=20°, for all six We numbers in sequence

In this figure (Figure 3.48) we see that the trend of the h_1 to slightly increase during the phenomenon still applies for a 30° angle. This time there is no clear conclusion as to the We effect on the h_1 height, because all three tiles have similar responses to the change of the distance between the tile and the syringe. It is obvious that the values of h_1 are even less scattered than before, probably due to the bigger angle which tends to make the phenomenon more difficult to happen in the first place, which means that in the bigger the angle, the less important the surface roughness.

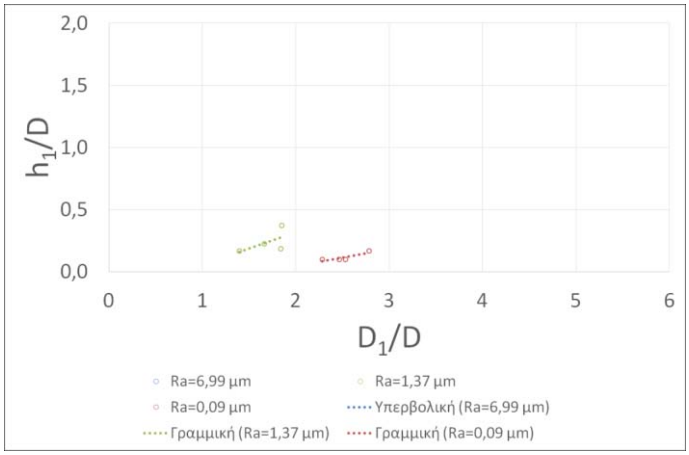

We=260

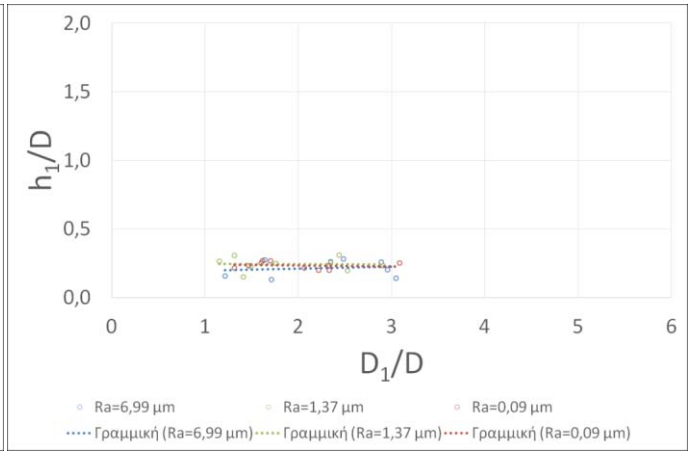

We=329

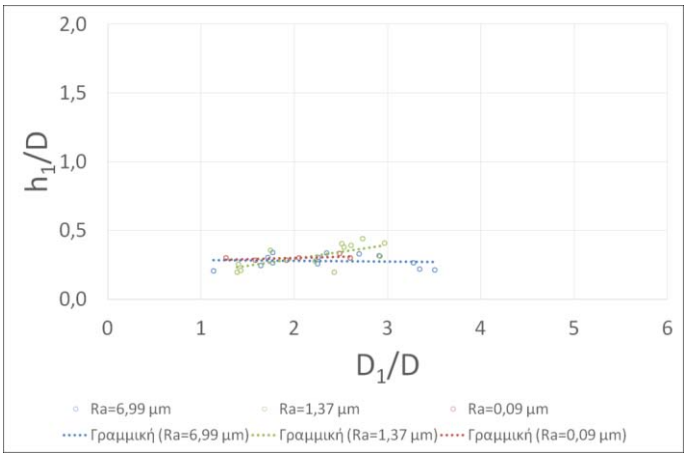

We=388

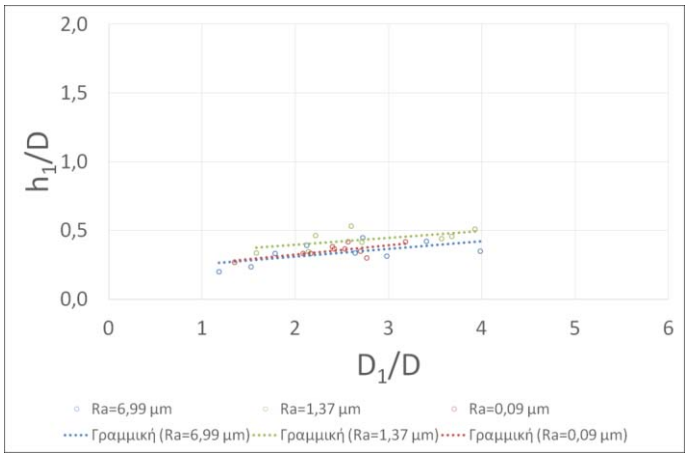

We=441

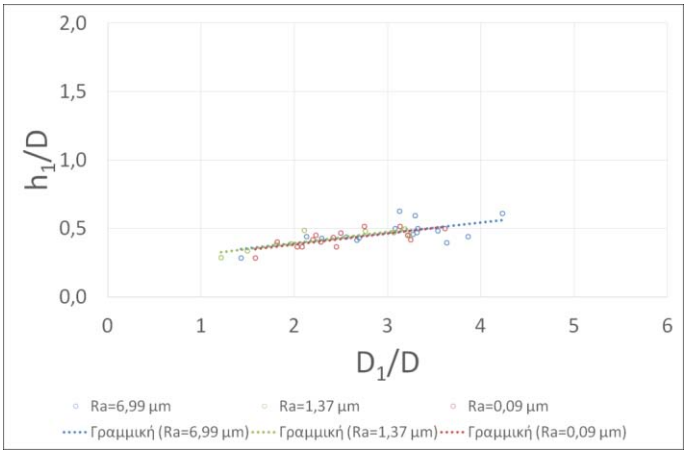

We=489

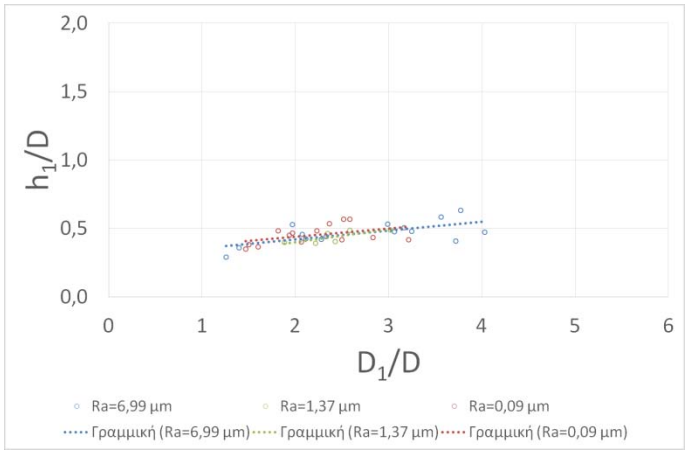

We=534

Figure 3.48: Crown height on the upslope side for θ=30°, for all six We numbers in sequence

In Figure 3.49 the values of h_2 are presented. For this parameter, just like for the h_1, we can observe a trend to increase during the evolution of the phenomenon. It can be said that the tile with the smallest

roughness never has the highest values, while the two other present similar behaviours with no other clear deduction to be made.

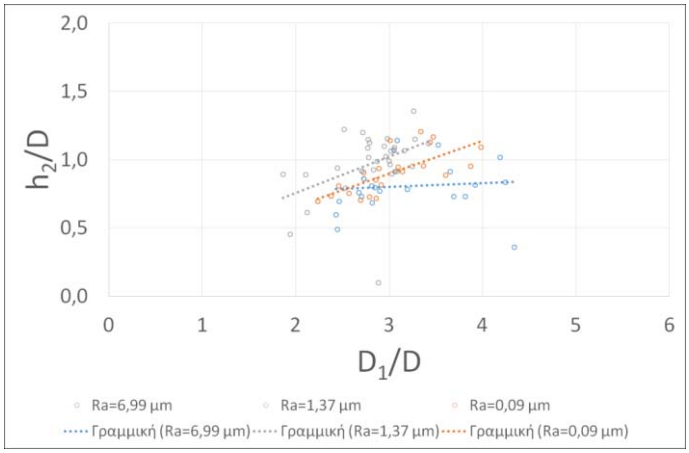

We=260

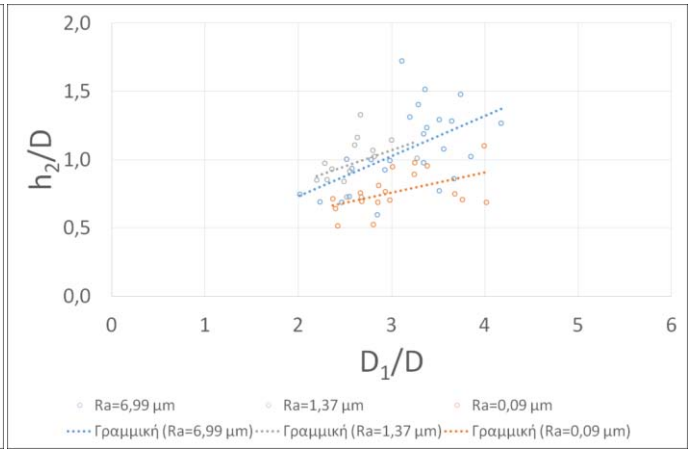

We=329

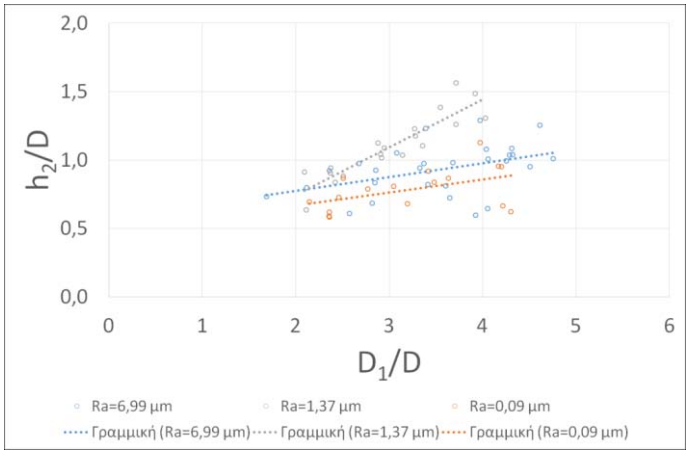

We=388

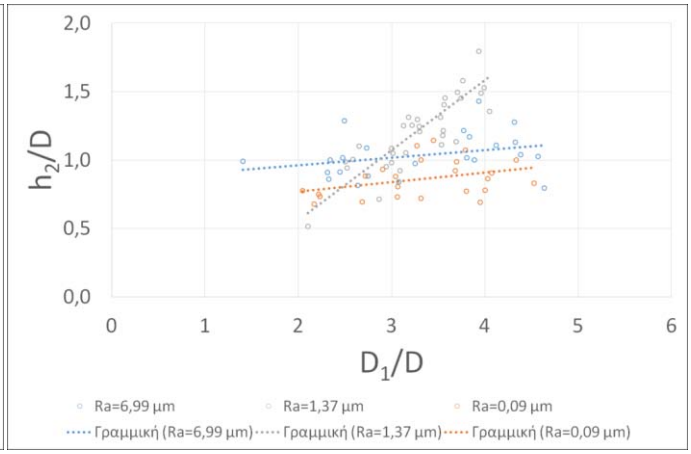

We=441

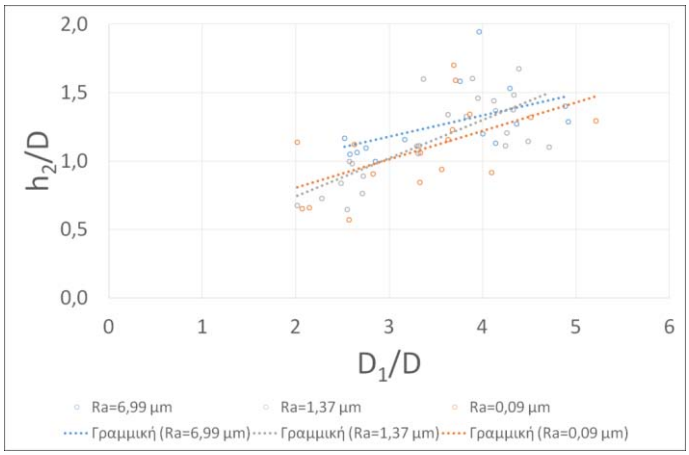

We=489

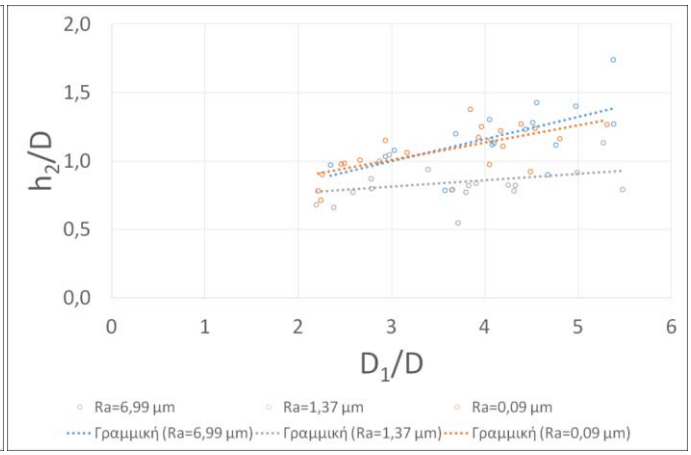

We=534

Figure 3.49: Crown height on the downslope side for θ=10°, for all six We numbers in sequence

A general view of Figure 3.50 reveals the general tendency of the h_2 parameter to increase during the evolution of the splashing in the case of θ=20°, like before. We cannot claim with certainty that the values are less scattered than before, but we see that the tile with the smallest roughness never has the lowest values of h_2, except for the first We while the tile with the highest roughness never has the highest values. Additionally, we observe a trend of the tile with the highest roughness, to decrease in some We numbers which may be due to a faster collapsing of the crown on the downslope side because of stagnating water on that side.

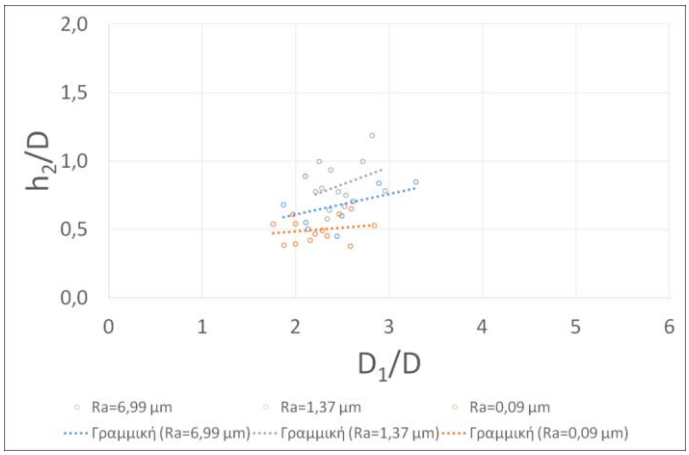

We=260

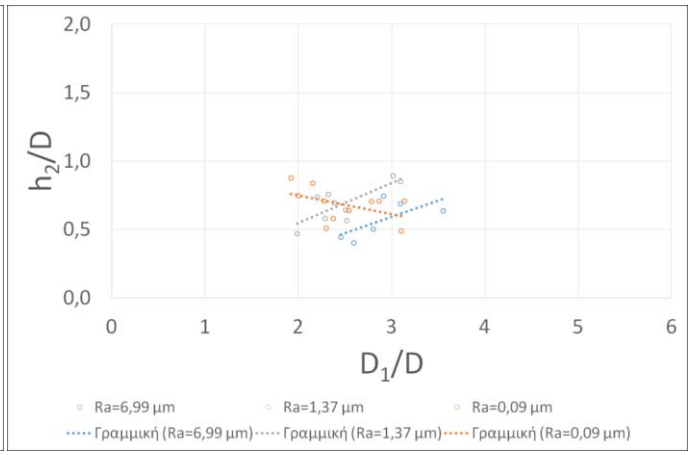

We=329

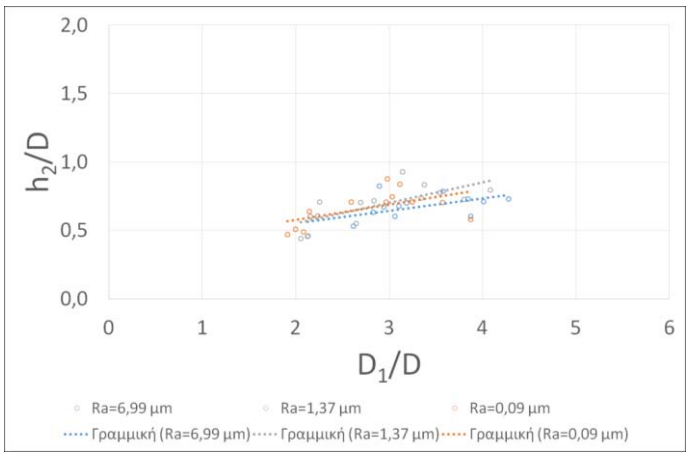

We=388

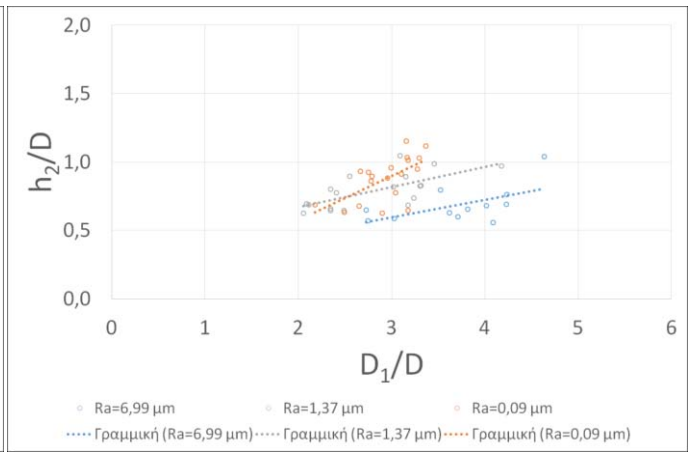

We=441

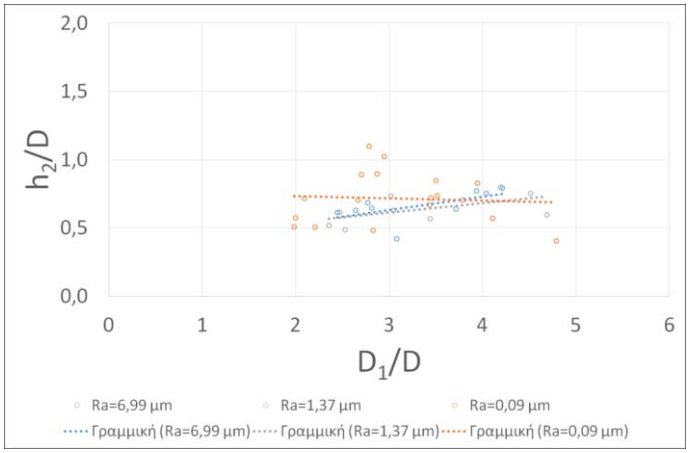

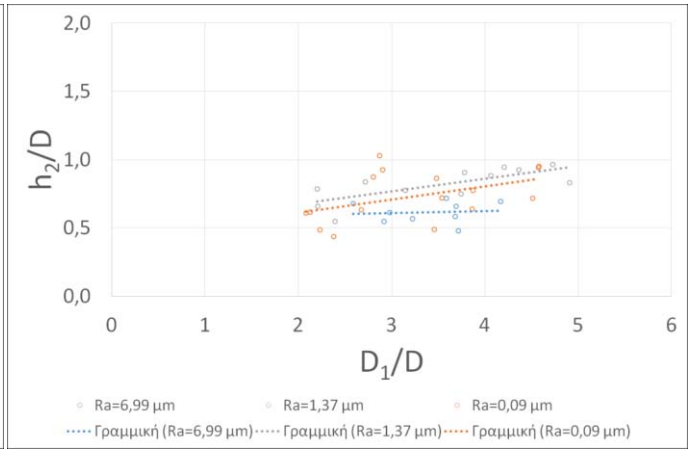

We=489 We=534

Figure 3.50: Crown height on the downslope side for θ=20°, for all six We numbers in sequence

For θ=30° (Figure 3.51) we observe again the general trend of the h_2 to increase while the splashing progresses. This time it is more obvious that the values of the specific parameter are less scattered than in the previous angles. It is safe to claim that the tile with the highest roughness has lower values than the other two, for all We numbers, which complies with the experiment for θ=20°. The tile with the lowest roughness has the higher values with the exception of the first diagram, which depicts the transitional phenomenon. This comes in contrast with the corresponding experiment for θ=10°.

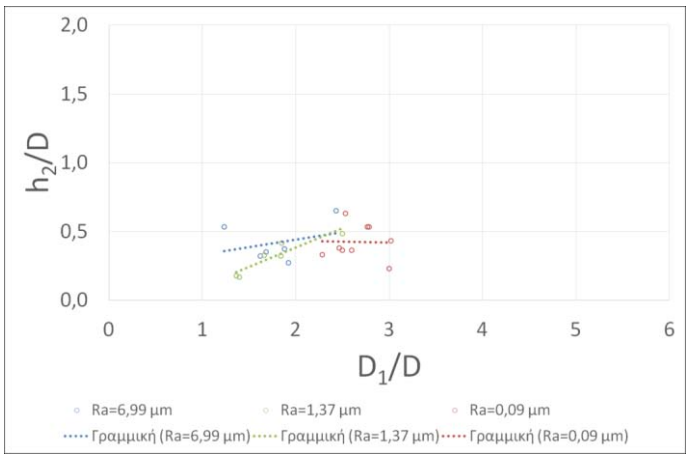

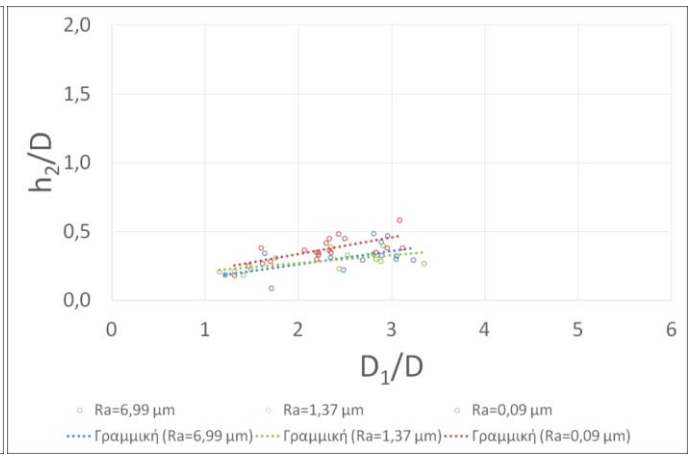

We=260 We=329

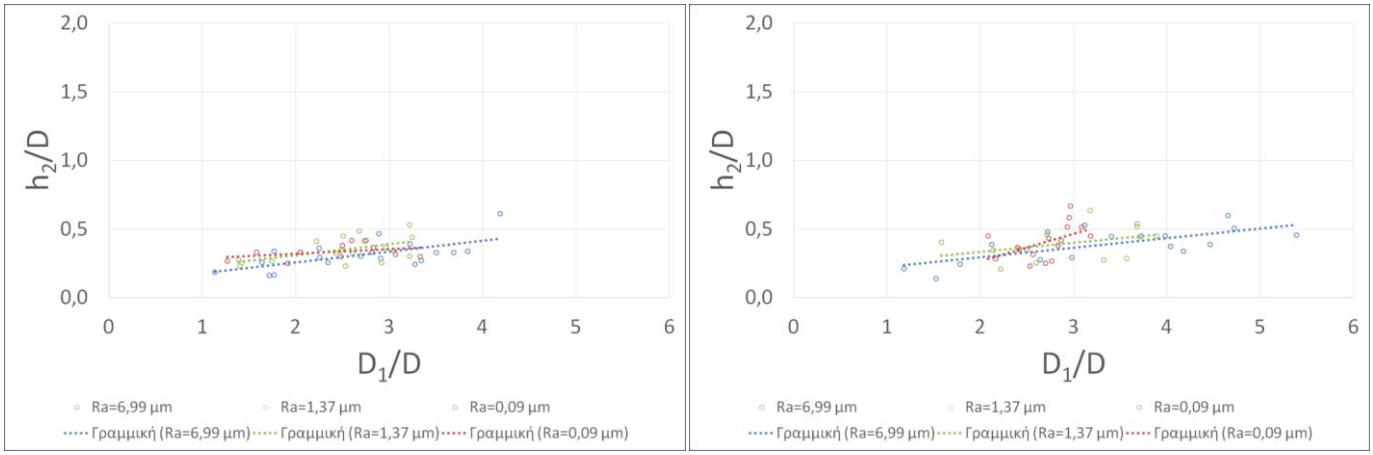

We=388 We=441

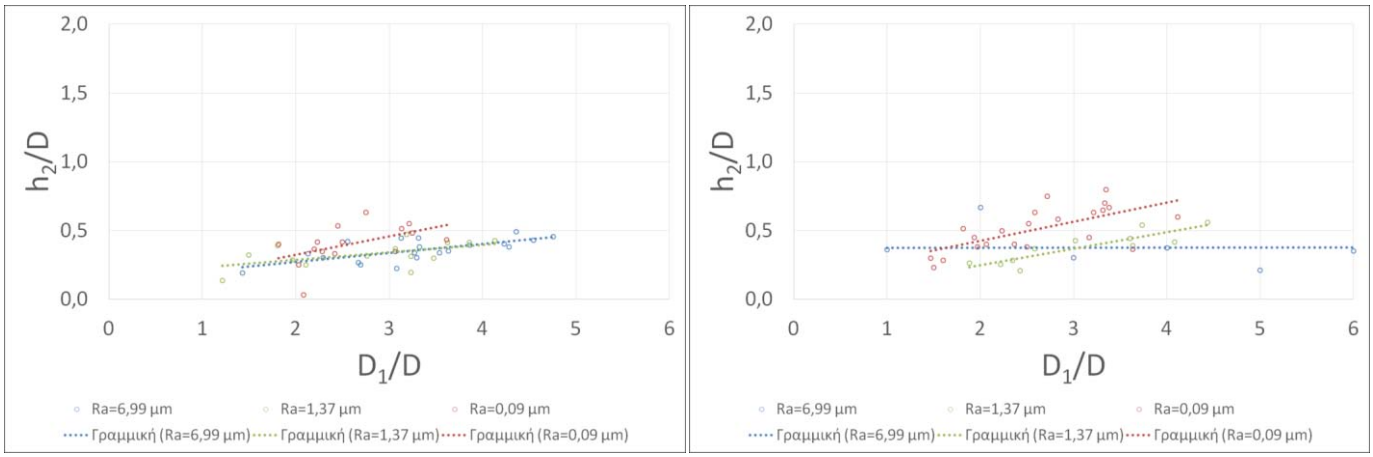

We=489 We=534

Figure 3.51: Crown height on the downslope side for θ=30°, for all six We numbers in sequence

In Figure 3.52 we see the transitions of the α_1 angle. For the lower We numbers it seems to decrease during the evolution of the phenomenon, but as the We increases it remains constant or even increases slightly for the highest We. The tile with the highest roughness appears to create the largest α_1 at low We, and the smallest at the higher We. No certain conclusion can be made for the other two tiles. Another important conclusion is that in the experiments for the low We, the results seem scattered, but with a closer look at the final diagram, we see that for the highest We they tend to gather in a small range of values, which means that the effect of the roughness becomes more insignificant with the increase of the distance between droplet and target.

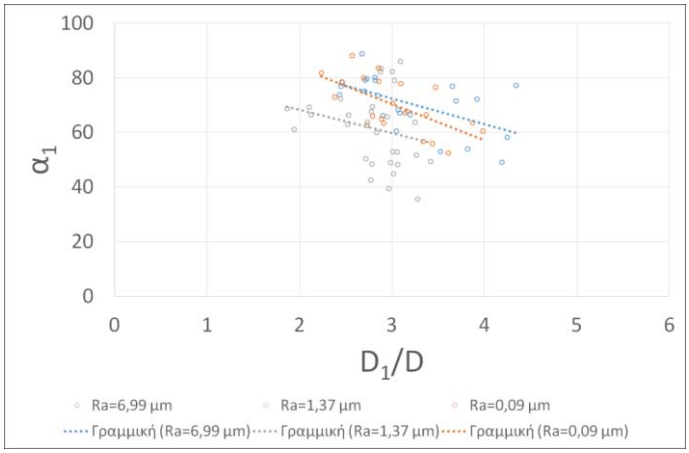

We=260

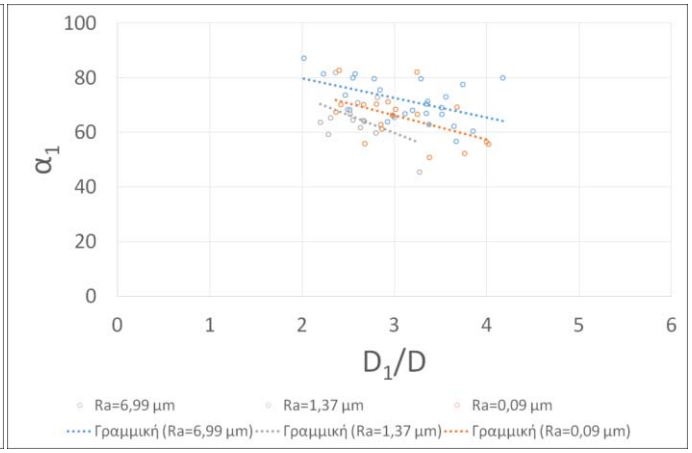

We=329

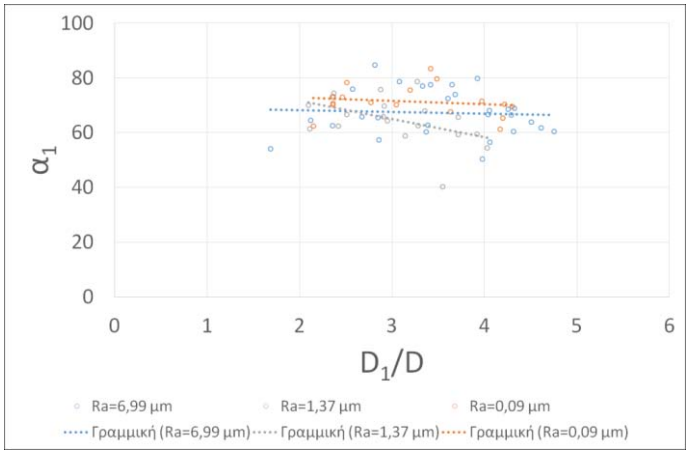

We=388

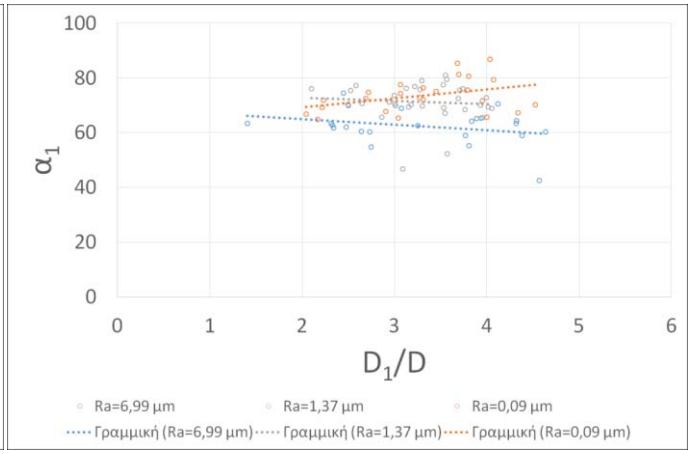

We=441

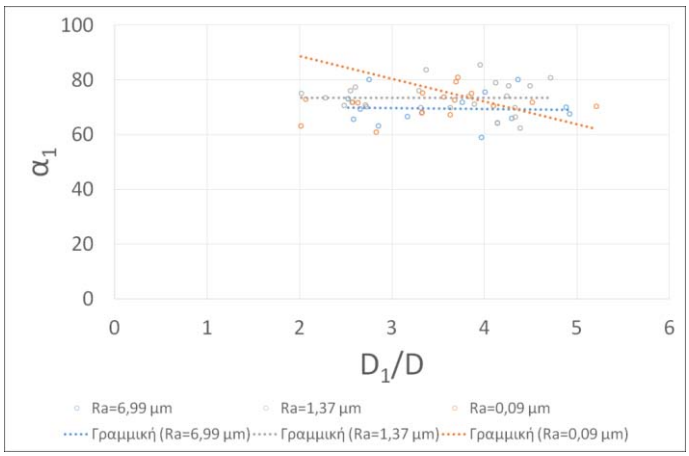

We=489

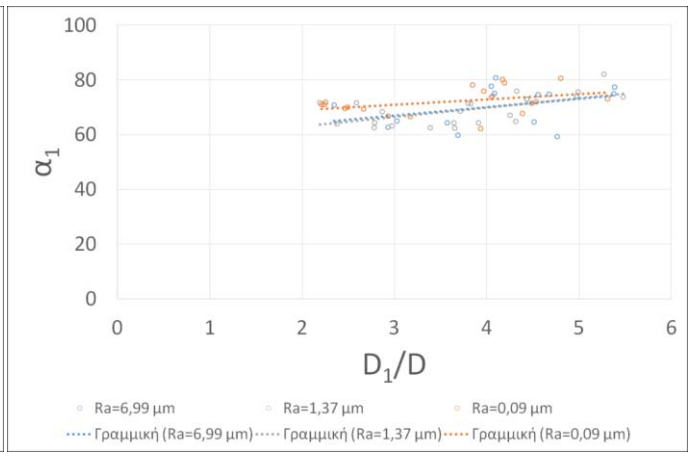

We=534

Figure 3.52: Crown angle on the upslope side for θ=10°, for all six We numbers in sequence

In the case of θ=20° (Figure 3.53), the results are even more inconclusive. Other than the fact that they all range from about 50° to 90° for all We and all three roughnesses, there is no clear trend in any

experiment. Furthermore, the diagrams do not indicate any connection between the roughness and the outcome. This can be attributed to the fact that the angle on the upslope side of the crown varies when the crown is not formed on a level surface depending on the water film that pre-exists there or any bulks of water from previous collisions. There are not enough data to claim that the scattering of the results tends to decrease in the last diagram compared with the rest like it was obvious in the case of θ=10°.

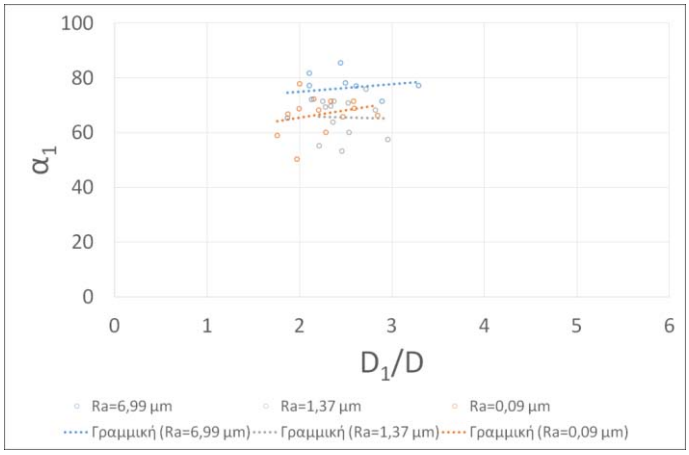

We=260

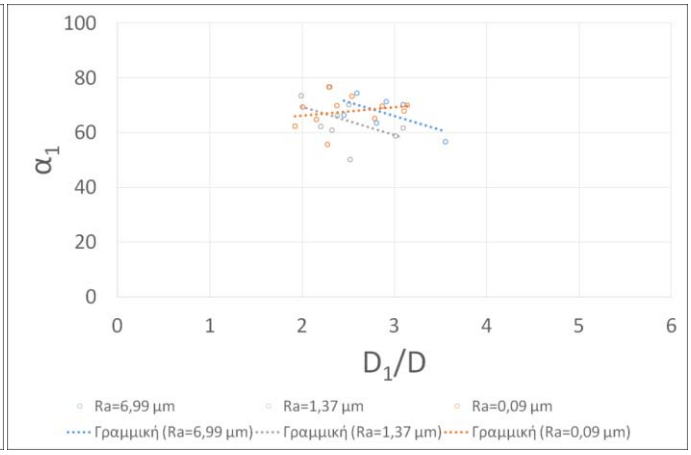

We=329

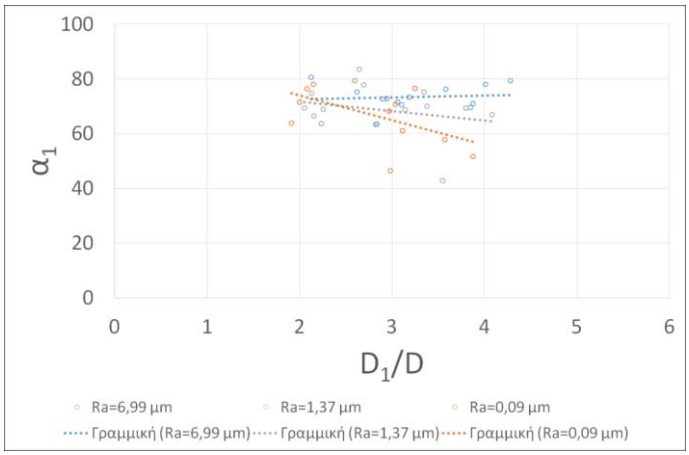

We=388

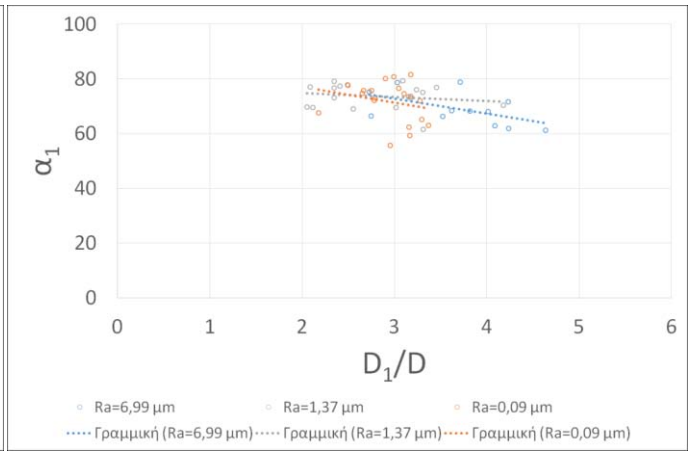

We=441

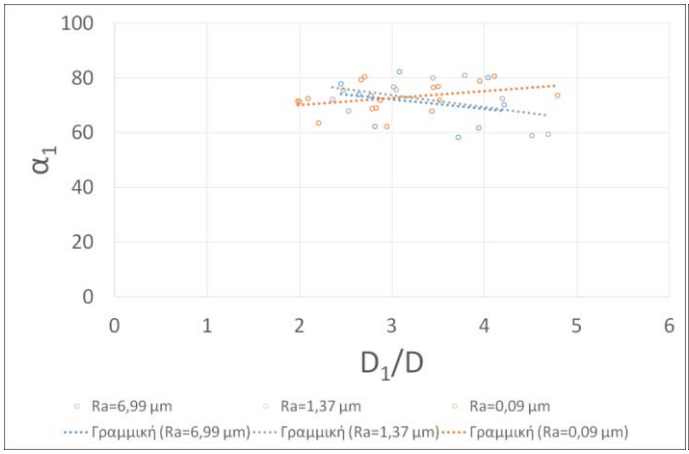

We=489

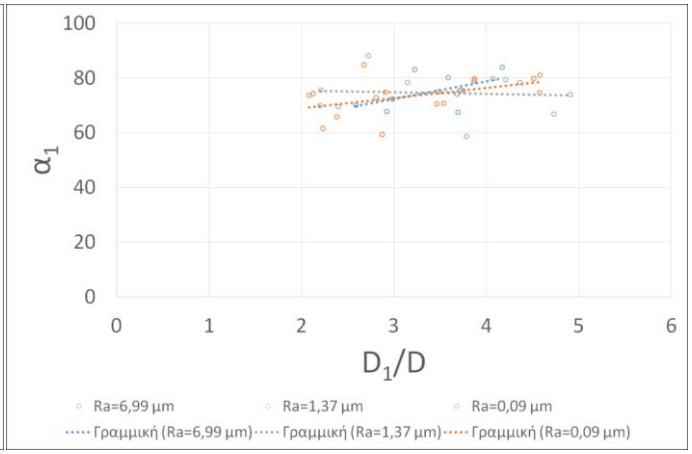

We=534

Figure 3.53: Crown angle on the upslope side for θ=20°, for all six We numbers in sequence

A general view of Figure 3.54 reveals four things. First of all, the first diagram has not enough data because it corresponds to the lowest We number were the transitional phenomenon takes place and therefore we cannot deduce anything from it. Secondly there is an obvious trend, in most experiments, of the α_1 to increase with the evolution of the phenomenon, or, in some cases, to remain constant around a specific value. The third thing is that the tile with the lowest roughness forms the lowest α_1 angles throughout the experiments. And last but not least, it can be said that while the results seem scattered for the three tiles for the lowest We, they appear to converge in a way for the highest We, which agrees with the results from Figure 3.53. Therefore, the roughness does play a more significant role in the α_1 angle when the droplet We number is small and the opposite.

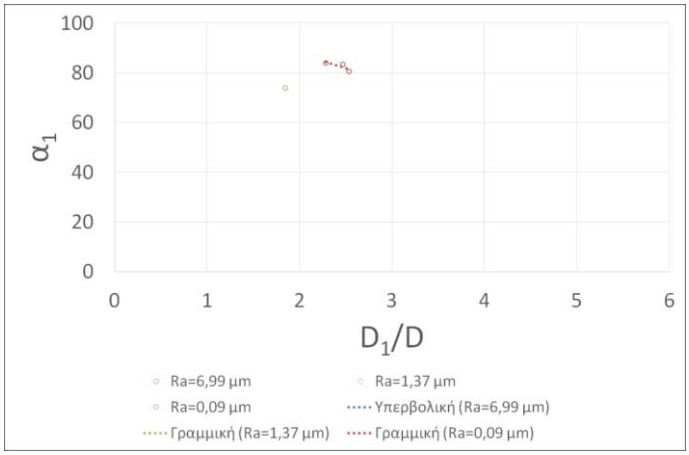

We=260

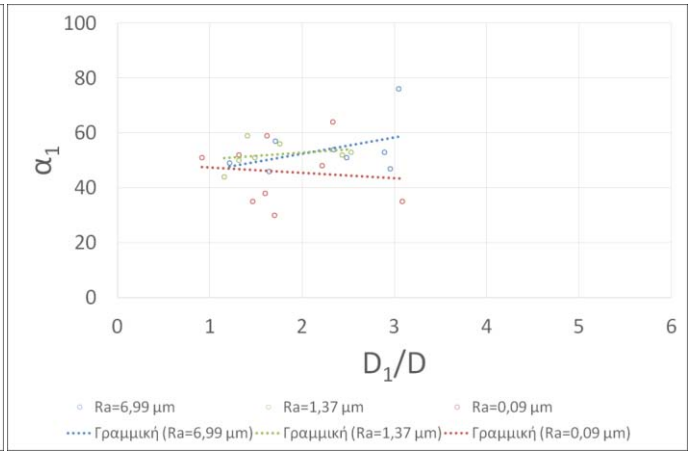

We=329

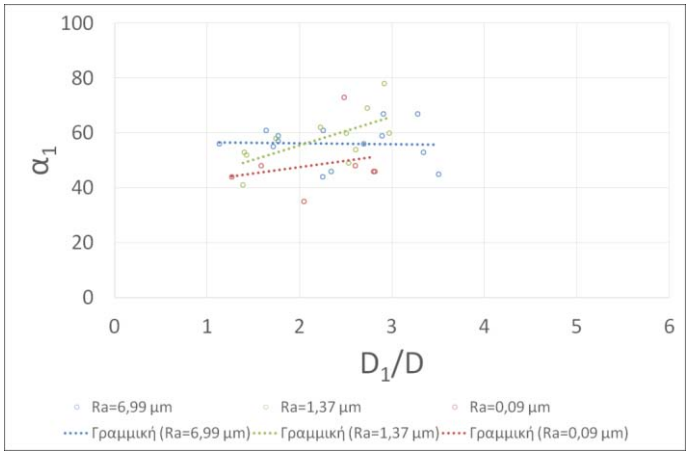

We=388

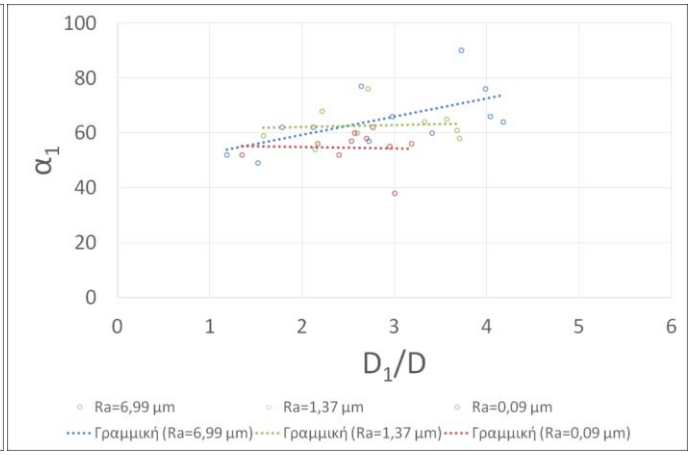

We=441

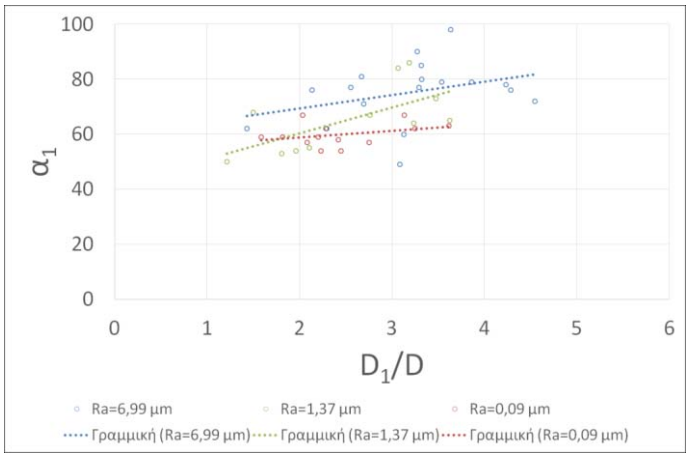

We=489

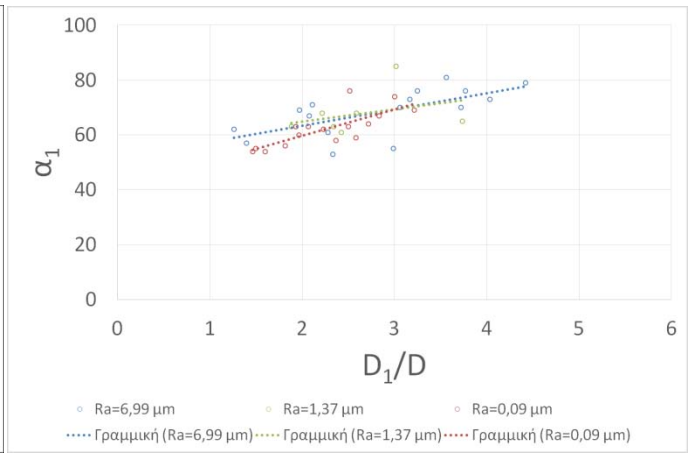

We=534

Figure 3.54: Crown angle on the upslope side for θ=30°, for all six We numbers in sequence

From Figure 3.55 we can see that at low We numbers there is no clear trend of the α2 parameter. As the We increases, it seems that the α_2 angle tends to increase during the evolution of the phenomenon. Furthermore, the tile with the highest roughness generally has the lowest values with only one exception, when the one with the middle roughness is constantly the one with the highest values. The results again seem to converge for the highest We, which indicates that the roughness doesn't affect significantly the formation of the α_2 angle when the distance between the droplet and the target increases.

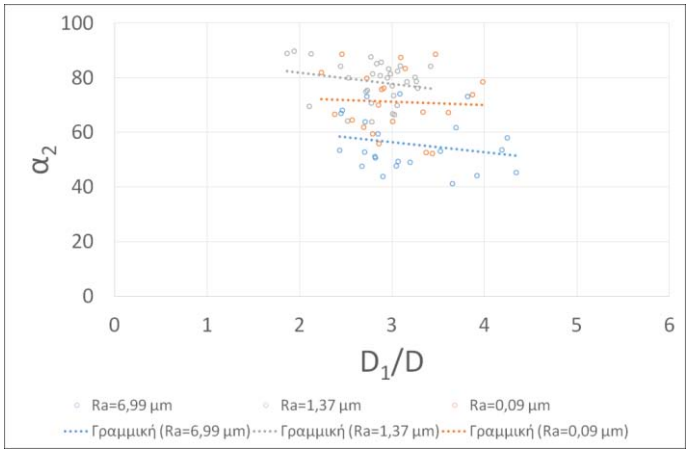

We=260

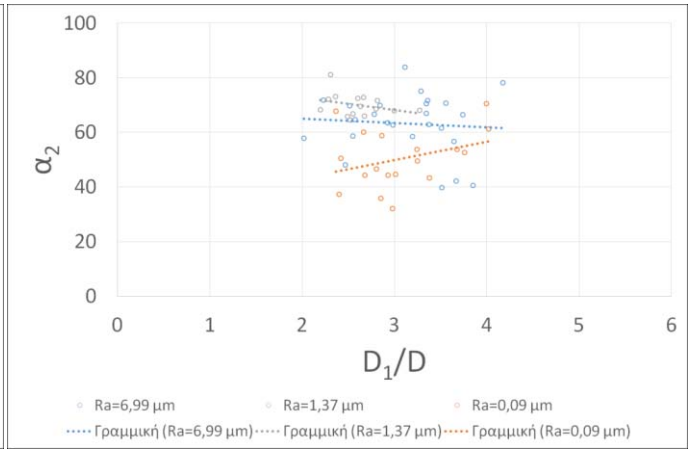

We=329

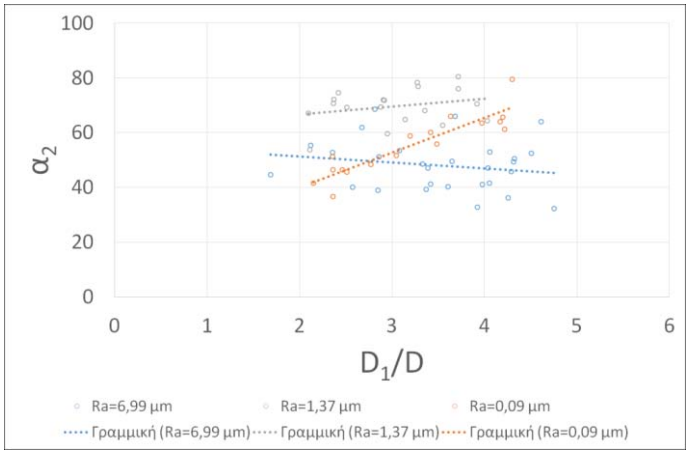

We=388

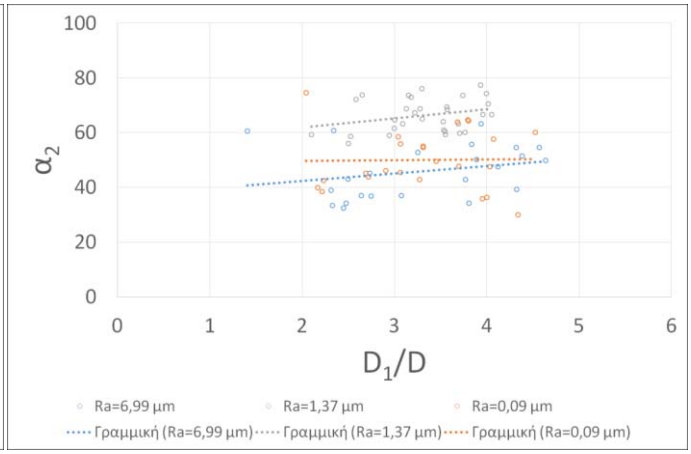

We=441

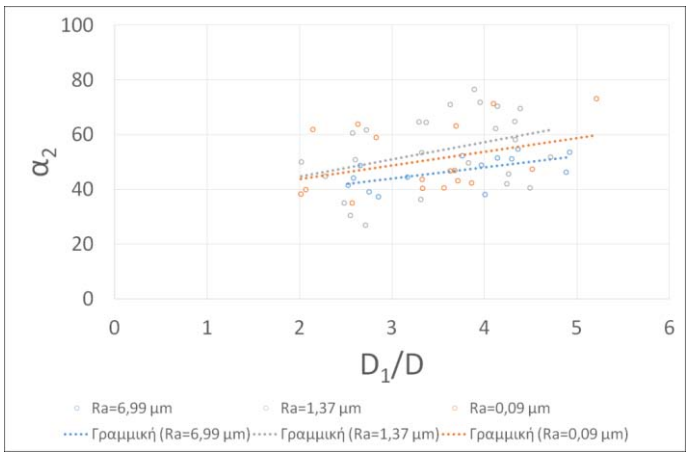

We=489

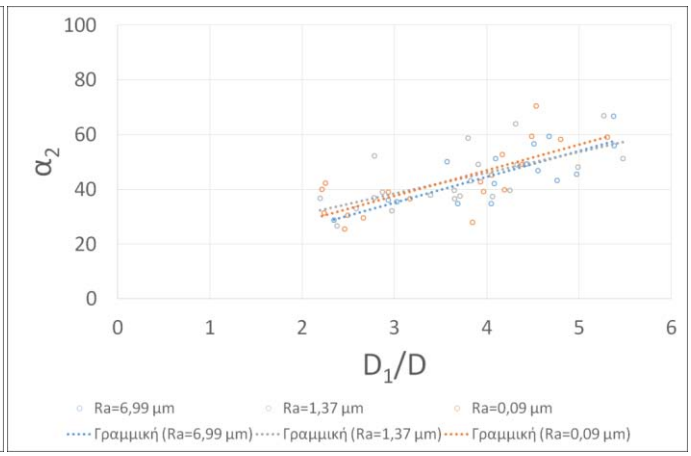

We=534

Figure 3.55: Crown angle on the downslope side for θ=10°, for all six We numbers in sequence

In the case of θ=20°, the Figure 3.56 shows that conclusions cannot be reached with certainty. No obvious trend can be seen, and no connection between the roughness and the α_2 angle can be

distinguished. This is because there are not enough results in some experiments and may be due to the conditions which were described before.

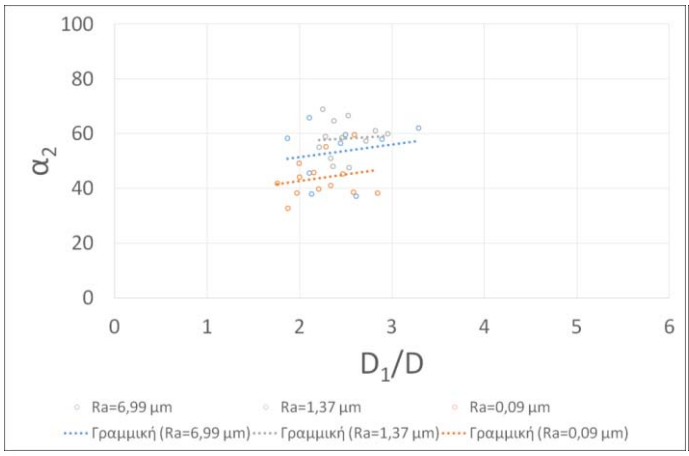

We=260

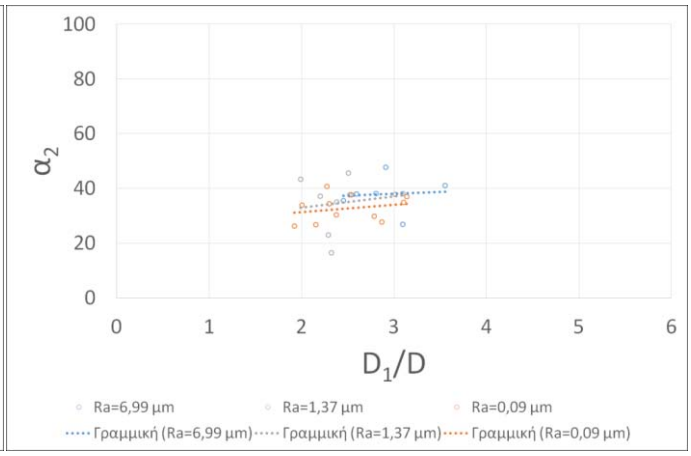

We=329

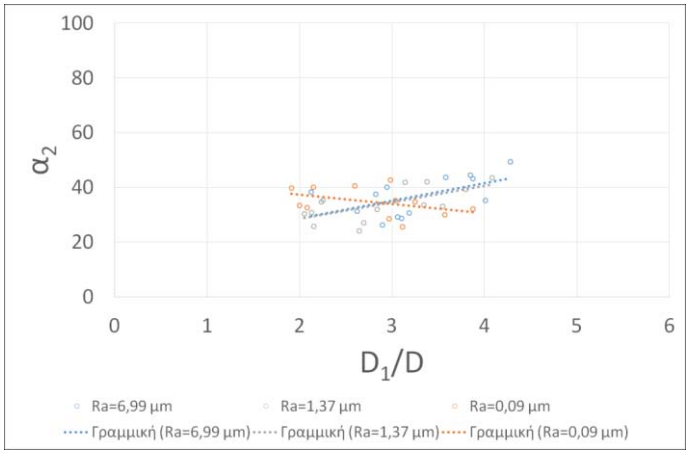

We=388

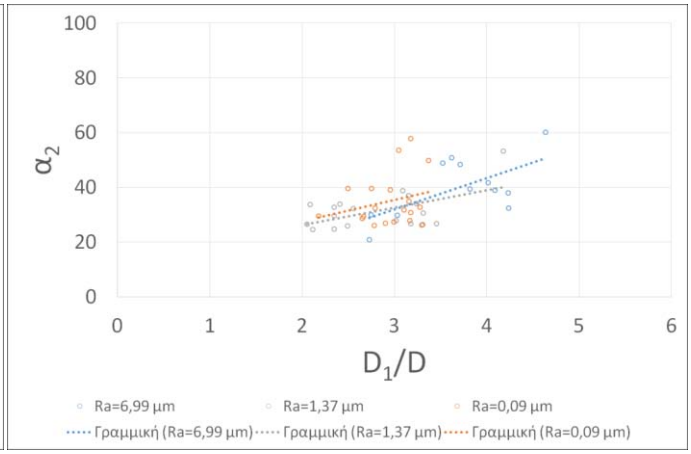

We=441

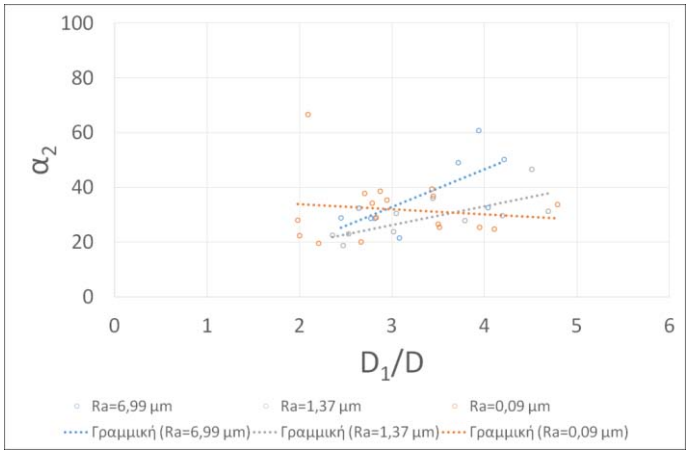

We=489

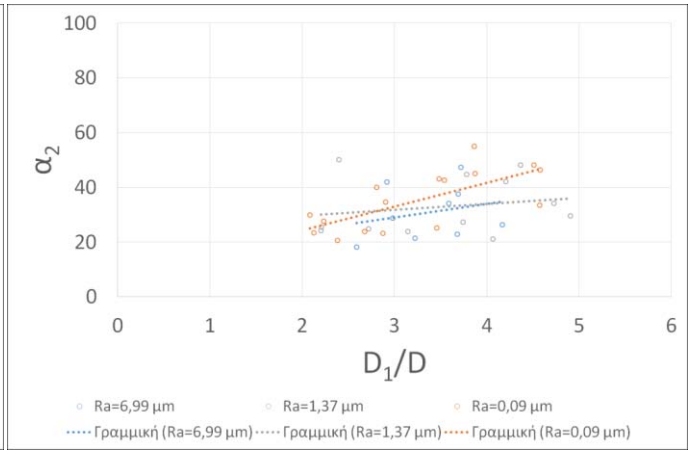

We=534

Figure 3.56: Crown angle on the downslope side for θ=20°, for all six We numbers in sequence

The last figure (Figure 3.57) shows that at the lowest We number the insufficient data due to the transitional phenomenon, don't allow us to reach a safe result for this case. For the rest experiments we can say that the tile with the lowest roughness is the one with the higher values of the α_2 angle, although for the highest We the roughness seems to play a less important role in the formation of this parameter. No certain trend can be seen in the diagrams for the α_2 behavior during the evolution of the phenomenon.

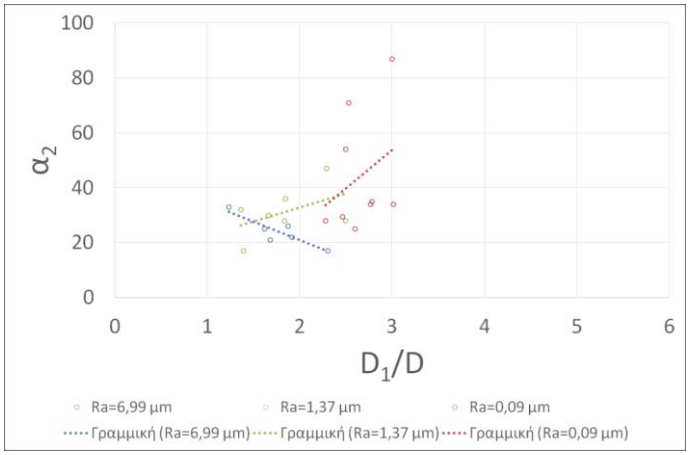

We=260

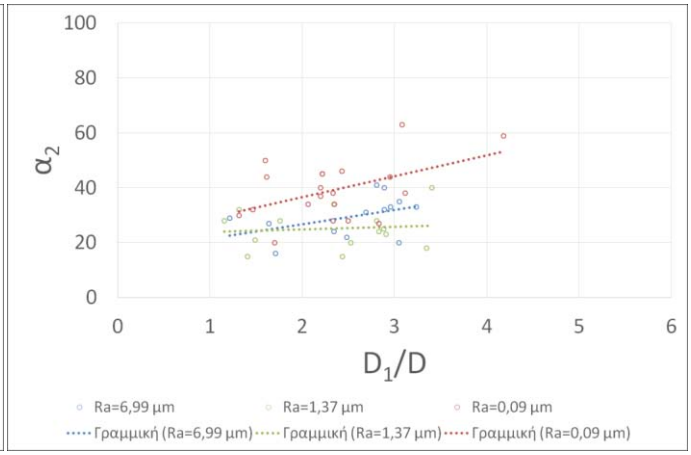

We=329

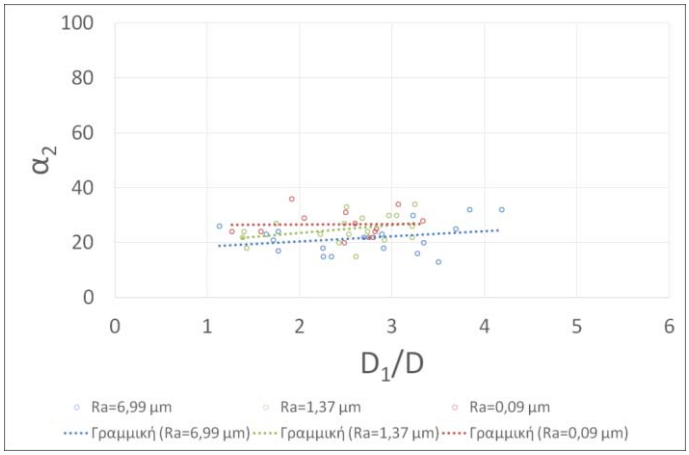

We=388

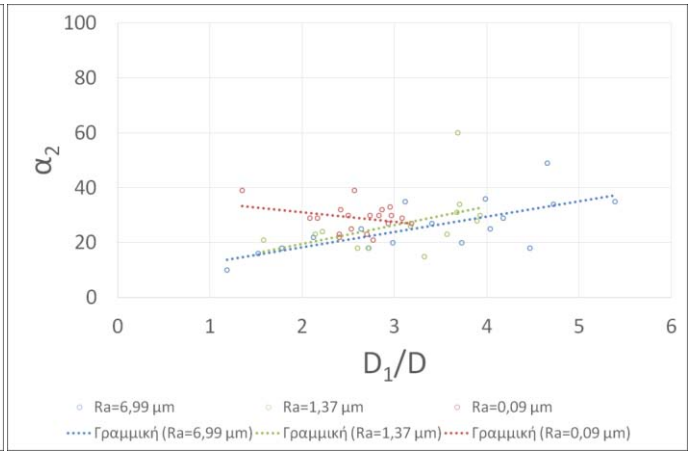

We=441

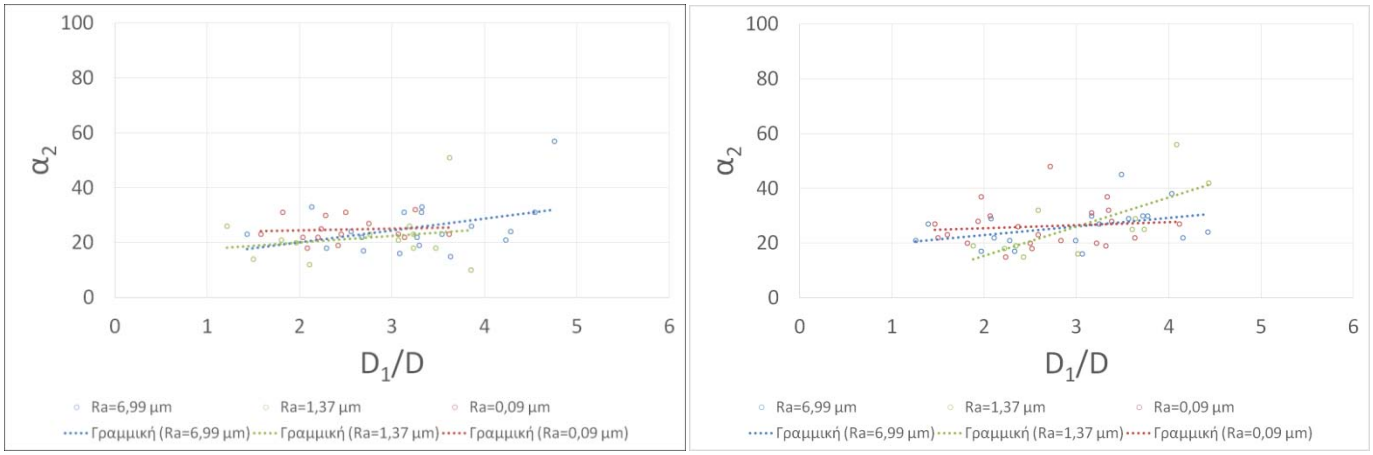

We=489 We=534

Figure 3.57: Crown angle on the downslope side for θ=30°, for all six We numbers in sequence

4. Conclusions

In the previous sections the experimental data was analyzed thoroughly for the four parameters (the crown heights on both sides and the angles between the crown and the surface) for six different We numbers listed above and three surfaces and the results revealed the trend for each one. In the next paragraph we sum up the trends for the studied parameters and we address solutions for the problems we encountered during the set up of the experiment. We also mark the points in the experiment that caused some of the results to be inconclusive in order to be taken into consideration for any future work.

1. The angle of the surface plays a significant role in the collision outcome. The larger the angle, the more difficult the splashing to occur. In the cases of the smallest angle (θ=10), the crown height was noticeably bigger than it was for θ=20 and θ=30, even at low We.

    a. For all three surfaces, the values of the h_1 are generally lower than those of the corresponding h_2 parameter for all We. Both the heights have a slight trend to increase during the evolution of the phenomenon, but there is great uncertainty.
    b. The α_2 angle seems to always take higher values than the α_1 which becomes more evident as the angle of the surface increases. In most cases the α_2 tends to increase during the evolution of the phenomenon while there is no clear trend for the α_1.

2. Regarding the effect of the droplet We number, some vague conclusions can be reached. In most cases the higher values of the h_1 and h_2 parameters occur for the higher We, although there are a few tests that contradict to that.
3. Regarding the surface roughness, for low We numbers the roughest surface creates the highest upslope crown heights (h_1). With the increase in the We, the roughness's effect decreases since all three surfaces have values of the h_1 from the same range. The same can be said about the h_2 height, as the deviation between the measurements decreases while the We increases. Observing the α_1 and α_2 we can claim that they have a similar trend with the h_1 and h_2 as they tend to be more concentrated for higher We. The surface with the highest roughness has the highest values of α_1 for the low We when no such thing can be said for the α_2.
4. A parameter that was not considered in this work is the droplet impingement frequency. It would be important to measure the way the frequency of the droplets affects the crowns and extract a relation between the two.
5. Regarding the experimental setup

    a. any light source that is powered by alternate current must be avoided due to the flickering effect.
    b. the camera must have a global shutter, in order to be able to capture the whole frame at a single instant. Any other capturing method will give deformed images that won't be able to be used to describe such an instantaneous phenomenon.
    c. The current control valve in the pressure tank that feeds water to the syringe, should be replaced with a high accuracy valve as drift in the frequency of the impinging droplets may affect the crown's characteristics.
    d. Alternatively, the set up would benefit from the use of a syringe pump instead of the pressure vessel.

5. External Image sources

(Figure 1.1): https://www.aps.org/about/physics-images/archive/redsplash.cfm?fbclid=IwAR2-b1j8vT8SI9p308pbddQ7CvSI6C8npotWvoIVtRiUT0Lu4Bzxb028zn0

6. References

Alghoul, S. K., Eastwick, C. N., & Hann, D. B. (2011). Normal droplet impact on horizontal moving films: An investigation of impact behaviour and regimes. *Experiments in Fluids*. https://doi.org/10.1007/s00348-010-0991-0

Asadi, S., & Passandideh-Fard, M. (2009). A Computational Study on Droplet Impingement Onto a Thin Liquid Film. *The Arabian Journal for Science and Engineering*.

Bremond, N., & Villermaux, E. (2006). Atomization by jet impact. *Journal of Fluid Mechanics*. https://doi.org/10.1017/S0022112005007962

Coghe, a, Brunello, G., Cossali, G., Marengo, M., & TeMPE-CNR, M. I. (1999). Single drop splash on thin film: measurements of crown characteristics. *ILASS Europe*.

Coppola, G., Rocco, G., & de Luca, L. (2011). Insights on the impact of a plane drop on a thin liquid film. *Physics of Fluids*. https://doi.org/10.1063/1.3555196

Cossali, G. E., Coghe, A., & Marengo, M. (1997). The impact of a single drop on a wetted solid surface. *Experiments in Fluids*. https://doi.org/10.1007/s003480050073

Cossali, G. E., Marengo, M., Coghe, A., & Zhdanov, S. (2004). The role of time in single drop splash on thin film. *Experiments in Fluids*. https://doi.org/10.1007/s00348-003-0772-0

Davidson, M. R. (2002). Spreading of an inviscid drop impacting on a liquid film. *Chemical Engineering Science*.

Deegan, R. D., Brunet, P., & Eggers, J. (2008). Complexities of splashing. *Nonlinearity*. https://doi.org/10.1088/0951-7715/21/1/C01

Engel, O. G. (1967). Initial pressure, initial flow velocity, and the time dependence of crater depth in fluid impacts. *Journal of Applied Physics*. https://doi.org/10.1063/1.1709044

Fedorchenko, A. I., & Wang, A. B. (2004). On some common features of drop impact on liquid surfaces. *Physics of Fluids*. https://doi.org/10.1063/1.1652061

Fujimoto, H., Ogino, T., Takuda, H., & Hatta, N. (2001). Collision of a droplet with a hemispherical static droplet on a solid. *International Journal of Multiphase Flow*. https://doi.org/10.1016/S0301-9322(00)00075-6

Gao, X., & Li, R. (2015). Impact of a single drop on a flowing liquid film. *Physical Review E - Statistical, Nonlinear, and Soft Matter Physics*. https://doi.org/10.1103/PhysRevE.92.053005

GREGORY, P. H., GUTHRIE, E. J., & BUNCE, M. E. (2009). Experiments on Splash Dispersal of Fungus Spores. *Journal of General Microbiology*. https://doi.org/10.1099/00221287-20-2-328

Guo, J. H., & Wang, X. Y. (2012). Simulation of the two phase flow of droplet impingement on liquid film by the lattice boltzmann method. *Journal of Hydrodynamics*. https://doi.org/10.1016/S1001-6058(11)60247-3

Josserand, C., & Zaleski, S. (2003). Droplet splashing on a thin liquid film. *Physics of Fluids*. https://doi.org/10.1063/1.1572815

Lagubeau, G., Fontelos, M. A., Josserand, C., Maurel, A., Pagneux, V., & Petitjeans, P. (2010). Flower

patterns in drop impact on thin liquid films. *Physical Review Letters*. https://doi.org/10.1103/PhysRevLett.105.184503

Lee, S. H., Hur, N., & Kang, S. (2011). A numerical analysis of drop impact on liquid film by using a level set method. *Journal of Mechanical Science and Technology*. https://doi.org/10.1007/s12206-011-0613-7

Liang, G., Guo, Y., & Shen, S. (2014). Gas properties on crown behavior and drop coalescence. *Numerical Heat Transfer, Part B: Fundamentals*. https://doi.org/10.1080/10407790.2014.884834

Liang, G., Guo, Y., Shen, S., & Yang, Y. (2014). Crown behavior and bubble entrainment during a drop impact on a liquid film. *Theoretical and Computational Fluid Dynamics*. https://doi.org/10.1007/s00162-013-0308-z

Liang, G., Guo, Y., Yang, Y., Guo, S., & Shen, S. (2013). Special phenomena from a single liquid drop impact on wetted cylindrical surfaces. *Experimental Thermal and Fluid Science*. https://doi.org/10.1016/j.expthermflusci.2013.06.012

Liang, G., Guo, Y., Yang, Y., & Shen, S. (2014). Liquid sheet behaviors during a drop impact on wetted cylindrical surfaces. *International Communications in Heat and Mass Transfer*. https://doi.org/10.1016/j.icheatmasstransfer.2014.03.010

Liang, G., Guo, Y., Yang, Y., Zhen, N., & Shen, S. (2013). Spreading and splashing during a single drop impact on an inclined wetted surface. *Acta Mechanica*. https://doi.org/10.1007/s00707-013-0910-6

Liang, G., & Mudawar, I. (2016). Review of mass and momentum interactions during drop impact on a liquid film. *International Journal of Heat and Mass Transfer*, *101*, 577–599. https://doi.org/10.1016/j.ijheatmasstransfer.2016.05.062

Liu, J., Vu, H., Yoon, S. S., Jepsen, R. A., & Aguilar, G. (2010). SPLASHING PHENOMENA DURING LIQUID DROPLET IMPACT. *Atomization and Sprays*. https://doi.org/10.1615/atomizspr.v20.i4.30

Macklin, W. C., & Metaxas, G. J. (1976). Splashing of drops on liquid layers. *Journal of Applied Physics*. https://doi.org/10.1063/1.323218

Martin Rein. (1993). Phenomena of liquid drop impact on solid and liquid surfaces. *Fluid Dynamics Research*, *12*(2), 61. https://doi.org/http://dx.doi.org/10.1016/0169-5983%2893%2990106-K

Motzkus, C., Gensdarmes, F., & Géhin, E. (2009). Parameter study of microdroplet formation by impact of millimetre-size droplets onto a liquid film. *Journal of Aerosol Science*. https://doi.org/10.1016/j.jaerosci.2009.04.001

Motzkus, C., Gensdarmes, F., & Géhin, E. (2011). Study of the coalescence/splash threshold of droplet impact on liquid films and its relevance in assessing airborne particle release. *Journal of Colloid and Interface Science*. https://doi.org/10.1016/j.jcis.2011.06.031

Mukherjee, S., & Abraham, J. (2007). Crown behavior in drop impact on wet walls. *Physics of Fluids*. https://doi.org/10.1063/1.2736085

Okawa, T., Shiraishi, T., & Mori, T. (2008). Effect of impingement angle on the outcome of single water drop impact onto a plane water surface. *Experiments in Fluids*. https://doi.org/10.1007/s00348-007-0406-z

Pan, K. L., & Hung, C. Y. (2010). Droplet impact upon a wet surface with varied fluid and surface properties. *Journal of Colloid and Interface Science*. https://doi.org/10.1016/j.jcis.2010.08.033

Raman, K. A., Jaiman, R. K., Lee, T. S., & Low, H. T. (2015). On the dynamics of crown structure in simultaneous two droplets impact onto stationary and moving liquid film. *Computers and Fluids*. https://doi.org/10.1016/j.compfluid.2014.11.007

Rieber, M., & Frohn, A. (1999). A numerical study on the mechanism of splashing. *International Journal of Heat and Fluid Flow*. https://doi.org/10.1016/S0142-727X(99)00033-8

Rioboo, R., Bauthier, C., Conti, J., Voué, M., & De Coninck, J. (2003). Experimental investigation of splash and crown formation during single drop impact on wetted surfaces. *Experiments in Fluids*, *35*(6), 648–652. https://doi.org/10.1007/s00348-003-0719-5

Roisman, I. V., & Tropea, C. (2002). Impact of a drop onto a wetted wall: Description of crown formation and propagation. *Journal of Fluid Mechanics*. https://doi.org/10.1017/S0022112002002434

Shetabivash, H., Ommi, F., & Heidarinejad, G. (2014). Numerical analysis of droplet impact onto liquid film. *Physics of Fluids*. https://doi.org/10.1063/1.4861761

Shoshan, Y., Wygoda, M., & Umansky, F. (2005). Stereotactic radiosurgery and fractionated stereotactic radiotheraphy: Background, definitions, applications. *Israel Medical Association Journal*, *7*(9), 597–599. https://doi.org/10.1146/annurev.fluid.38.050304.092144

Stow, C. D., & Stainer, R. D. (2017). The Physical Products of a Splashing Water Drop. *Journal of the Meteorological Society of Japan. Ser. II*. https://doi.org/10.2151/jmsj1965.55.5_518

Tropea, C., & Marengo, M. (2014). THE IMPACT OF DROPS ON WALLS AND FILMS. *Multiphase Science and Technology*, *11*(1), 19–36. https://doi.org/10.1615/multscientechn.v11.i1.20

Trujillo, M. F., & Lee, C. F. (2001). Modeling crown formation due to the splashing of a droplet. *Physics of Fluids*. https://doi.org/10.1063/1.1388541

Vander Wal, R. L., Berger, G. M., & Mozes, S. D. (2006). Droplets splashing upon films of the same fluid of various depths. *Experiments in Fluids*. https://doi.org/10.1007/s00348-005-0044-2

Wang, A. B., & Chen, C. C. (2000). Splashing impact of a single drop onto very thin liquid films. *Physics of Fluids*. https://doi.org/10.1063/1.1287511

Worthington, A. M., & Cole, R. S. (2006). Impact with a Liquid Surface Studied by the Aid of Instantaneous Photography. Paper II. *Philosophical Transactions of the Royal Society A: Mathematical, Physical and Engineering Sciences*. https://doi.org/10.1098/rsta.1900.0016

Yarin, A. L. (2006). DROP IMPACT DYNAMICS: Splashing, Spreading, Receding, Bouncing…. *Annual Review of Fluid Mechanics*. https://doi.org/10.1146/annurev.fluid.38.050304.092144

Yarin, A. L., & Weiss, D. A. (1995). Impact of Drops on Solid Surfaces: Self-Similar Capillary Waves, and Splashing as a New Type of Kinematic Discontinuity. *Journal of Fluid Mechanics*. https://doi.org/10.1017/S0022112095002266

Zhang, L. V., Brunet, P., Eggers, J., & Deegan, R. D. (2010). Wavelength selection in the crown splash. *Physics of Fluids*. https://doi.org/10.1063/1.3526743